

**Photocatalytic Activity of Heterostructured Powders:
Nanostructured TiO₂ Shell surrounding Microcrystalline Cores**

Submitted in partial fulfillment of the requirements for

the degree of

Doctor of Philosophy

in

Department of Materials Science and Engineering

Li Li

B.S., Polymer Engineering, Harbin Institute of Technology
M.S., Polymer Chemistry and Physics, Harbin Institute of Technology
M.S., Materials Science and Engineering, Carnegie Mellon University

Carnegie Mellon University

Pittsburgh, PA

September, 2012

Acknowledgements

I would first like to thank my advisors and the committee chairs for my dissertation Prof. Gregory Rohrer and Prof. Paul Salvador for their guidance and help for my research in the past four years. Their strict scientific attitudes and genial personalities have benefited me greatly. I also want to thank my committee members, Prof. Gregory Lowry, Prof. Mohammad Islam, and Prof. Jay Whitacre for their valuable suggestions concerning my research that form the core of this thesis. I want to acknowledge the financial support to my project from National Science Foundation (DMR 0804770 and DMR 1206656) and the PA DCED. The support from MSE staff and faculties is also gratefully appreciated.

I would also want to acknowledge my group members and friends in CMU for their help with my research, as well as with life. I especially want to thank my friends Yiling Zhang and Andy Schultz for research discussions, including those on thin film growth with pulsed laser deposition. Additionally, I want to thank Dr. Wei Wang in MSE department for his great help and guidance when I first arrived in US. Through his help I was able to make me have a great start in the CMU environment.

Finally, I want to thank my parents and my fiancée Xuan Liu. The love and encouragement I receive from them forms the spritual supports that allowed me to successfully pursue my Ph.D. degree. My mother and father are my mentors both in work and life. Their endless love is a constant source of encouragement for me to overcome all difficulties that arises on the road to success. Xuan's help and support

make me confident and resilient in the situation of adversity and disappointment. I could not finish my project successfully without her encouragement. I want to dedicate this thesis to my parents and my fiancée Xuan Liu.

Abstract

The efficiency of photocatalytic water splitting with particulate catalysts is low because of the recombination of photogenerated charge carriers and the back reaction of intermediate chemical species. To efficiently separate the intermediate species and charge carriers, a heterostructured ceramic powder composed of a micron sized light absorbing ferroelectric core surrounded by a nanostructured coating has been synthesized. It is hypothesized that the internal fields from the core can enhance the photocatalytic activity of heterostructured powders both under UV and visible light. The present work compares the photocatalytic activity of heterostructured powders with that of their components and other related formulations. The heterostructured powders investigated include micron-sized (*mc*-) crystallites of ATiO_3 ($\text{A}=\text{Ba}, \text{Sr}, \text{Pb}, \text{Fe}$) and AFeO_3 ($\text{A}=\text{Bi}, \text{La}, \text{Y}$) coated with nanostructured (*ns*-) TiO_2 .

The results show that *mc*-(Ba, Sr) TiO_3 /*ns*- TiO_2 heterostructures annealed at 600 °C are more efficient for photocatalytic hydrogen production than their components alone. That a sonomechanical mixture of BaTiO_3 and commercial TiO_2 (Degussa P25) did not show enhanced photocatalytic hydrogen production, indicates that the interface between the core and the shell is important for enhanced photocatalytic activity. Comparison of the absorbance coefficient of each component implies that the micron sized core is the primary component that absorbs photons. This is also confirmed by the fact that a non-absorbing Al_2O_3 core coated with TiO_2 showed a similar photocatalytic hydrogen production rate to TiO_2 alone. It is argued

that electrons from the core can transfer to the surface of the coating to participate in redox reactions. Micron sized BaTiO₃ coated with nanostructured TiO₂ is more photocatalytically active than a nano sized BaTiO₃/TiO₂ heterostructure, which further indicates the advantage of the micro-nano core/shell heterostructure.

Three parameters that affect the photocatalytic activity of heterostructured powders, namely annealing temperature, cocatalyst loading, and coating thickness, were optimized. The annealing temperature was shown to change the photocatalytic activity of the shell as well as the interface properties. Photocatalysts loaded with 1 wt % Pt showed the greatest photocatalytic hydrogen production rate. An increase of coating thickness, within a certain range, improved the photocatalytic activity of the heterostructured powders.

Ferroelectric PbTiO₃, having a narrower band gap than BaTiO₃, was coated with *ns*-TiO₂ and the heterostructure showed enhanced visible light photocatalytic activity for methylene blue degradation (when compared with the components). This confirms that micro-nano heterostructures are promising for the design of efficient visible-light photocatalysts.

Visible light absorbing *mc*-FeTiO₃ and *mc*-AFeO₃ (A=Bi, La, Y) were also coated with *ns*-TiO₂ for photocatalytic methylene blue degradation under visible light irradiation. Combined with the results from (Ba, Sr, Pb)TiO₃, it is observed that *mc*-ATiO₃/*ns*-TiO₂ (A=Ba, Sr, Pb, Fe) heterostructures show greatly enhanced photocatalytic activities, when compared with their components, while *mc*-AFeO₃/*ns*-TiO₂ (A=Bi, La, Y) do not. It is speculated that the similarities of the electronic

properties (band gap energy and band positions) of the core materials to the TiO₂ coating and the bonding between the core and shell also influence the photocatalytic activity of the micro-nano heterostructures.

TABLE OF CONTENTS

ACKNOWLEDGEMENTS.....	II
ABSTRACT.....	IV
TABLE OF CONTENTS.....	VII
LIST OF TABLES.....	XIII
LIST OF FIGURES	XV
1. INTRODUCTION.....	1
1.1 MOTIVATIONS	1
1.2 OBJECTIVES AND HYPOTHESIS	6
1.3 OUTLINE	10
1.4 REFERENCES.....	11
2. BACKGROUND	13
2.1 INTERNAL FIELD POLARIZATION	13
2.1.1 <i>Ferroelectric</i>	13
2.1.1.1 <i>Definition</i>	13
2.1.1.2 <i>Spontaneous Polarization</i>	14
2.1.1.3 <i>Domains</i>	15
2.1.1.4 <i>Size Effect on Ferroelectrics</i>	16
2.1.2 <i>Surface Termination</i>	18
2.1.3 <i>P-N Junctions</i>	20

2.2	PHOTOCATALYSTS.....	21
2.2.1	<i>Principle of Photocatalytic Water Splitting</i>	21
2.2.2	<i>Visible Light Harvesting</i>	29
2.2.3	<i>Sacrificial Solutions for Water Splitting</i>	32
2.2.4	<i>Photocatalytic Activity Characterization</i>	35
2.2.5	<i>Current TiO₂ Research as Photocatalyst and Approaches for Charge Carrier Separation</i>	38
2.3	HETEROSTRUCTURED PHOTOCATALYST DESIGN.....	41
2.3.1	<i>Dipolar Field Effect</i>	42
2.3.2	<i>Previous Ferroelectric Research Review</i>	43
2.3.3	<i>Heterostructured Photocatalyst</i>	45
2.3.4	<i>Photocatalyst Processing</i>	46
2.3.5	<i>Sol-gel Method</i>	47
2.3.6	<i>Hydrothermal Method</i>	49
2.4	REFERENCES.....	51
3.	MATERIALS AND EXPERIMENTAL METHODS.....	59
3.1	MATERIALS.....	59
3.1.1	<i>BaTiO₃</i>	59
3.1.2	<i>SrTiO₃</i>	60
3.1.3	<i>PbTiO₃</i>	61
3.1.4	<i>FeTiO₃</i>	62
3.1.5	<i>BiFeO₃</i>	62

3.1.6	<i>LaFeO₃</i>	63
3.1.7	<i>YFeO₃</i>	64
3.2	EXPERIMENTAL SETUP.....	64
3.2.1	<i>Core Preparation</i>	64
3.2.1.1	<i>Preparation of Faceted (Ba,Sr)TiO₃</i>	65
3.2.1.2	<i>BiFeO₃ Preparation</i>	66
3.2.1.3	<i>LaFeO₃ Preparation</i>	67
3.2.1.4	<i>YFeO₃ Preparation</i>	68
3.2.2	<i>Coating Process</i>	68
3.2.3	<i>Characterization</i>	70
3.2.3.1	<i>X-ray Powder Diffraction</i>	70
3.2.3.2	<i>Scanning Electron Microscopy</i>	71
3.2.3.3	<i>Transmission Electron Microscopy</i>	71
3.2.3.4	<i>Gas Adsorption Analysis</i>	73
3.2.3.5	<i>Diffuse Reflectance Spectroscopy and Absorbance Spectroscopy</i>	74
3.2.3.6	<i>Gas Chromatography</i>	77
3.2.4	<i>Photocatalytic Activity Characterization</i>	77
3.2.4.1	<i>Photocatalytic Hydrogen Production</i>	77
3.2.4.2	<i>Photocatalytic Dye Degradation</i>	79
3.3	REFERENCES.....	81
4.	PHOTOCATALYTIC ACTIVITY OF (Ba, Sr)TiO₃/TiO₂	85
4.1	HYDROGEN PRODUCTION FROM BaTiO ₃ /TiO ₂	85

4.1.1	<i>BaTiO₃/TiO₂ (Sol-gel)</i>	85
4.1.1.1	<i>Phase Characterization</i>	85
4.1.1.2	<i>Morphology of Core Materials</i>	86
4.1.1.3	<i>Heterostructure Characterization</i>	88
4.1.1.4	<i>Surface Area Characterization</i>	89
4.1.1.5	<i>Photocatalytic Hydrogen Production</i>	91
4.1.2	<i>BaTiO₃/TiO₂ (Sonomechanical Mixture)</i>	93
4.2	HYDROGEN PRODUCTION FROM SrTiO ₃ /TiO ₂	95
4.3	EFFECT OF THE CORE	97
4.4	DISCUSSION	102
4.5	SUMMARY	107
4.6	REFERENCES	108
5.	EFFECT OF GEOMETRIC, COMPOSITIONAL, AND PROCESSING	
	PARAMETERS ON PHOTOCATALYTIC PROPERTIES OF HETEROSTRUCTURED	
	POWDERS	110
5.1	EFFECT OF ANNEALING TEMPERATURE	110
5.2	PHASE AND GRAIN SIZE.....	111
5.2.1	<i>Morphology</i>	116
5.2.2	<i>Surface Area and Pore Structure</i>	118
5.2.3	<i>Photocatalytic Hydrogen Production</i>	119
5.3	EFFECT OF COATING THICKNESS	122
5.4	EFFECT OF Pt LOADING CONTENT	125

5.5	DISCUSSION	126
5.6	SUMMARY.....	132
5.7	REFERENCES.....	133
6.	PHOTOCATALYTIC ACTIVITY OF PbTiO₃/TiO₂ HETEROSTRUCTURED CATALYSTS.....	134
6.1	STRUCTURAL CHARACTERIZATION OF PbTiO ₃ /TiO ₂ HETEROSTRUCTURE.....	135
6.1.1	<i>Phase Composition</i>	135
6.1.2	<i>Morphology</i>	136
6.1.3	<i>Surface Area and Pore Morphology</i>	139
6.1.4	<i>Light Absorption</i>	141
6.2	PHOTOCATALYTIC ACTIVITY	142
6.3	DISCUSSION	146
6.4	SUMMARY.....	152
6.5	REFERENCES.....	152
7.	PHOTOCATALYTIC ACTIVITY OF FeTiO₃/TiO₂ AND AFeO₃/TiO₂ (A= Bi, La, Y) HETEROSTRUCTURES.....	154
7.1	PHOTOCATALYTIC ACTIVITY OF FeTiO ₃ /TiO ₂ HETEROSTRUCTURE	155
7.1.1	<i>Phase Composition</i>	155
7.1.2	<i>Morphology</i>	157
7.1.3	<i>Optical Properties</i>	158
7.1.4	<i>Photocatalytic Activity for Methylene Blue Degradation</i>	160

7.2	PHOTOCATALYTIC ACTIVITY OF (Bi,La,Y)FeO ₃ /TiO ₂ HETEROSTRUCTURE	163
7.2.1	<i>Structure Characterization</i>	163
7.2.2	<i>Photocatalytic Activities of the Heterostructures</i>	165
7.3	DISCUSSION.....	167
7.4	SUMMARY.....	171
7.5	REFERENCES.....	172
8.	CONCLUSIONS AND FUTURE WORK.....	174
8.1	CONCLUSIONS	174
8.2	FUTURE WORK	176
8.3	REFERENCES.....	177

LIST OF TABLES

Table 2-1 Energy distribution in the terrestrial solar spectrum (AM 1.5). (This table is reproduced from reference 26.).....	25
Table 3-1 Spectral energy distribution of 450 W medium-pressure mercury immersion lamp.	79
Table 4-1 Surface area and pore morphologies of F-BaTiO ₃ /TiO ₂ , C-BaTiO ₃ /TiO ₂ and TiO ₂ annealed at 600°C and commercial BaTiO ₃	90
Table 4-2 Summary of physical properties of a BaTiO ₃ /P25 mechanical mixture treated, P25, and P25 treated at 500°C.....	94
Table 4-3 Surface properties of FSTO/TiO ₂ annealed at 500°C, and its components.	96
Table 4-4 Physical properties of <i>mc</i> -BaTiO ₃ / <i>ns</i> -TiO ₂ and <i>ns</i> -BaTiO ₃ / <i>ns</i> -TiO ₂ annealed at 500°C, as well as their components.	101
Table 5-1 The phase composition and TiO ₂ grain sizes of BaTiO ₃ /TiO ₂ , SrTiO ₃ /TiO ₂ , and TiO ₂ annealed at different temperatures.	113
Table 5-2 Summary of physical properties of various photocatalysts annealed at different temperatures.	119
Table 5-3 Summary of physical properties of BaTiO ₃ /TiO ₂ annealed at 500 °C with different coating cycles. (BTO/ <i>n</i> TiO ₂ : <i>n</i> means coating cycles.).....	125
Table 6-1 Comparison of anatase d-spacings and lattice parameters for titania, Pb-doped TiO ₂ , and TiO ₂ in the heterostructures (labeled H-TiO ₂).	136
Table 6-2 Surface areas and pore characteristics of <i>mc</i> -PbTiO ₃ / <i>ns</i> -TiO ₂ and its components.	

.....	140
Table 7-1 Lattice parameters and unit cell volumes of undoped TiO ₂ , Fe-doped TiO ₂ (D-TiO ₂), and TiO ₂ phases in FeTiO ₃ /TiO ₂ heterostructure (H-TiO ₂).	156
Table 7-2 Physical properties of heterostructured powders and their reaction rates for photocatalytic degradation of methylene blue (K _{MB}).	161
Table 7-3 Physical properties of heterostructured powders and its reaction rate for photocatalytic degradation of methylene blue (K _{MB}).	166
Table 7-4 Electronic properties of various core materials and TiO ₂	168

LIST OF FIGURES

Figure 1-1 Schematic illustrations of water photolysis in a PECs with TiO ₂ and Pt as electrode. (This figure is reproduced from reference 11.).....	3
Figure 1-2 Photosynthesis by green plants and photocatalytic water splitting as an artificial photosynthesis. (This figure is reproduced from reference 9.).....	3
Figure 1-3 Simple schematic of powder photocatalyst for water splitting. (This figure is reproduced from reference 11.).....	4
Figure 1-4 A highly simplified schematic of a heterostructured ceramic powder.	8
Figure 2-1 Crystal structure of the perovskite ferroelectric BaTiO ₃ . (A) High temperature, paraelectric, cubic phase. (B and C) Room temperature, ferroelectric, tetragonal phases, showing up and down polarization variants. (This figure is reproduced from reference 5.).....	14
Figure 2-2 Schematic of domains in a ferroelectric crystal. (This figure is reproduced from reference 9.)	16
Figure 2-3 Variation of spontaneous polarization at transition (P_s) and at 25 °C (P_3) with particle size for PbTiO ₃ . (This figure is reproduced from reference 10.).....	17
Figure 2-4 Size effect on the spontaneous polarization of single domain tetragonal BaTiO ₃ . (This figure is reproduced from reference 11.)	18
Figure 2-5 The influence of dipolar field created by polar surface termination on the photochemical reactivity of SrTiO ₃ . (This reference is reproduced from the reference 18.).....	20

Figure 2-6 The schematic of p-n junction formation between two semiconductors without the applied external voltage.	21
Figure 2-7 Schematic representation of water photoelectrolysis using illuminated oxide semiconductor electrode. (This figure is reproduced from reference 22.)	22
Figure 2-8 Main processes in photocatalytic water splitting. (This figure is reproduced from reference 23.).....	24
Figure 2-9 Schematic representation of relationship between band structure of semiconductor and redox potential. (This figure is reproduced from reference 24.).....	24
Figure 2-10 Effect of particle size and boundary on photocatalytic activity. (This figure is reproduced from reference 27.).....	26
Figure 2-11 Band Structure of n-type semiconductor with different particle size. (This figure is reproduced from reference 31.).....	27
Figure 2-12 Schematic illustration of H ₂ evolution on core/shell-structured nanoparticles (with a noble metal or metal oxide core and a Cr ₂ O ₃ shell) as cocatalyst for photocatalytic overall water splitting. (This figure is reproduced from reference 45.)	29
Figure 2-13 Schematic illustration of dye-sensitized hydrogen production from water. (This figure is reproduced from reference 66.).....	31
Figure 2-14 Schematic for the mechanism of charge separation for coupled semiconductors. (This reference is reproduced from reference 75.).....	32
Figure 2-15 Scheme of photoinduced charge transfer on the surface of spatially separated illuminated semiconductors S1 and S2. (This figure is reproduced from reference	

86.)	34
Figure 2-16 The semiconductor-mediated photodegradation initiated by the surface electron injection from the adsorbed dye molecules that harvest visible light. (This figure is reproduced from reference 103.)	36
Figure 2-17 Distribution of scientific publications focusing on nanomaterials for photocatalytic hydrogen production. (This figure is reproduced from reference 114.)	38
Figure 2-18 Band bending in a polarized crystal. (a) Band bending due to insufficient positive surface charge. (b) Band bending for the crystal in the case of net positively and negatively charged surfaces. (This figure is reproduced from reference 2.)	42
Figure 2-19 Schematic of the effect from internal electric field on the photocatalytic chemical reaction. (This figure is reproduced from reference 2.).....	43
Figure 3-1 Schematic illustration of BiFeO ₃ structure. (This figure is reproduced from reference 40.).....	63
Figure 3-2 Structure of 125 mL acid digestion vessel. (This figure is reproduced from reference 58.).....	67
Figure 3-3 Emission produced by the interaction of an electron beam with a solid sample. (This figure is reproduced from reference 63.)	72
Figure 3-4 Schematic representation of various characterization methods for particle size. (This figure is reproduced from reference 65.)	74
Figure 3-5 Schematic of photocatalytic hydrogen production reactor setup.	78
Figure 3-6 Transmittance graph of the borosilicate immersion well. (This figure is reproduced	

from reference 71.).....	79
Figure 3-7 Schematic of photocatalytic dye degradation setup.....	80
Figure 3-8 Emission spectrum of 300 W mercury lamp used in the experiment. (This figure is reproduced from reference 3.).....	81
Figure 4-1 Powder x-ray diffraction patterns of platinumized (a) BaTiO ₃ , (b) TiO ₂ , and (c) BaTiO ₃ /TiO ₂ annealed at 600 °C.	87
Figure 4-2 The morphology of BaTiO ₃ powders (a) before treatment and (b) after molten salt treatment (The inset is high magnification of powders prepared from molten salt method. The inside scale bar is referred to 300 nm.)	87
Figure 4-3 Bright field TEM images of a platinumized heterostructured particle composed of a <i>mc</i> -BaTiO ₃ core and a <i>ns</i> -TiO ₂ shell annealed at 600 °C. (a) shows the entire particle and (b) shows a higher magnification of the coating.	89
Figure 4-4 Surface area characterization of <i>mc</i> -F-BaTiO ₃ / <i>ns</i> -TiO ₂ annealed at 600 °C: (a) pore size distribution and (b) nitrogen adsorption-desorption isothermal.....	91
Figure 4-5 Time dependent hydrogen production per surface area from platinumized BaTiO ₃ , TiO ₂ , F-BaTiO ₃ /TiO ₂ and C-BaTiO ₃ /TiO ₂ annealed at 600 °C.	92
Figure 4-6 Powder x-ray diffraction patterns of platinumized (a) BaTiO ₃ , (b) P25 and (c) BaTiO ₃ /P25.	93
Figure 4-7 SEM images of a BaTiO ₃ and P25 mechanical mixture.....	94
Figure 4-8 Powder x-ray diffraction patterns of platinumized (a) SrTiO ₃ , (b) TiO ₂ , and (c) SrTiO ₃ /TiO ₂ annealed at 500°C.	95
Figure 4-9 Bright field TEM images of a platinumized heterostructured particle composed of a	

<p><i>mc</i>-SrTiO₃ core and <i>ns</i>-TiO₂ shell annealed at 500 °C: (a) shows the entire particle and (b) shows a higher magnification of the coating.</p>	96
<p>Figure 4-10 Hydrogen production from platinized SrTiO₃/TiO₂, TiO₂, and SrTiO₃ annealed at 500 °C (1 wt% Pt) in 100 mL 8 % methanol water solution.</p>	97
<p>Figure 4-11 UV-vis diffuse reflectance spectra of (a) platinized BaTiO₃/TiO₂ and its components annealed at 500 °C (b) platinized SrTiO₃/TiO₂ and annealed at 600 °C.</p>	98
<p>Figure 4-12 Powder x-ray diffraction patterns of Pt-Al₂O₃/TiO₂ annealed at (a) 500 °C and (b) 600 °C (A: Al₂O₃, T: TiO₂).</p>	98
<p>Figure 4-13 Hydrogen production from platinized Al₂O₃/TiO₂ and its components annealed at 500 °C and 600 °C as well as BET surface area (-500, -600 represents the powders annealed at 500 °C and 600 °C).</p>	100
<p>Figure 4-14 Pore size distribution of <i>mc</i>-BaTiO₃/<i>ns</i>-TiO₂ and <i>ns</i>-BaTiO₃/<i>ns</i>-TiO₂ annealed at 500 °C.</p>	101
<p>Figure 4-15 Hydrogen production from platinized <i>mc</i>-BaTiO₃/<i>ns</i>-TiO₂ and <i>ns</i>-BaTiO₃/<i>ns</i>-TiO₂ annealed at 500 °C.</p>	102
<p>Figure 4-16 A highly simplified schematic representation of band structure diagram of heterostured BaTiO₃/TiO₂ for (a) and (b) thin coating with different polarization directions. (E_{vac}, E_c, E_f and E_v represent the edge for vacuum level, conduction band, Fermi level and valance band, respectively. P_s refers to spontaneous polarization from ferroelectrics. The hydrogen and oxygen redox level are shown in the right.).....</p>	104

Figure 5-1 Comparison of powder x-ray diffraction patterns of platinized TiO ₂ annealed at 400-600 °C. (T-400 represents TiO ₂ annealed at 400 °C, etc; A and R refer to anatase and rutile.)	112
Figure 5-2 Comparison of powder x-ray diffraction patterns of platinized BaTiO ₃ /TiO ₂ , SrTiO ₃ /TiO ₂ , and TiO ₂ annealed at 700 °C. (A and R refer to anatase and rutile.)	113
Figure 5-3 Bright field TEM images of a platinized heterostructured particle composed of a <i>mc</i> -BaTiO ₃ core and <i>ns</i> -TiO ₂ shell annealed at 400 °C: (a) shows the entire particle, (b) shows a higher magnification of the coating, 500 °C: (c) shows the entire particles, and (d) shows a higher magnification of the coating.	116
Figure 5-4 Bright field TEM images of a platinized heterostructured particle composed of a <i>mc</i> -SrTiO ₃ core and a <i>ns</i> -TiO ₂ shell annealed at 800 °C: (a) shows the entire particle and (b) shows a higher magnification image of the coating.....	117
Figure 5-5 TEM bight field images of BaTiO ₃ /TiO ₂ annealed at 500 °C with (a) one coating cycle, (b) two coating cycles, and (c) three coating cycles.	124
Figure 5-6 Pore size distribution of BaTiO ₃ /TiO ₂ annealed at 500 °C with different coating cycles.....	125
Figure 5-7 Hydrogen production from SrTiO ₃ /TiO ₂ annealed at 600 °C with different amounts of Pt. (The number marked in the figure is referred to weight percentage relative to the entire photocatalyst mass.)	126
Figure 5-8 A highly simplified schematic representation of band structure diagram of heterostructured BaTiO ₃ /TiO ₂ for: (a)(b) thick and (c)(d) thin coatings with	

different polarization directions. (E_{vac} , E_c , E_f and E_v represent the edge for vacuum level, conduction band, Fermi level and valance band, respectively. P_s refers to spontaneous polarization from ferroelectrics. The hydrogen and oxygen redox level are shown in the right.)..... 131

Figure 6-1 X-ray diffraction patterns of (a) $PbTiO_3$, (b) $PbTiO_3/TiO_2$, (c) TiO_2 , and (d) Pb -doped TiO_2 annealed at 500 °C..... 135

Figure 6-2 TEM images of heterostructured particles composed of *mc*- $PbTiO_3$ and *ns*- TiO_2 annealed at 500 °C: (a) low magnification bright field image of entire particle, (b) high magnification bright field image of detail of the $PbTiO_3/TiO_2$ interface, (c) HRTEM image of the interface, (d) SAED of TiO_2 coating, and (e) HRTEM image of the interface after in-situ annealing with high energy electron beam. 138

Figure 6-3 (a) Isothermal curves and (b) pore size distribution of $PbTiO_3/TiO_2$ annealed at different temperatures (the number in the caption refers to the annealing temperature). 141

Figure 6-4 Absorbance data, converted from diffuse reflectance spectra using the K-M function for (a) $PbTiO_3/TiO_2$, (b) $PbTiO_3$, and (c) TiO_2 annealed at 500 °C. The inset enlarges the absorbance spectra between 400 nm and 450 nm. 142

Figure 6-5 Photochemical dye degradation with $PbTiO_3/TiO_2$ annealed at 500 °C and its component phases during irradiation by visible light ($\lambda > 420$ nm). Absorbance data labeled blank, which is overlaid by the $PbTiO_3$ data, is from a control experiment conducted without the addition of a catalyst. 145

Figure 6-6 Methylene blue degradation with $PbTiO_3/TiO_2$ annealed at different temperatures

from 400 °C to 600 °C and TiO ₂ doped with 1 mol% Pb.....	146
Figure 6-7 A schematic energy level diagram of PbTiO ₃ /TiO ₂ with (a) negative polarization and (b) positive polarization normal to the heterostructure interface. E _{vac} , E _C , E _F , E _v , and E _s are the energies of the vacuum level, conduction band, Fermi level, valance band, and surface potential, respectively.	147
Figure 7-1 X-ray diffraction pattern of <i>mc</i> -FeTiO ₃ / <i>ns</i> -TiO ₂ core/shell heterostructure annealed at different temperatures from 400 to 600 °C and their components. The diffraction pattern of 1mol% Fe doped TiO ₂ is also shown. The number after the heterostructure represents the annealing temperature in the preparation of heterostructure by sol-gel method. (e.g. -400: 400 °C). The TiO ₂ and FeTiO ₃ powders were annealed at 500°C.	156
Figure 7-2 TEM images of <i>mc</i> -FeTiO ₃ / <i>ns</i> -TiO ₂ heterostructure powders annealed at 500 °C: (a) low magnification bright field images of the entire particles; (b) high magnification bright field image of detail about FeTiO ₃ and TiO ₂ interface; (c) SAED of TiO ₂ coating; and (d) HRTEM image of TiO ₂ coating.....	158
Figure 7-3 UV-visible spectra of <i>mc</i> -FeTiO ₃ / <i>ns</i> -TiO ₂ heterostructure annealed at different temperatures, its components, and Fe-doped TiO ₂	160
Figure 7-4 Photodegradation of methylene blue with FeTiO ₃ /TiO ₂ annealed at 500 °C and its components. The reactivity of FeTiO ₃ and TiO ₂ mechanical mixture as well as Fe doped TiO ₂ are also shown here. Blank refers to the dye degradation without any powder addition.....	163
Figure 7-5 Powder x-ray diffractograms of (a) BiFeO ₃ prepared by hydrothermal method, (b)	

YFeO₃ prepared by sol-gel method, and (c) LaFeO₃ prepared by citrate gel method.

..... 164

Figure 7-6 Powder x-ray diffractograms of various heterostructured powders. The titanium dioxide phase was designated as “T” and marked in the figure. 164

Figure 7-7 Photodegradation of methylene blue with (Pb,Fe)TiO₃/TiO₂ and (Bi,La,Y)FeO₃ annealed at 500 °C and TiO₂ under visible light illumination. 166

Figure 7-8 The schematic of band gap energy and band positions for various core materials. 170

1. Introduction

1.1 Motivations

Currently, society derives its energy primarily from fossil fuels, which produce greenhouse gas emissions to the atmosphere, amongst other pollutants. Other disadvantages of fossil fuels are that they must be retrieved from the earth through environmentally questionable mining/drilling practices, and are distributed unevenly across the globe. While renewable energy sources, including hydroelectric, geothermal, tides, etc., are considered as potential energy resources, they only account for a minor percentage of the total present energy production.¹ Hydrogen, the simplest closed-shell molecule possible, is attracting scientific and technological interest as a primary energy carrier and as a potential transportation fuel.² Hydrogen can be considered as an alternative fuel to fossil sources because it has three times the energy density of oil and its combustion is considered to be environmentally friendly.

Hydrogen can be presented as an alternative energy to the traditional fossil fuels, but only with the realization of an appropriate source.³ Currently, the primary hydrogen production method used in industry is steam reforming of hydrocarbon feedstocks,⁴⁻⁷ which are considered as non-renewable sources that hydrogen is meant to replace. Renewable energy only contributes 5 % of commercial hydrogen production, primarily via water electrolysis with renewable electrical power source.⁶ The high expense of electrolysis restricts its use to the production of highly pure

hydrogen. Therefore, other methods to produce hydrogen from renewable energy sources need to be considered. The amount of solar energy that falls on the earth's surface every year exceeds our energy consumption; solar energy is the only renewable energy that has the capacity to satisfy current energy demands or those predicted for the future.⁸ Solar energy is considered a relatively clean and secure energy source, which is advantageous to decrease the pressure on the environment. Owing to its potential environmental and economic benefits, solar hydrogen production has been receiving increased attention.⁹

A major breakthrough for solar hydrogen production was discovered in 1972 by Japanese scientists Fujishima and Honda.¹⁰ It was observed that hydrogen and oxygen were produced respectively on the surface of Pt and TiO₂ electrodes when ultraviolet light illuminated the TiO₂ electrode immersed in an electrolyte aqueous solution. When TiO₂ was irradiated by photons of energy equivalent to or greater than its band gap, electrons in the valence band were excited to the conduction band, leaving holes in the valence band. These photogenerated electrons and holes can move to the surface of the electrode to participate in redox reactions. Under this circumstance, the whole water splitting process can be divided into two sub-reactions: (a schematic of this process is shown in figure 1-1).¹¹

At the TiO₂ electrode: $\text{H}_2\text{O} + 2\text{h}^+ = 1/2\text{O}_2 + 2\text{H}^+$ (oxidation)

At the Pt electrode: $2\text{e}^- + 2\text{H}^+ = \text{H}_2$ (reduction)

The above process provides one method for conversion of solar energy to chemical energy, a potential way to produce hydrogen from a clean and abundant

source. This conversion from solar energy to chemical energy is analogous to photosynthesis in green plants, both resulting in an uphill Gibbs free energy change. Therefore, photocatalytic water splitting is also considered as artificial photosynthesis (shown in figure 1-2).⁹

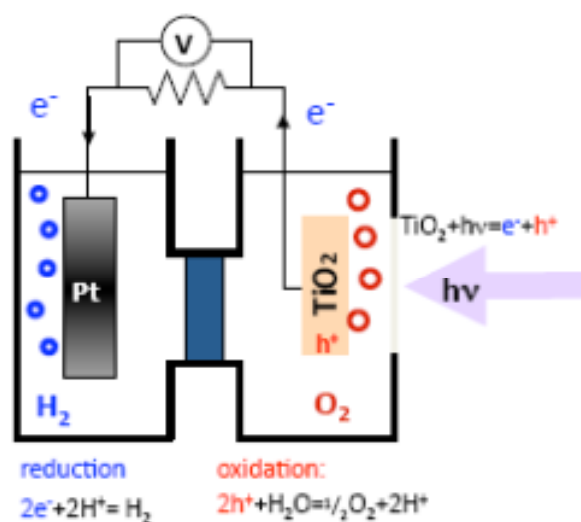


Figure 1-1 Schematic illustrations of water photolysis in a PECs with TiO₂ and Pt as electrode. (This figure is reproduced from reference 11.)

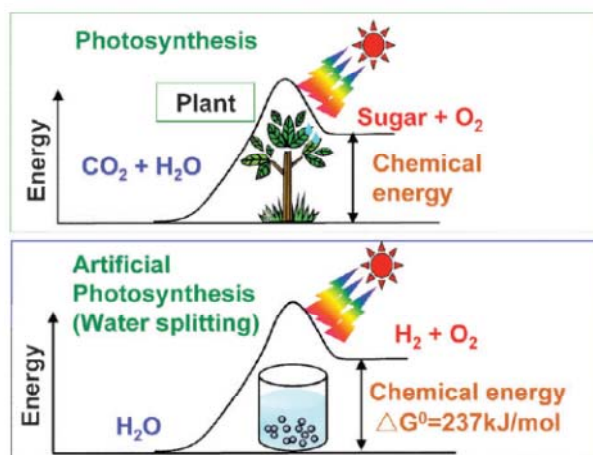


Figure 1-2 Photosynthesis by green plants and photocatalytic water splitting as an artificial photosynthesis. (This figure is reproduced from reference 9.)

Generally speaking, photolysis is achieved primarily by two methods: photoelectrolysis using photoelectrochemical cells (PECs)¹² and photolysis using

colloidal suspensions of powdered catalysts, such as TiO_2 ^{13,14} and other ceramics powders.¹⁵ The most outstanding advantage for photoelectrochemical cells is the relatively high efficiency because the photogenerated electrons and holes are separated spatially to different electrodes, which decreases the possibility of carrier recombination. Meanwhile, hydrogen and oxygen are also evolved in the different locations, diminishing the back reaction of intermediate chemical species.^{16,17} However, the high cost for processing is restricting the use of PECs in industry and more work must be done to make them economically feasible.

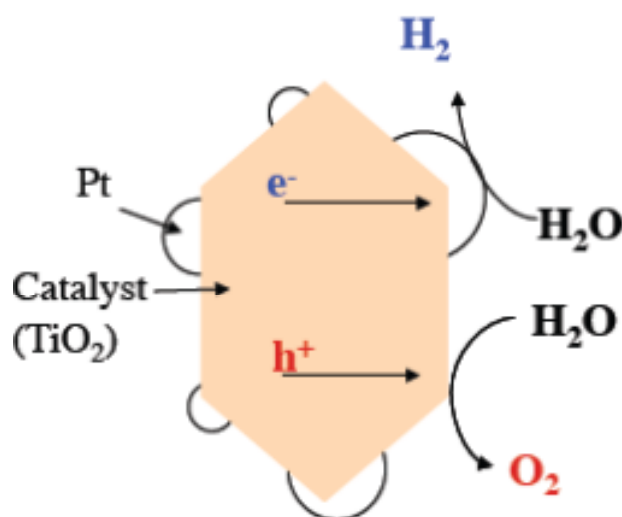


Figure 1-3 Simple schematic of powder photocatalyst for water splitting. (This figure is reproduced from reference 11.)

Photolysis using powdered catalysts is considered a potential method to achieve water splitting in a scalable fashion. Compared with PECs, the cost of processing powders is relatively low. The most significant factor constraining their use is their low efficiency. The schematic structure of a powdered photocatalyst is shown in figure 1-3 using TiO_2/Pt as the example.¹¹ In general, the powder photocatalyst absorbs a small fraction of light and then only a small percentage of those photons are

used for photolysis.^{17,18} Furthermore, high surface area powder photocatalysts have small sizes that do not fully support internal space charges.¹⁹ Therefore, the photogenerated charge carriers and the reaction products are produced in close proximity in such powdered photocatalysts, and this is considered one of the main bottlenecks of particulate systems.²⁰

At present, the efficiency of photocatalysts for water splitting is quite limited. The highest quantum efficiency (QE, defined as the ratio between number of reacted electrons and number of incident photons),⁹ which is one important figure of merit for realistic technologies of a photocatalyst for pure water splitting under visible light, is 2.5 % using a Cr/Rh-modified GaN/ZnO.²¹⁻²³ The maximum solar energy conversion of water splitting for a semiconductor with a 2.5 eV band gap is 14 %.²⁴ Nowadays, 10 % is the target for commercial application of powdered photocatalysts under visible light.²⁵ The technology for photocatalytic water splitting with powdered photocatalysts has significant space for improvement and many studies are focusing on these materials and technologies.

Much work has focused on the two important limitations of powdered photocatalysts, namely the recombination of photogenerated charge carriers and the back reaction of intermediate chemical species.^{9,25-31} The previous research in our group showed that the surface reactivity of thin (<100 nm) dense TiO₂ coatings supported on ferroelectrics was directly influenced by the underlying domain structure of the ferroelectric (BaTiO₃).^{32,33} Inoue et al. showed earlier that the photocatalytic activity of TiO₂ or NiO film supported by poled ferroelectric LiNbO₃ was enhanced

for one type of domain polarization (positive or negative).³⁴ These research efforts provide evidence that the internal electric fields from ferroelectrics (or other sources) can be used both to separate photogenerated electrons and holes and to control the spatial location of oxidation and reduction processes, thereby mitigating the two losses described above (analogous to the external field in the photoelectrochemical cell). This motivates our group to design efficient heterostructured photocatalysts in which the movement of electrons and holes are controlled by internal electric fields.

1.2 Objectives and Hypothesis

The long-term objective of this project is to establish a scientific model combining both the advantages of PECs and powder photocatalysts, to allow the efficient separation of photogenerated carriers and reaction products intermediates in the particulate catalyst. This model can provide a new strategy for the design of efficient photocatalysts for future hydrogen production from water using UV and visible light.

The model photocatalyst proposed here is shown in figure 1-4. On the left, the white particle represents the microcrystalline (*mc*) core. Charged surfaces arise from the internal field from the ferroelectric micron-sized core, from the net interfacial charge based on planar chemical termination, or from electronic interactions between the core and shell. The blue layer represents the nanostructured catalytic coating for water splitting (here take TiO₂ as an example). Dark spheres represent impregnated Pt

particles, which are used as a cocatalyst for providing active sites, (decreasing the free Gibbs energy of the barrier) for hydrogen evolution.

There are a number of questions concerning heterostructured photocatalysts that motivate this research, eight of which are listed here. Most of these will be addressed at some level in the research presented herein.

- 1) Can the ferroelectric core drive the separation of electrons and holes in the catalytic coating such that the photocatalytic activity of the composite catalyst can be enhanced?
- 2) Can other internal electric fields (besides those arising from ferroelectric polarization) have an effect on the separation of photogenerated carriers in the catalytic coating?
- 3) Do the micron-sized cores act as the primary light absorbing component in the heterostructured photocatalyst?
- 4) Is there an appreciable difference in the photocatalytic activity for differently sized (nano and micro) cores?
- 5) Do the geometric parameters, such as the thickness and grain size, of the nanostructured coating affect the photocatalytic activity?
- 6) What is the influence of the cocatalyst loading (amount) on the hydrogen production rate?
- 7) Is the interface between the core and coating important for improvement of photocatalytic activity?
- 8) What are the selection criteria for the core and coating material to optimize

performance?

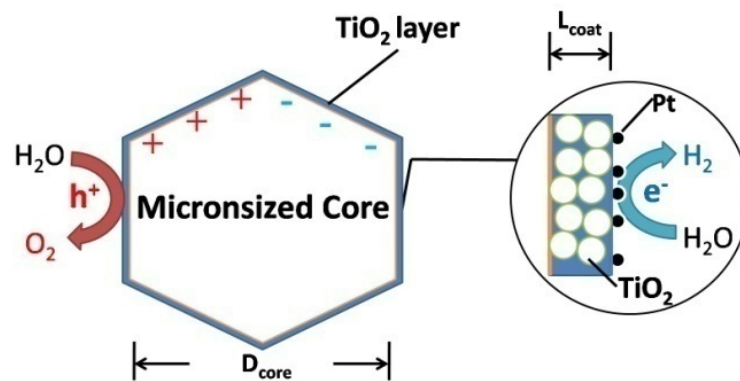


Figure 1-4 A highly simplified schematic of a heterostructured ceramic powder.

Building on these questions, two detailed hypotheses are proposed here.

- i) A heterostructured ceramic powder composed of a micron-sized (UV and visible) light absorbing ferroelectric core surrounded by a nanostructured catalytic coating will exhibit enhanced photocatalytic activity when compared to its components alone.

- ii) The photocatalytic activity of the heterostructured photocatalyst can be optimized by controlling the thickness of nanostructured coating, as well as the processing temperature and the amount of the co-catalyst.

Hypothesis (i) can be further divided into several parts:

- i.a) The ferroelectric core will improve the photocatalytic activity of the heterostructured ceramic powder.

- i.b) The core is the primary component in the heterostructure to absorb light.

- i.c) The core dimension should be large enough to support band bending in a volume comparable to the absorption depth of the light and the coating that

surrounds the core should be nanostructured.

i.d) By choosing appropriate components of the core, the heterostructured photocatalyst can have improved photocatalytic activity both under UV and visible light irradiation.

To test these hypotheses and sub-hypotheses, micron-sized ferroelectric barium titanate (BaTiO_3) was selected as a UV-absorbing core surrounded by a nanostructured TiO_2 layer for water splitting, under UV light irradiation. Simultaneously, non-ferroelectric strontium titanate (SrTiO_3) was used as a comparison to investigate the difference between ferroelectric and non-ferroelectric cores in hydrogen production (i.a). Nano-sized BaTiO_3 was coated with nanostructured TiO_2 with the same processing procedure to micron-sized $\text{BaTiO}_3/\text{TiO}_2$. This control experiment is used to check the influence of core size on the photocatalytic activity of heterostructured powders (i.c). Ferroelectric PbTiO_3 , reported to have a narrower band gap energy than BaTiO_3 , was used to investigate the photocatalytic activity of the heterostructured powder under visible light. In addition, a small number of other ABO_3 perovskites, namely BiFeO_3 (ferroelectric), $(\text{La}, \text{Y})\text{FeO}_3$ (non-ferroelectrics), and ilmenite, FeTiO_3 (non-ferroelectric), are tested for water splitting and other photochemical reactions to investigate their photocatalytic activity under UV and visible light (i.d). The absorption properties of all materials are tested and different light sources are also used to demonstrate that the core primarily absorbs light (i.b).

Hypothesis (ii) focuses on the optimization of the photocatalytic hydrogen

production rate by controlling the materials properties and geometric dimensions. To test this hypothesis, the hydrogen production rate from heterostructured photocatalysts with coatings of different thicknesses is compared. The annealing temperature for processing the heterostructured photocatalysts are investigated to obtain nanostructured catalytic coatings with different grain sizes. Furthermore, the hydrogen production rate from photocatalysts with different percentages of Pt loading is investigated. Ultimately, this work aims to shed light on the design criteria for heterostructured photocatalysts for water photolysis.

1.3 Outline

The document is organized as follows. Chapter 2 will introduce background information about ferroelectrics, the conceptual and fundamental mechanisms of photocatalysts, the common characterization methods for measuring photocatalytic activity, and the traditional single and composite materials processing methods. Chapter 3 will introduce the materials used in the experiments, the experimental setups, as well as the structure and property characterization techniques. Chapter 4 will summarize the hydrogen production results from BaTiO₃ and SrTiO₃ based heterostructures, to investigate the effect of the ferroelectric core on photocatalytic activity. Chapter 5 will explore the influence of processing temperature, nanostructured coating thickness, and cocatalyst loading to optimize the hydrogen production rate. In Chapter 6, *mc*-PbTiO₃ coated with *ns*-TiO₂ is investigated to determine the photocatalytic activity of a visible light absorbing heterostructure

powder. Chapter 7 describes experiments on FeTiO₃ and other AFeO₃ core materials to examine the affect of changing core composition and explore the selection criteria for the core materials. Chapter 8 will describe the conclusions that are drawn from all findings and discuss their implications for the design of efficient photocatalysts.

1.4 References

- (1) In *Energy Information Administration /Annual Energy Review In 2005*, 2005.
- (2) Lubitz, W.; Tumas, W. *Chemical Reviews* **2007**, *107*, 3900.
- (3) Esswein, A. J.; Nocera, D. G. *Chemical Reviews* **2007**, *107*, 4022.
- (4) Navarro, R. M.; Pena, M. A.; Fierro, J. L. G. *Chemical Reviews* **2007**, *107*, 3952.
- (5) Al-Mazroai, L. S.; Bowker, M.; Davies, P.; Dickinson, A.; Greaves, J.; James, D.; Millard, L. *Catalysis Today* **2007**, *122*, 46.
- (6) Ni, M.; Leung, M. K. H.; Leung, D. Y. C.; Sumathy, K. *Renewable and Sustainable Energy Reviews* **2007**, *11*, 401.
- (7) Palo, D. R.; Dagle, R. A.; Holladay, J. D. *Chemical Reviews* **2007**, *107*, 3992.
- (8) Cunningham, W. P. S., B. W. *McGraw-Hill Science/Engineering/Math* **2005**.
- (9) Kudo, A.; Miseki, Y. *Chemical Society Reviews* **2009**, *38*, 253.
- (10) Fujishima, A.; Honda, K. *Nature* **1972**, *238*, 37.
- (11) Masao, K.; Ichiro, O. *Photocatalysis Science and Technology*; Springer, 2002.
- (12) Bard, A. J. *The Journal of Physical Chemistry* **1982**, *86*, 172.
- (13) Schrauzer, G. N.; Guth, T. D. *Journal of the American Chemical Society* **1977**, *99*, 7189.
- (14) Kraeutler, B.; Bard, A. J. *Journal of the American Chemical Society* **1978**, *100*, 4317.
- (15) Reber, J. F.; Meier, K. *The Journal of Physical Chemistry* **1984**, *88*, 5903.
- (16) Tryk, D. A.; Fujishima, A.; Honda, K. *Electrochimica Acta* **2000**, *45*, 2363.
- (17) K.Domen. Characterization of Photoexcitation Processes on Solid Surfaces. In *Surface Photochemistry*; M. Anpo. J. Wiley & Sons, Chichester, 1996; pp 1.
- (18) Rohrer, G. S.; Salvador, P. A. *Proposal for NSF project* **2008**.
- (19) Alberly, W. J.; Bartlett, P. N. *Journal of the Electrochemical Society* **1984**, *131*, 315.
- (20) Nokik, A. J. *Photoeffects of semi-conductor-electrolyte interfaces*; American Chemical Society: Washington, D.C., 1981.
- (21) Maeda, K.; Teramura, K.; Lu, D. L.; Takata, T.; Saito, N.; Inoue, Y.; Domen, K. *Journal of Physical Chemistry B* **2006**, *110*, 13753.
- (22) Maeda, K.; Teramura, K.; Lu, D. L.; Takata, T.; Saito, N.; Inoue, Y.; Domen, K. *Nature* **2006**, *440*, 295.
- (23) Maeda, K.; Takata, T.; Hara, M.; Saito, N.; Inoue, Y.; Kobayashi, H.; Domen, K. *Journal of the American Chemical Society* **2005**, *127*, 8286.
- (24) Morrison, S. R. *Electrochemistry at semiconductor and oxidized metal electrodes*; Plenum Press: New York, 1980.
- (25) Osterloh, F. E. *Chemistry of Materials* **2008**, *20*, 35.

- (26) Hernandez-Alonso, M. D.; Fresno, F.; Suarez, S.; Coronado, J. M. *Energy & Environmental Science* **2009**, *2*, 1231.
- (27) Maeda, K.; Domen, K. *Journal of Physical Chemistry Letters* **2010**, *1*, 2655.
- (28) Rufino M. Navarro Yerga, M. C. A. G., F. del Valle, Jose A. Villoria de la Mano, and Jose L. G. Fierro. *ChemSusChem* **2009**, *2*, 471.
- (29) Joshi, U. A.; Palasyuk, A.; Arney, D.; Maggard, P. A. *Journal of Physical Chemistry Letters*, *1*, 2719.
- (30) Tachikawa, T.; Fujitsuka, M.; Majima, T. *Journal of Physical Chemistry C* **2007**, *111*, 5259.
- (31) Rajeshwar, K. *Journal of Applied Electrochemistry* **2007**, *37*, 765.
- (32) Burbure, N. V.; Salvador, P. A.; Rohrer, G. S. *Chemistry of Materials* **2010**, *22*, 5823.
- (33) Burbure, N. V.; Salvador, P. A.; Rohrer, G. S. *Chemistry of Materials* **2010**, *22*, 5831.
- (34) Inoue, Y.; Okamura, M.; Sato, K. *Journal of Physical Chemistry* **1985**, *89*, 5184.

2. Background

This chapter describes fundamental background information concerning ferroelectrics, heterostructured photocatalysts, and photocatalyst processing that are relevant to the research discussed in this dissertation. It attempts to systematically introduce such background knowledge to aid the reader in further understanding how the objectives and hypothesis proposed in the previous chapter were chosen and how they will be addressed. When appropriate, current research trends are also described.

2.1 Internal Field Polarization

2.1.1 Ferroelectric

2.1.1.1 Definition

A ferroelectric is defined as an insulating material with two or more discrete stable (or metastable) states of different nonzero electric polarization in zero applied electric field, which is referred to as spontaneous polarization.¹ Ferroelectrics are non-centrosymmetric with positive and negative charges having different centers of symmetry resulting in a polarized crystal.² Any two of the orientation states are normally identical in the crystal structure, differing only in the direction of the electric polarization vector.³ The polarization vector can be switched between these different orientation states with an applied electric field, which changes the relative energy of

the states through the coupling of the field to the polarization.¹

2.1.1.2 Spontaneous Polarization

The spontaneous polarization is one of the important characteristic features of a ferroelectric.⁴ The detailed mechanism of generating spontaneous polarization varies in different ferroelectrics. In general, this polarization arises from displacements of individual atoms or ions in the crystal structure. The most common and extensively studied ferroelectrics are perovskite oxides, represented as ABO_3 (where A and B represents cationic elements). $BaTiO_3$, the first perovskite oxide compound identified as ferroelectric,¹ is used here as an example to introduce polarization generation.

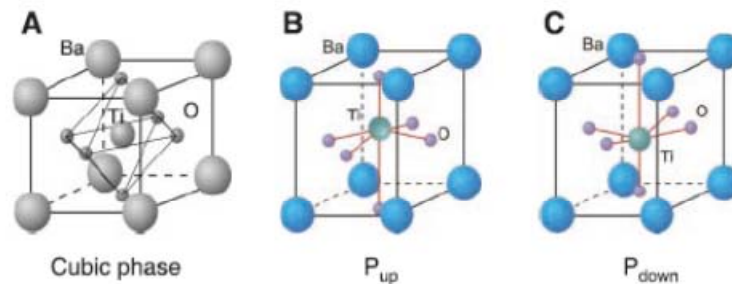


Figure 2-1 Crystal structure of the perovskite ferroelectric $BaTiO_3$. (A) High temperature, paraelectric, cubic phase. (B and C) Room temperature, ferroelectric, tetragonal phases, showing up and down polarization variants. (This figure is reproduced from reference 5.)

Figure 2-1 shows the crystal structure of $BaTiO_3$ at different temperatures.⁵ At high temperatures (above 393K), the crystal displays a cubic perovskite structure and no spontaneous polarization is observed (figure 2-1 A). When the temperature is below 393 K, but above 278 K, the octahedral cages of oxygen distort and the Ti and Ba sublattices are shifted relative to the negatively charged oxygens, which produces the polarization. The specific shift of atoms (along $\langle 100 \rangle$) leads to a change of crystal

structure from cubic to tetragonal. When the temperature is below 278 K, the preferred displacement direction of atoms changes (from $\langle 100 \rangle$ to $\langle 110 \rangle$) and the structure converts to orthorhombic; below 183 K it converts to trigonal (with $\langle 111 \rangle$ displacements).⁶ The direction of atomic displacement determines the polarization direction. This critical transformation temperature from ferroelectric to non-ferroelectric is called the Curie temperature (T_c).^{5,7} The high temperature phase that transforms to the ferroelectric below T_c is termed a paraelectric.⁶

A depolarization field arises in a domain having a spontaneous polarization, because of the non-uniform polarization throughout the ferroelectric can be neutralized by the flow of free charge within the crystal or absorbed ions in the surrounding medium.^{6,8} The polarization is temperature dependent and can be detected by observing the flow of charge to and from the surfaces on change of temperature, which is called the pyroelectric effect.⁶ It should be noted that polar terminations of some crystals can also result in compensating surface charges.

2.1.1.3 Domains

To minimize the depolarization fields, the direction of the polarization varies from region to region of the crystals. Any region having a locally uniform polarization is called a domain; the boundary separating two domains is called a domain wall.⁹ The size of a domain is determined by minimizing the overall deformation and the electrostatic energies.³ Domain walls are often described relative to the angle formed between the polarization vectors on either side of the wall. In tetragonal BaTiO_3 ,

where the polarization directions are along the pseudocubic $\langle 100 \rangle$ directions, domain walls can be either 90° or 180° . The 90° and 180° domain walls are shown in figure 2-2. In this figure, “ c^+ ” and “ c^- ” refers to domains with polarization vectors along (+) and (-) z direction (vertical), respectively, while “ a^+ ” and “ a^- ” represents domains along the a axis (horizontal).

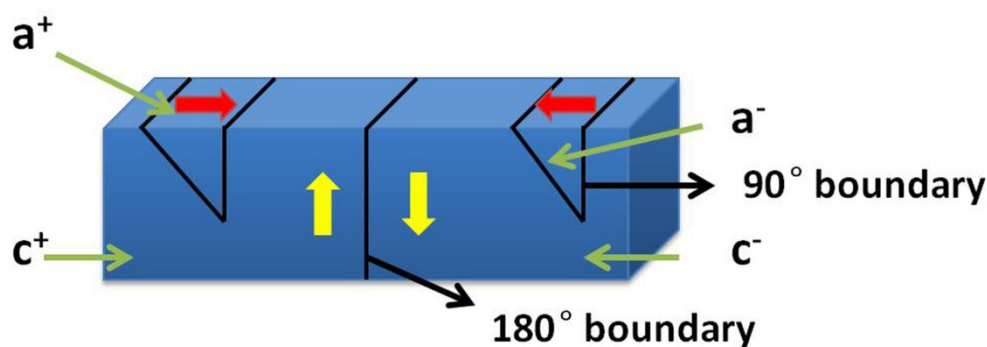


Figure 2-2 Schematic of domains in a ferroelectric crystal. (This figure is reproduced from reference 9.)

2.1.1.4 Size Effect on Ferroelectrics

For photocatalyst design, it is necessary to understand the influence of crystal size on the ferroelectric properties. It is known that the measured spontaneous polarization decreases with decreasing particle size in the nanoscale size range. Figure 2-3¹⁰ and figure 2-4¹¹ shows the size effect on spontaneous polarization for two common ferroelectrics, BaTiO_3 and PbTiO_3 (both investigated herein too). It is reported that the ratio of the lattice constant of the c-axis to that of the a-axis decreases with the decreasing particle size.^{12,13} One interpretation of this observations is that, as the particle size decreases, a gradual loss in covalent character of Ti-O

bonds occurs and this results in a loss of the tetragonality in the lattice. Therefore, the spontaneous polarization, involving cooperative noncentrosymmetric displacements of ions in the neighboring unit cells, is decreased.¹⁰

In addition, many other ferroelectric properties are size dependent. For instance, the initial piezoelectric hysteresis loop of a ferroelectric also has a negative shift with the decreasing of particle size.¹⁴ The unit-cell volume of tetragonal BaTiO₃ powders increases as particle size decreases (agreeing with the loss of covalency character).^{11,15} The dielectric constant of ferroelectric ceramics with smaller grain sizes also decreases significantly.¹⁶

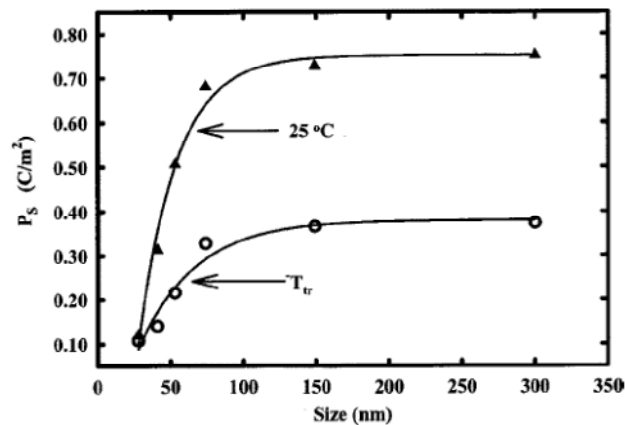


Figure 2-3 Variation of spontaneous polarization at transition (P_s) and at 25 °C (P_3) with particle size for PbTiO₃. (This figure is reproduced from reference 10.)

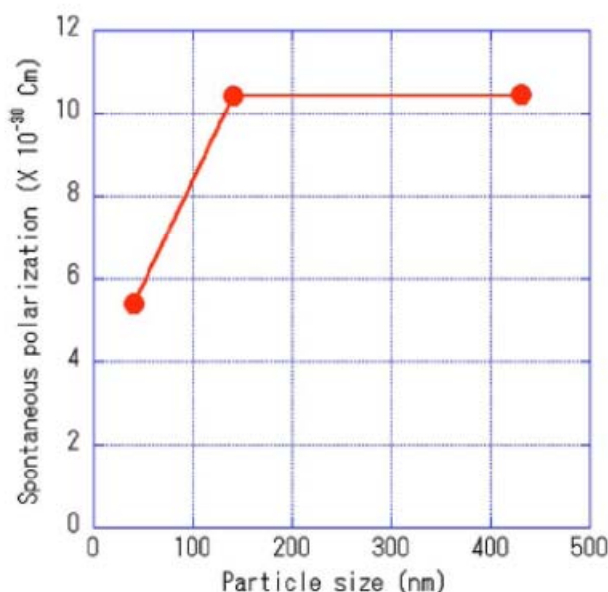


Figure 2-4 Size effect on the spontaneous polarization of single domain tetragonal BaTiO₃. (This figure is reproduced from reference 11.)

2.1.2 Surface Termination

Surface structure is quite important for physical and chemical properties of materials. The atoms at the surface have different coordination numbers than those in the bulk, often resulting in dangling bonds at the surface. In the case where occupied and unoccupied dangling bonds exist at high densities, they can overlap to form bands.¹⁷ Surface atoms also have higher energies than the atoms in the bulk. As such, the surfaces adsorb cations and anions from the surrounding environment to reduce the energy, likely satisfying residual bonding issues of the surface atoms too.

This dipolar field has great influence the photocatalytic activity of materials. Our group has shown the photochemical reduction of Ag⁺ and oxidation of Pb²⁺ on the surface of SrTiO₃ is anisotropic.¹⁸ The dipolar field created by a polar surface termination can promote the separation of photogenerated charge carriers and

spatially selective of oxidation and reduction. As shown in figure 2-5,¹⁸ the two images in the upper half are the AFM topographic images of surfaces of a (111)-oriented SrTiO₃ single crystal before and after photochemical reduction reaction. During this procedure, silver nitrate was reduced to produce solid silver on top of a SrTiO₃ surface under UV-visible light illumination. The final result shows residual silver is only observed to deposit on specific terraces, which means the photochemical reduction is spatially separated. This was explained by the reason that the bulk-truncated ideal (111) surface of SrTiO₃ can only be terminated by negative charged SrO₃⁴⁻ surfaces or positive charged Ti⁴⁺ surfaces, as shown in the figure 2-6 down side. These charged surfaces form the dipolar field, which separates the electrons and holes and promote the spatially selection of reduction reaction. The same experiment was performed on (100) surfaces, which can only be terminated by neutral charge SrO surfaces and TiO₂ surfaces. The final result shows the silver reduction is deposited uniformly.

The influence of polar surface terminations on the photocatalytic activity of SrTiO₃ and Fe₂O₃ was also evinced from other experiments. 50 nm Fe₂O₃ films supported on the (111) surface of SrTiO₃ show enhanced photochemical reactivity for silver reduction under visible light when compared to bulk Fe₂O₃ and a similar Fe₂O₃ film supported on (0001) Al₂O₃.¹⁹ It was argued that the internal fields created by the polar surface terminations of SrTiO₃ increased the reactivity of the (0001) surface of the film. Further research on bulk Fe₂O₃ indicated that a combination of electronic structure and surface charge could explain why the (1 $\bar{2}$ 10) prismatic planes were the

most reactive of all surface orientations.²⁰

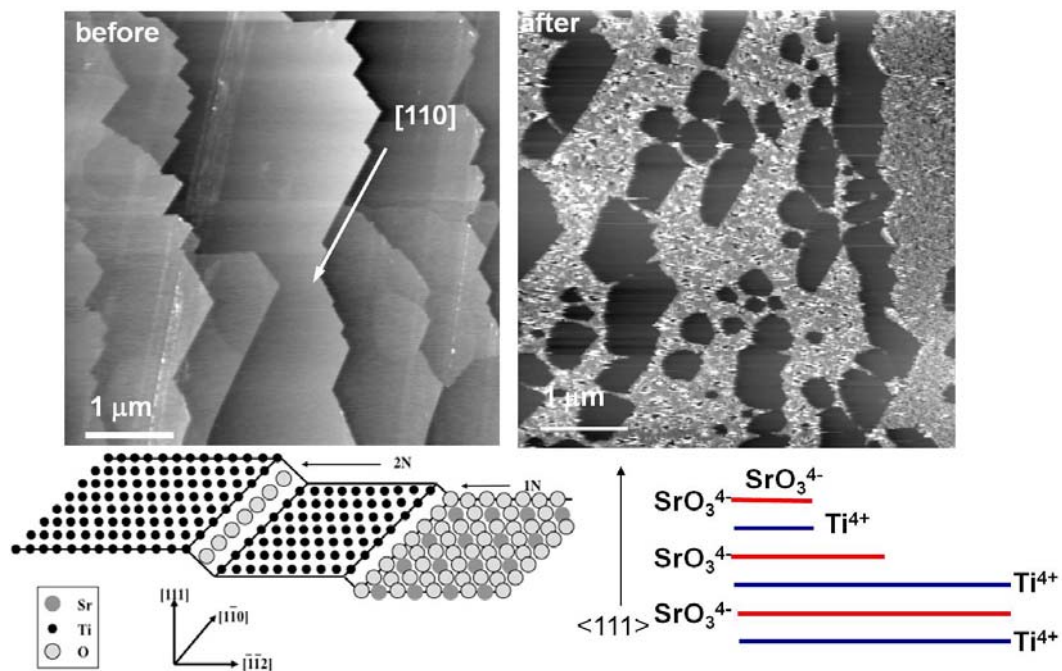


Figure 2-5 The influence of dipolar field created by polar surface termination on the photochemical reactivity of SrTiO₃. (This reference is reproduced from the reference 18.)

2.1.3 P-N Junctions

A p-n junction is formed in the boundary region between a p-type and a n-type semiconductor. When p-type and n-type semiconductors contact each other, charge is transferred so that the Fermi levels equilibrate. At the interface of the semiconductors, bands will bend owing to the formation of space charge regions after electron transfer. An electric field is created in the space charge region to screen the diffusion of electrons and holes with the semiconductors. A schematic is shown in figure 2-6. This internal field formed between a p-type and a n-type semiconductor also can be used for the separation of photogenerated charge carriers (and to improve the efficiency of water photolysis).

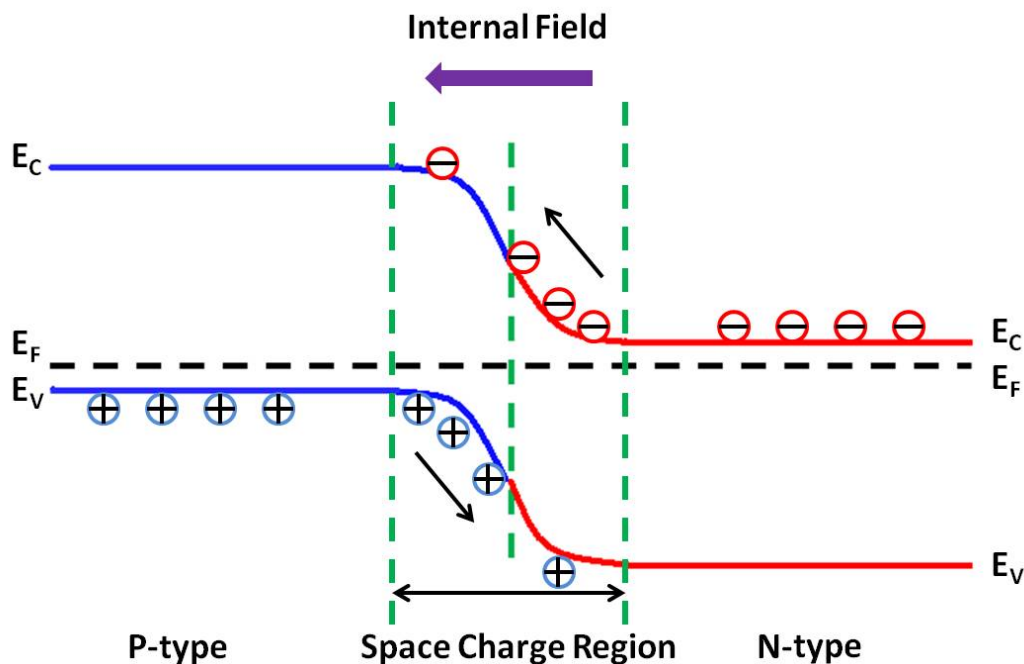


Figure 2-6 The schematic of p-n junction formation between two semiconductors without the applied external voltage.

2.2 Photocatalysts

2.2.1 Principle of Photocatalytic Water Splitting

Since the discovery by Fujishima and Honda in 1972,²¹ there have been many advancements toward the discovery of a suitably efficient photocatalyst. In general, water splitting is mostly accomplished using semiconductors, though novel metals and polymers have been combined with semiconductors to improve photocatalytic activity. The mechanism for photocatalytic water splitting with a semiconductor is illustrated in figure 2-7.²² In this figure, water photoelectrolysis is chosen to explain the mechanism of water splitting, which is also applicable to water photolysis with

semiconductor powders. As described before, when the photocatalyst is illuminated by photons with energy greater than its bandgap, electrons are excited to the conduction band from the valence band and move to participate in the reduction reaction. The remaining holes are driven to the surface to participate in the oxidation reaction.

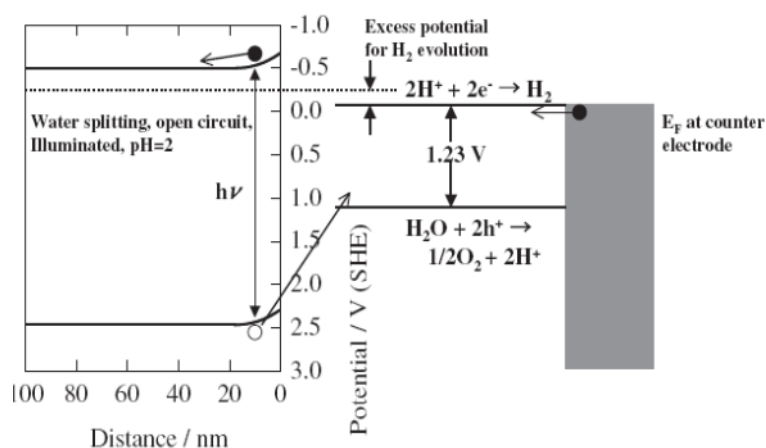


Figure 2-7 Schematic representation of water photoelectrolysis using illuminated oxide semiconductor electrode. (This figure is reproduced from reference 22.)

Figure 2-8 schematically illustrates the primary processes for water photolysis.²³ The whole process can be divided, generally, into three parts: photon absorption and carrier excitation, separation of photoinduced carriers and their bulk transport, and surface transfer / reaction of photoinduced carriers. These three processes control the efficiency of photocatalytic water splitting and are the focus for design of new efficient photocatalysts.

The first step for photocatalysis in the illuminated semiconductor is light absorption and then excitation if the photon energy exceeds the bandgap energy of semiconductors. The band gap and band-edge energies must satisfy certain criteria to split water. The electron energy (conduction band edge) must be above the redox level

for hydrogen production (0 V on the SHE scale), while the hole energy (valence band edge) must be below the oxygen redox level (1.23 V on the SHE scale). Obviously, the band gap of useful photocatalysts must be larger than 1.23 V (the difference in the relevant redox levels on the SHE scale). In view of the kinetics of the reactions, the conduction (valence) band edge should be above (below) the relevant potential by 0.4 V to 0.8 V. Therefore, a realistic value for the minimum band gap (assuming the midgap state is 0.66 eV below H on the SHE scale) of photocatalysts for water splitting is between 2.0 eV and 2.5 eV.¹⁷

The relationship between the band edge energies of semiconductors and the redox potentials for water splitting is shown in figure 2-9.²⁴ From this figure, it can be implied that silicon itself is not suitable for photocatalytic water splitting due to the band gap energy. Considering the cost and scarcity of some elements, such as Ga or In, as well as toxicity and concomitant environmental issues, oxide semiconductors are the primary choice for photocatalyst materials for hydrogen production.²⁵ (Note that the transfer of electrons from the solid to the water is essentially part of process 3, but it makes sense to discuss band edges here for clarity and conciseness).

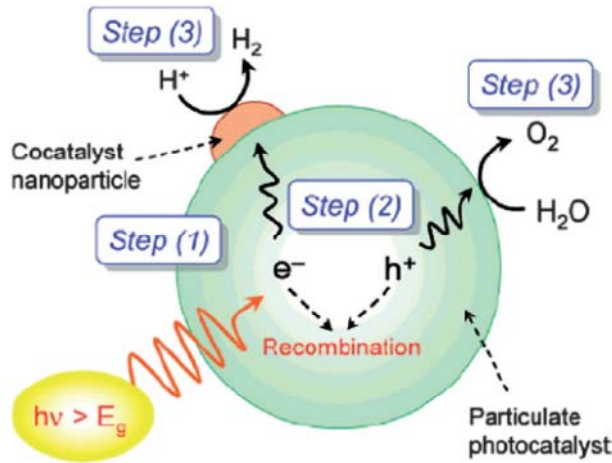


Figure 2-8 Main processes in photocatalytic water splitting. (This figure is reproduced from reference 23.)

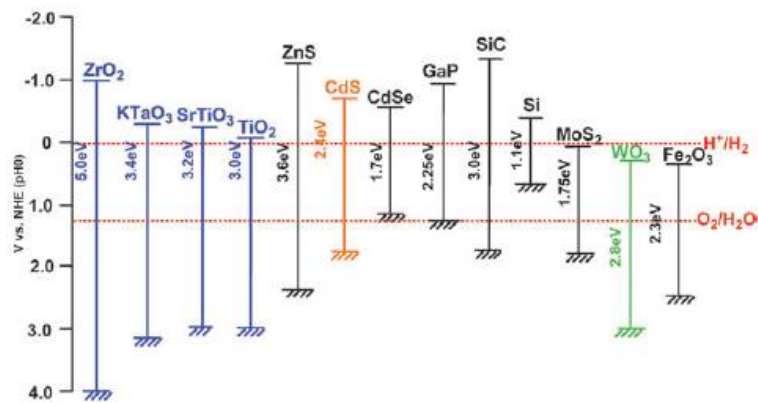


Figure 2-9 Schematic representation of relationship between band structure of semiconductor and redox potential. (This figure is reproduced from reference 24.)

If one considers the energy distribution in the solar spectrum, which is shown in table 2-1,²⁶ it can be concluded that only 30% of the solar energy can be utilized for realistic water splitting. Actually, the solar utilization efficiency is even lower than this value because of thermodynamic losses from electron and hole recombination. Therefore, one important aspect of photocatalyst selection and design is bandgap engineering, which focuses on the fabrication of materials or composites with suitable bandgaps to harvest as much solar energy as possible.

Table 2-1 Energy distribution in the terrestrial solar spectrum (AM 1.5). (This table is reproduced from reference 26.)

Spectral region	Wavelength (nm)	Energy (eV)	Contribution to total spectrum (%)
near-UV	315-400	3.93-3.09	2.9
blue	400-510	3.09-2.42	14.6
green/yellow	510-610	2.42-2.03	16.0
red	610-700	2.03-1.77	13.8
near-IR	700-920	1.77-1.34	23.5
infrared	920->1400	1.34-<0.88	29.4

The second process is the separation of photoinduced carriers and their bulk transport. Several factors have an influence on this process, discussed here in no particular order. Also note, that it is difficult to completely isolate each process, so when other processes are also affected by the factor they may be discussed here for simplicity.

One factor is the particle size. The influence of particle size on photocatalytic water splitting is illustrated in figure 2-10.²⁷ Nanoparticles have the advantage of having large surface areas and a large fraction of atoms at the surface in contact with the solution, which means more active sites per volume for hydrogen production (process three). Smaller sizes also mean shorter distances for photogenerated charge carriers to migrate before reaching surface reaction sites, potentially further improving performance.²⁷⁻²⁹ When the particle size is smaller than the space charge region width of bulk materials, which is not larger than 100 nm for TiO₂,³⁰ the space charge region is narrowed and bands cannot extend fully to the bulk level. Keeping in mind that the space charge region is the location where the photogenerated charge carriers are separated by an electric field, the narrower space charge region means the potential drop for charge carrier separation is smaller (assuming potential at the

surface is the same), as is shown in figure 2-11.³¹ Therefore, the recombination rate for photogenerated charge carriers increases with the decrease of particle size in the nano-range. Smaller sizes also tend to lead to increased recombination rates owing to increased probability of collision; since the possibility of recombination is simply the probability that an electron and hole will encounter one other, then recombination will increase with the inverse of particle volume.³² So the performance will be a trade off between the negative impacts of increased recombination rates and decreased electric fields and positive impacts of smaller transport distances and larger surface areas.

Another effect of particle size is that, as the size decreases to the nanoscale range, the conduction and valence band edge move apart and the bandgap of the semiconductor increases owing to quantum confinement size effects.³³⁻³⁵ A larger bandgap means less solar energy is harvested. Similar effects are observed near the surfaces of all particles. To sum up, the change of particle size has both positive as well as negative influences on photocatalytic activity and it is necessary to optimize the particle size for a specific reaction system to balance the various effects.

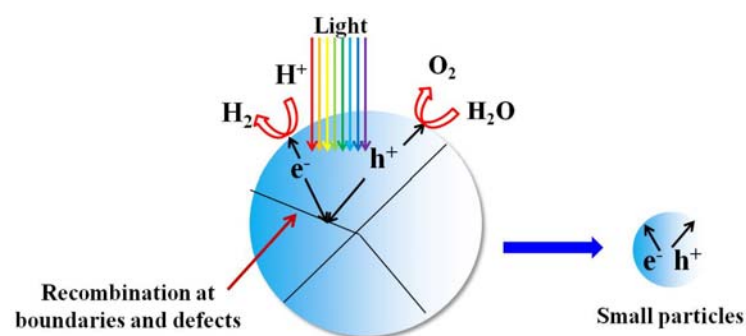


Figure 2-10 Effect of particle size and boundary on photocatalytic activity. (This figure is reproduced from reference 27.)

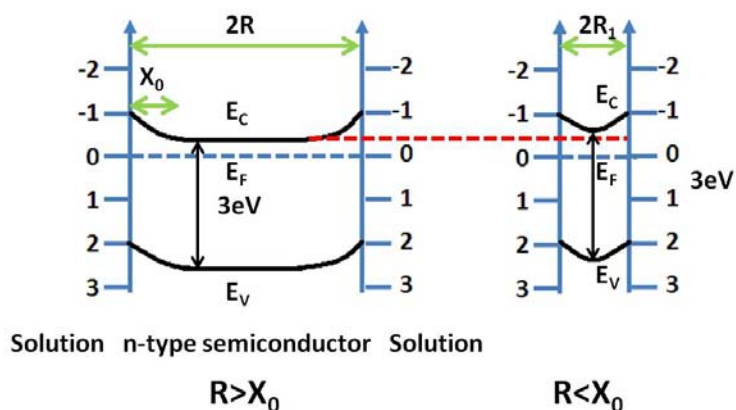


Figure 2-11 Band Structure of n-type semiconductor with different particle size. (This figure is reproduced from reference 31.)

The crystal structure and the level of crystallinity also affect the charge recombination rate, and therefore bulk transport. TiO_2 , the most commonly used photocatalyst, has three common crystalline polymorphs, namely anatase (tetragonal), rutile (tetragonal), and brookite (orthorhombic); it can also be easily fabricated as an amorphous solid. Anatase and rutile are generally regarded to be photocatalytic whereas brookite is not.^{36,37} Anatase is reported to have a higher photocatalytic activity than rutile because of the lower rate of charge carrier recombination (process two) and more negative conduction band position (process one and three).^{38,39} However, rutile displays the same effective photocatalytic decomposition of pollutants.⁴⁰ It has been reported that mixtures of rutile and anatase exhibit enhanced photocatalytic activity compared to the same isolated materials. This has been explained by increased light absorption in rutile (process one) and the transfer of photogenerated electrons to trapping sites in anatase (process three), which decreases the recombination of photogenerated charge carriers (process two).⁴¹ In general, higher crystalline quality of any of these polymorphs mean fewer defects in the

photocatalyst, which are regarded as electron-hole recombination centers, and should lead to improved bulk transport.²⁷ Because the crystal structure of TiO₂ and the crystalline quality are both closely related to the preparation method and processing temperature, these effects are often coupled. The transformation temperature from anatase to rutile is in the range of 500 °C to 600 °C.⁴²⁻⁴⁴

The third process, the transfer of photoinduced charge carriers to the surface where they react, is enhanced by cocatalyst loading to provide abundant active sites and decrease the activation energy for hydrogen and oxygen evolution.⁴⁵ Pt, NiO, and RuO₂ are the most common cocatalysts to produce hydrogen because the conduction band levels of many oxide photocatalysts are not high enough to reduce water to produce hydrogen without catalytic assistance.²⁷ Currently, composite cocatalysts are designed to enhance photocatalytic activity for hydrogen production. The photocatalyst with the greatest quantum efficiency for water splitting using visible light is a GaN-ZnO solid solution with a core-shell co-catalyst shown in figure 2-12.⁴⁵⁻⁵⁰ Moreover, a cocatalyst also can promote the back reaction of hydrogen and oxygen to re-form water. The loading of cocatalysts should be optimized to obtain the most efficient catalysis.²⁷

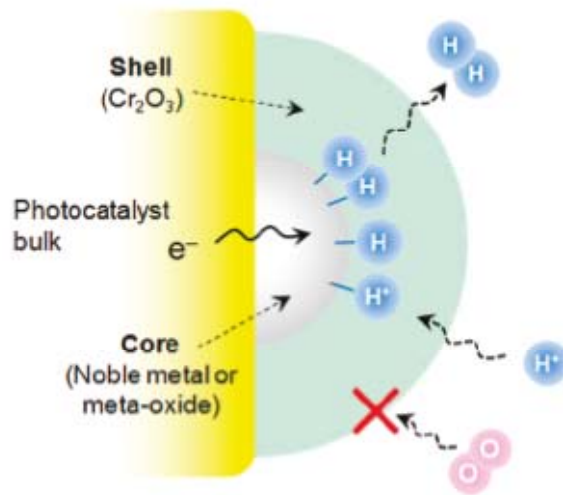


Figure 2-12 Schematic illustration of H₂ evolution on core/shell-structured nanoparticles (with a noble metal or metal oxide core and a Cr₂O₃ shell) as cocatalyst for photocatalytic overall water splitting. (This figure is reproduced from reference 45.)

In addition to the three processes described for photocatalytic water splitting, another point for photocatalyst design and selection that should be considered is the chemical stability of the photocatalyst to corrosion and photocorrosion in the aqueous environments.²⁶ A number of photocatalysts have high visible light activity for water splitting but are prone to decomposition in photolysis environments, and therefore they lose photocatalytic activity in a short time.^{51,52} Unstable materials can only be utilized as photocatalysts if they are suitably protected from degradation.

2.2.2 Visible Light Harvesting

Nowadays, research on photolysis is focused either on improving photoelectrochemical cells or photolytic properties of powders for photocatalytic hydrogen production from water using sunlight. Based on table 2-1, visible light makes up a large percentage of the solar spectrum. However, the band gap energy of

the most common photocatalyst, TiO_2 , is approximately 3.0 eV for rutile and 3.2 eV for anatase.⁵³ Therefore, the wavelengths of irradiation that can be absorbed by TiO_2 will be less than 410 nm, the majority of which is in the UV range. In order to absorb more of the solar spectrum, many attempts have been made to modify the photocatalyst so that it absorbs visible light. The most common way is chemical doping. Metal ions with partially filled d-orbits, such as V^{5+} ,⁵⁴ Cr^{3+} ,⁵⁵ Fe^{3+} ,⁵⁶ and Mo^{3+} ,⁵⁷ substitute for titanium (Ti^{4+}). Another strategy to dope TiO_2 for visible light absorption is to replace the oxygen anion (O^{2-}) with another electronegative atom, such as N,⁵⁸ S,⁵⁹ C,⁶⁰ and F.⁶¹ Doping is aimed at forming new electronic states within the forbidden gap of TiO_2 to lower the threshold energy required to light absorption. One problem with this is that substitutional elements act as scattering centers, and this may decrease the photocatalytic activity even if more light is absorbed.^{62,63}

The second method for modifying wide band gap photocatalysts to absorb visible light is to use dye sensitization. This method was greatly improved by O'Regan and Grätzel in 1991 and has been widely developed for use in so-called dye-sensitized solar cells.⁶⁴ This low cost solar cell has achieved high solar energy conversion efficiency (12%) in diffuse daylight. This method was also extended for water splitting to produce hydrogen.⁶⁵⁻⁶⁷

Figure 2-13 is a simple schematic of the principle for dye sensitized photocatalytic hydrogen production from water.⁶⁶ Based on this figure, the primary component for light absorption in the whole system is the organic dye. Under visible light irradiation, the electrons are injected into the conduction band of the

semiconductor photocatalyst and then reduce the water to produce hydrogen on the surface of photocatalyst. The addition of a metal cocatalyst, such as Pt, can promote hydrogen production (which is not shown in the figure). The excited sensitizer molecules are regenerated by the electrons donated by water. Some sacrificial reagent, such as EDTA, can replace water to be used as the electron donor, and this sacrificial system can also be beneficial for hydrogen evolution.⁶⁸ Another way of using dye sensitization to improve the efficiency of photocatalytic water splitting is to connect one photosystem, which is active for oxygen evolution, with a dye sensitized TiO₂ cell, which is active for hydrogen evolution. The whole reaction system is analogous to the Z-scheme of photosynthesis that occurs in green plants.⁶⁹

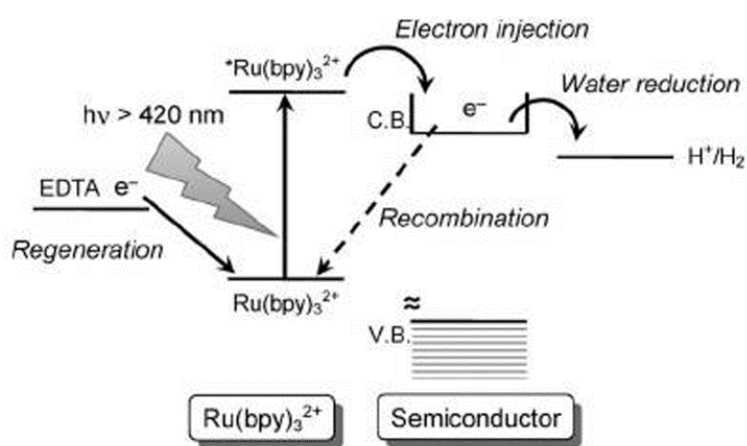


Figure 2-13 Schematic illustration of dye-sensitized hydrogen production from water. (This figure is reproduced from reference 66.)

Another strategy to extend the absorption of TiO₂ to the visible light region is by coupling with other narrow band gap semiconductors or forming the solid solution to absorb the visible light.⁷⁰⁻⁷⁴ The coupling of different semiconductors can be employed to improve photocatalytic activity under visible light as well as UV irradiation. As shown in figure 2-14,⁷⁵ the p-type BiOI with a narrow band gap energy

(1.79 eV) was coupled with anatase (3.02 eV) and the composite was illuminated under visible light (wavelength larger than 420 nm). TiO₂ cannot absorb photons of this energy. The photogenerated electrons absorbed by BiOI with a more negative conduction band are injected into the lower conduction band of TiO₂. Hence, more efficient charge-carrier separation is achieved and the composite displays an enhanced photocatalytic activity for decomposition of organic pollutants.

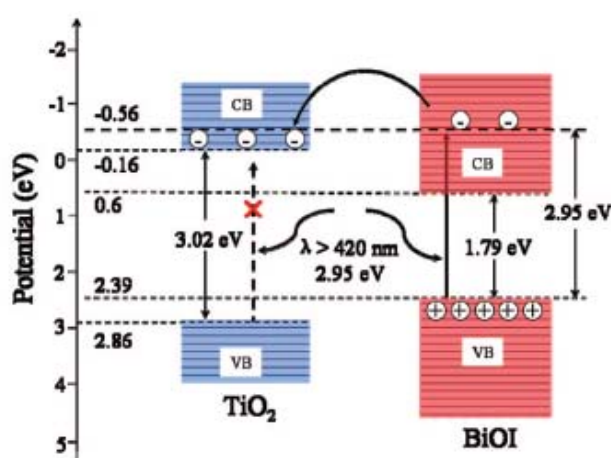


Figure 2-14 Schematic for the mechanism of charge separation for coupled semiconductors. (This reference is reproduced from reference 75.)

The method of coupling TiO₂ with a narrow bandgap semiconductor for visible light absorption inspired the current study of the design and fabrication of efficient composite photocatalysts. Section 2.3 will focus on mechanisms for the design of TiO₂ based heterostructures and also contains a brief introduction to relevant processing methods.

2.2.3 Sacrificial Solutions for Water Splitting

Because of the difficulty of splitting pure water directly, some sacrificial solutions have been employed to promote hydrogen or oxygen production and

increase photocatalytic efficiency. The sacrificial reagents can scavenge holes better than water, and the better collection suppresses the electron-hole recombination (and more electrons can participate in reduction reactions on the photocatalyst). Therefore, hydrogen production is enhanced. Similarly, oxygen is more apt to evolve with the assistance of electron scavengers in the solution. While sacrificial reactions are employed in most photocatalytic research to test the photocatalytic activity of semiconductors, it is not equivalent to overall water splitting.^{27,76}

The most common sacrificial reagent, methanol, is also used in the current work. Other promising electron donors are ethanol,^{77,78} EDTA,⁷⁹ CN⁻,⁸⁰ lactic acid.⁸¹ It has been reported that the enhancement capacity for hydrogen production of various reagents is EDTA > methanol > ethanol > lactic acid.^{82,83} However, it has also been reported that methanol is the most efficient sacrificial solution for promoting hydrogen production.⁸⁴ In general, organic pollutants also can provide electrons and increase the efficiency of hydrogen production.^{83,85}

Reversible electron mediators are another type of sacrificial reagent that can be used for overall water splitting. In this case, both electron and hole donors exist simultaneously. They can act as redox mediators. Figure 2-15 depicts the mechanism of photoinduced charge transfer between the spatially separated illuminated semiconductors.⁸⁶ In this shuttle charge transfer system, Ce³⁺ can be oxidized to be Ce⁴⁺ on the hydrogen producing catalyst and Ce⁴⁺ reduced to Ce³⁺ on the oxygen producing catalyst. The characteristic feature of this shuttle system is that the redox reactions proceed in spatially separate locations for the overall water splitting, which

can decrease the recombination of charge carriers and suppress the back reaction of intermediates.^{87,88} This two step water splitting process is similar to the photosynthesis by green plants and is promising for the conversion of solar energy. In addition, the Ce^{3+}/Ce^{4+} pair mediators are stable in the aqueous system under irradiation.⁸⁶ Similar redox mediator pairs are I^-/IO_3^- ,⁸⁹⁻⁹¹ Fe^{2+}/Fe^{3+} ,^{92,93} Br_2/Br^- .⁹⁴

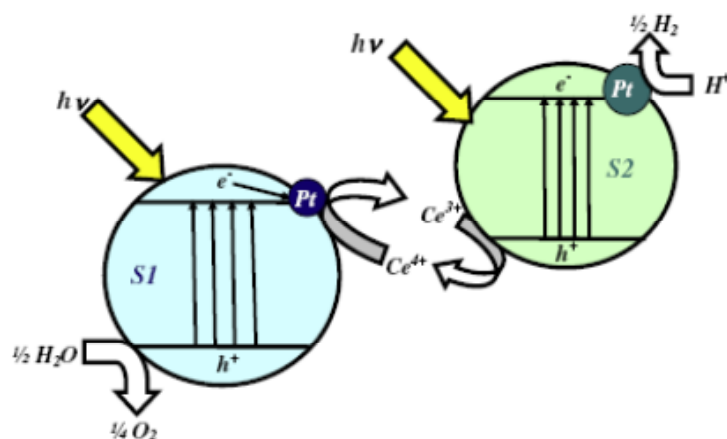


Figure 2-15 Scheme of photoinduced charge transfer on the surface of spatially separated illuminated semiconductors S1 and S2. (This figure is reproduced from reference 86.)

Sometimes, carbonate salts, like Na_2CO_3 and $NaHCO_3$, are added to the aqueous solution to suppress the back reaction and increase hydrogen production.^{95, 96} The carbonate species can react with photogenerated holes to separate them from the electrons. The mechanism of CO_3^{2-} and HCO_3^- promoting photocatalytic water splitting is shown in the following:⁸³

- (1) $CO_3^{2-} + H^+ = HCO_3^-$
- (2) $HCO_3^- + h^+ = HCO_3\cdot$
- (3) $HCO_3\cdot = H^+ + CO_3\cdot^-$
- (4) $CO_3\cdot^- = C_2O_6^{2-}$
- (5) $C_2O_6^{2-} + 2 h^+ = O_2 + CO_2$

Carbon dioxide produced from the above reaction is then dissolved into water to form carbonate ions. Meanwhile, the photogenerated hole is consumed. However, adding excess carbonate can decrease photocatalytic hydrogen production because absorbed carbonate ions on the surface of the photocatalyst affects the absorption of solar light.⁹⁷

The common hole donors for oxygen production are Ag^+ and Fe^{3+} . Analogous to electron donors, the oxidizing reagents are utilized to react with photogenerated holes to promote oxygen evolution. Several papers about this topic can be found in the references.⁹⁸⁻¹⁰⁰

2.2.4 Photocatalytic Activity Characterization

As discussed in Chapter 1, the primary methods for photocatalytic water splitting are photoelectrolysis using photoelectrochemical cells (PECs) and photolysis using particulate semiconductors. The photoelectrochemical cell is one of the primary characterization methods for photocatalytic activity. The primary photocatalytic activity characterization for PECs is the measurement of photocurrent and photovoltage induced from irradiation.^{101,102} Hydrogen production by photoelectrolysis is also used to quantify a PEC's photocatalytic performance.

The second way to evaluate the reactivity of a photocatalyst is to decompose an organic pollutant. This characterization is more commonly utilized when the application is water treatment and detoxification.¹⁰³ The mechanism of photocatalytic

degradation of organic pollutants is shown by the following reaction. (R-H represents organic pollutant):¹⁰³

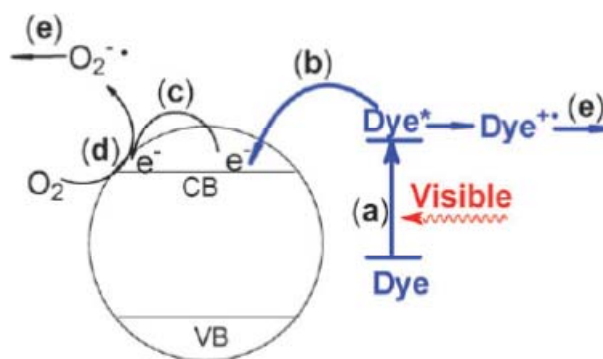
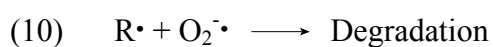
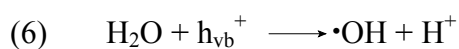


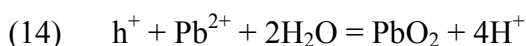
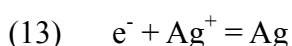
Figure 2-16 The semiconductor-mediated photodegradation initiated by the surface electron injection from the adsorbed dye molecules that harvest visible light. (This figure is reproduced from reference 103.)

Similar to photocatalytic water splitting, photogenerated electrons in the semiconductor can be excited to the conduction band, leaving holes in the valance band. The holes in the valance band react with water to form hydroxyl radicals or react with the organic pollutant (such as dye) to form radicals. The excited electrons react with oxygen to produce superoxide radicals. The superoxide and hydroxyl radicals are the primary effective groups to oxidize organic pollutants.¹⁰⁴

Simultaneously, dye can be employed to harvest light to extend the photocatalytic

activity into visible light region. The dye absorbs visible light and excited state electrons injected into the conduction band of the semiconductor can be trapped by surface active sites and participate in surface reactions to produce superoxide radicals, which then react to decompose the dye. These processes are illustrated schematically in figure 2-16.¹⁰³ Based on this mechanism, Grätzel created the dye-sensitized photovoltaic cell.^{64,67}

Another way to characterize a photochemical reaction is to use a marker reaction. In this case, photogenerated electrons and holes arising from the bulk photocatalyst react with the solution to produce an insoluble reaction product, which “marks” the surface of photocatalyst and can be observed microscopically or by other analytical techniques. The most common reagents employed are AgNO_3 for the reduction reaction and $\text{Pb}(\text{CH}_3\text{COO})_2$ for the oxidation reaction.^{18,105-107} The photocatalytic marker reactions are:



Other characterization methods involve the destruction of gas phase pollutants for air treatment,¹⁰⁸ photocatalytic disinfection,¹⁰⁹ and photocatalysis for organic synthesis such as the photoreduction of CO_2 to useful hydrocarbon products.¹¹⁰ As this discussion indicates, photocatalytic technologies have a wide range of applications in the environmental and energy fields.

2.2.5 Current TiO₂ Research as Photocatalyst and Approaches for Charge Carrier Separation

Of all the materials that promote photolysis, TiO₂ still attracts the most interest because it has a workable balance of the necessary materials properties.¹¹¹⁻¹¹³ Figure 2-17 shows the distribution of current scientific research on photocatalytic hydrogen production.¹¹⁴ This data in this pie chart implies that more than a third of photocatalyst research is focused on TiO₂.

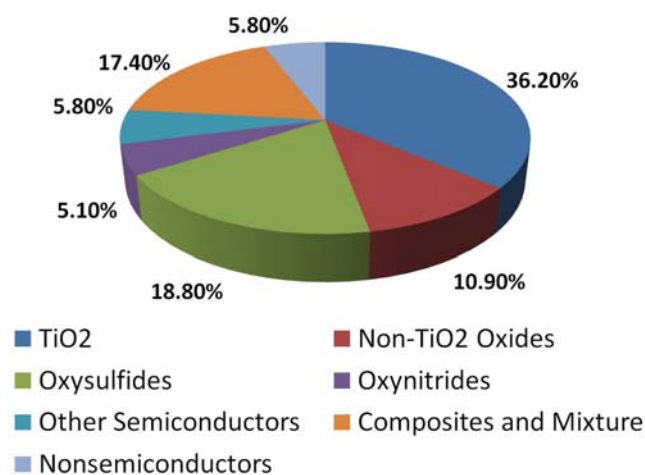


Figure 2-17 Distribution of scientific publications focusing on nanomaterials for photocatalytic hydrogen production. (This figure is reproduced from reference 114.)

Titanium is the ninth most abundant element in the Earth.³⁷ Industry produces TiO₂ from ilmenite (FeTiO₃), which is quite common and is found in large deposits in many countries. The abundant raw materials and relatively simple processing mean that TiO₂ is inexpensive. In general, TiO₂ is thought to have low toxicity although research in this area is ongoing.

TiO₂ is an n-type semiconductor, that is, mainly donor-type defects, involving oxygen vacancies and titanium interstitials, are responsible for the electronic

conductivity.¹¹⁵ However, current studies show that prolonged oxidation of TiO₂ at elevated temperatures (1323 K and 1123 K) with subsequent rapid cooling leads to the formation of titanium vacancies, which means TiO₂ at room temperature displays p-type conductivity.^{116,117} This represents progress in the control of the electrical properties for TiO₂, which is of great importance to the design of semiconductors for photoelectrochemical and photolytic applications.

As discussed in Section 2.2, efficient separation of photogenerated electrons and holes are important to improve the efficiency of photocatalysts for water splitting. The current approach for charge carrier separation is focused on the following directions: cocatalyst loading, modification of crystal structure, modification of size and morphology, and different semiconductor combinations.⁷⁴ The Fermi level of the metal cocatalyst is generally smaller than the conduction band energy of the semiconductor photocatalyst, and thus the cocatalyst can entrap the photogenerated electrons and decrease the recombination of charge carriers. Meanwhile, the loading of the cocatalyst can decrease the adsorption energy of H⁺, which increases the efficiency for hydrogen evolution.⁷⁴ As discussed in Section 2.2, the photocatalytic activity of particulate semiconductor photocatalysts is also dependent on particle size and crystallinity. Currently, the influence of photocatalyst morphology on photocatalytic activity is widely studied. Different morphologies can lead to an increase of the surface area, which can provide more activate sites for water splitting. In other words, different morphologies show differences in the separation of photogenerated charge carriers.¹¹⁸ Different nanostructures, such as one-dimensional

(1D) nanotube/nanowire/nanorods and two-dimensional (2D) nanoplate/nanosheet,¹¹⁹⁻¹²¹ are widely reported to have increased photocatalytic activities. Three-dimensional (3D) nanostructures are also a hot topic in photocatalyst research.^{122,123} Their application as photocatalysts for hydrogen production is considered as promising. However, the mechanisms by which the different morphologies promote the separation of photogenerated charge carriers are unknown and need to be further explored.

The structures of the facets that terminate catalyst particles are thought to influence the process of charge carrier separation.¹²⁴⁻¹³⁰ The surface atomic arrangement, atomic coordination, and surface energy influence the adsorption of reacted molecules, electron separation and transfer, product desorption, and, ultimately, the overall photocatalytic reactivity.^{124,130} These are the reasons why different planes show different photocatalytic activities. Therefore, tuning the ratio of different facets can control the photocatalytic activity. For example, (101) planes of anatase TiO₂ are considered as more reactive than (001) in photooxidation reactions for OH radical generation and photocatalytic hydrogen evolution. Anatase powders with different percentages of (101) facets have been synthesized by HF etching.¹²⁵

Composite formation is another approach for charge carrier separation. The synergistic effect between semiconductors with different physical and chemical properties, such as band gap energy, can decrease the recombination of photogenerated electrons and holes and thus increase the photocatalytic activity. For example, the incorporation of semiconductors into the interlayers of lamellar

structured photocatalysts to suppress the recombination of charge carriers has been studied.⁷⁴ Encapsulation of semiconductors into a micro/mesoporous structure to promote photogenerated charge carrier separation is another way to combine semiconductors.^{131,132} Mesoporous TiO₂ with WS₂ nanoparticles in the channels was reported to show increased visible light photocatalytic activity because of efficient charge carrier separation.¹³³ To sum up, different semiconductor combinations are widely studied and this method is considered as one of the best ways to promote charge carrier separation.

2.3 Heterostructured Photocatalyst Design

There are two important design goals for heterostructured photocatalysts that will be considered here. First, they should separate photogenerated charge carriers and intermediate chemical species. Second, they should absorb visible light. Photoelectrochemical systems attract our attention because they separate the reactants and use an internal voltage to separate the photogenerated electrons and holes over macroscopic distances. The ultimate aim in photolysis is to achieve a particle equivalent of the photoelectrochemical cell.¹³⁴ One of the goals of this dissertation is to demonstrate that it is possible to control, in a composite particle, the length scales for light absorption, charge separation and transfer, and photochemical reaction by using nanostructured coatings supported on microcrystalline core powders, moving towards the emulation of photoelectrochemical systems in heterostructured catalysts.

2.3.1 Dipolar Field Effect

The internal dipolar field creates charged surfaces on ferroelectrics that cause the photogenerated carriers to move in the opposite directions,¹³⁵ which can assist separating electrons and holes for redox reactions and cause oxidation and reduction products to be generated at different locations. We call this the dipolar field effect.

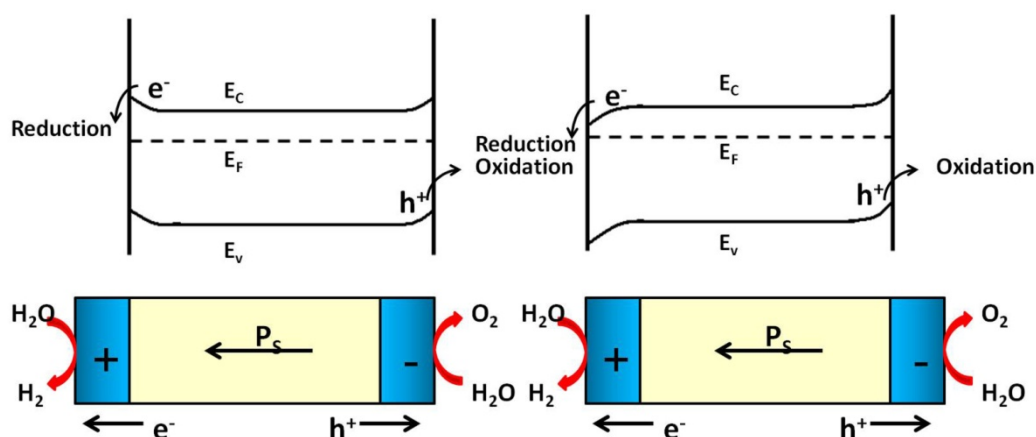


Figure 2-18 Band bending in a polarized crystal. (a) Band bending due to insufficient positive surface charge. (b) Band bending for the crystal in the case of net positively and negatively charged surfaces. (This figure is reproduced from reference 2.)

Figure 2-18² depicts the mechanism of the dipolar field effect. The internal polarization in the polarized crystal is screened by internal free charge carriers or defects in the bulk, which causes band bending on the ferroelectric surface.¹³⁶ On a surface of negative polarity, the electrons are repelled from the surface and the bands will bend upwards to form a depletion layer, which obstructs electrons from moving toward the surface but promotes the movement of holes toward the surface where they can participate in the oxidation reaction. On a surface of positive polarity, the bands will still bend upwards if there is not sufficient positive surface charge to balance the excess electrons on the n-type semiconductor. Electrons with sufficient energy to

overcome the barrier can participate in reactions on the surface. If the positive charge increases further, it will create a surface with a net positive charge and the bands will bend downward. In this case, the electrons can easily reach the surface to react with the solution.¹³⁷ The electrons and holes are separated by internal electric field to different surfaces. This internal electric field arises from the ferroelectric spontaneous polarization and the electrochemical potential of electrons at interfaces, especially surfaces (polar surface termination) and phase boundaries. As discussed before, the direction of spontaneous polarization varies in different domains. Figure 2-19 shows the effect of different internal electric fields on photochemical reactions.²

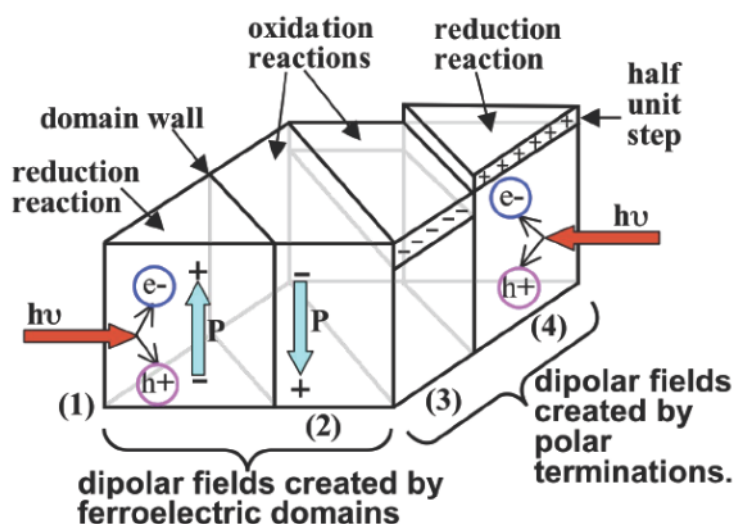


Figure 2-19 Schematic of the effect from internal electric field on the photocatalytic chemical reaction. (This figure is reproduced from reference 2.)

2.3.2 Previous Ferroelectric Research Review

Inoue et al.¹³⁸ demonstrated that positively poled ferroelectric $\text{Pb}(\text{Zr},\text{Ti})\text{O}_3$ produced 10-40 times more hydrogen during photolysis than negatively poled $\text{Pb}(\text{Zr},\text{Ti})\text{O}_3$. This observation provides evidence that ferroelectric polarization

influences reactivity. In addition, previous work in our group showed that dipolar fields promote spatially selective silver reduction and Pb oxidation on BaTiO₃ that is correlated to the domain structure.^{105,106} Similar experiments then verified that spatially localized photochemical reaction products also occur on the surface of BaTiO₃ and Sr₂Nb₂O₇ microcrystals,¹³⁹ extending the bulk photovoltaic effect to a smaller size scale. A similar spatially selective photochemical reaction is also observed on the polar surfaces of SrTiO₃ crystals, demonstrating that the internal dipolar fields arising from charged surface domains in nonferroelectric materials can also influence the transport of photogenerated charge carriers and promote the photochemical spatially selective reactions.¹⁸

The dipolar fields from a ferroelectric also influence the reactivity of supported films. If the ferroelectric field from the substrate cannot be screened by carriers in the interface and film, it will influence charge carriers on the surface of film.¹⁰⁷ It was reported that the photocatalytic activity of TiO₂ or NiO films supported by poled ferroelectric LiNbO₃ was enhanced for one type of domain polarization (positive or negative).¹⁴⁰ The work in our group showed that the photocatalytic reactivity of a TiO₂ film supported by BaTiO₃ is spatially selective and correlated to the domain polarization.¹⁰⁷ In addition to the effect from the substrate, the thickness of the film and the orientation relationship also influence photocatalytic activity.^{141,142} More recent results show that electrons generated in the narrow band gap ferroelectric BiFeO₃ substrate by visible light irradiation can be influenced by the dipolar fields and transported to the surface of TiO₂ films to participate in the redox marker

reactions.⁶² Currently, more and more attention is focused on the application of polarizable semiconductors to control photochemical reactions and this approach provides a new strategy for heterostructured photocatalyst design.⁹

2.3.3 Heterostructured Photocatalyst

Inspired by the advances in promoting photochemical reactions with dipolar fields discussed above, we proposed to design heterostructured particulate photocatalysts with efficient separation of photogenerated charge carriers and solar energy harvesting for water splitting. Core-shell nanocatalysts attract our attention because this structure can provide more freedom in the catalyst design, using different functionalities of the core and shell components to optimize solar light absorption, while maintaining high surface areas.^{46,143-151} Akin to the previous ferroelectrics coated with thin films,^{62,141,142} a heterostructured core-shell photocatalyst could take advantage of the favorable band edge locations of TiO₂ as a nanostructured shell of high surface areas and the absorption / charge separation properties of a core having internal fields to improve the activity of particulate photocatalysts for water splitting.

A ferroelectric core with an internal field is necessary in this heterostructured photocatalyst. As discussed before, the spontaneous polarization will diminish with the decrease of particle size in the nano range. In addition, nanostructured powders do not support internal space charges and,¹⁵² therefore, they do not separate the photogenerated electrons and holes, though certain composite geometries improve

carrier separation because of the relative positions of the energy levels for electrons and holes in each component.¹⁵³⁻¹⁵⁵ Considering the above reasons, a micron-sized core is used herein to create a heterostructured photocatalyst.

This heterostructured photocatalyst composed of a micron-sized core and nanostructured coating has been reported by literatures and is referred to the NBC (nano-bulk composite) structure.^{146,156-159} In the previous work, the micron-sized core was used to absorb visible light. To the best of our knowledge, the effect of using a ferroelectric core has not been reported. Gao et al.¹⁴⁶ demonstrated that nanostructured TiO₂ coatings on microcrystalline FeTiO₃ could be prepared and they reported improved properties for the degradation of organic dyes under visible light. Jang et al.¹⁵⁶ designed a p-n junction heterostructured photocatalyst consisting of a micron-sized AgGaS core with a TiO₂ coating to produce hydrogen from Na₂S/Na₂SO₃ solution.¹⁵⁶ They also utilized a TiO₂ coating to protect microcrystalline CdS from photocorrosion and used this heterostructured photocatalyst to produce hydrogen from visible light.^{157,158} Those reports demonstrate that this heterostructured photocatalyst design is promising for hydrogen production.

2.3.4 Photocatalyst Processing

As discussed above, the physical and chemical properties of a photocatalyst, such as crystallinity, structure, and surface orientation, depend on the processing. Understanding photocatalyst processing makes it possible to control the structure and

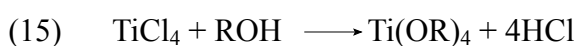
properties of heterostructured semiconductor powders. For example, nanomaterials with controlled morphologies such as nanotubes, nanosheets, and nanodiscs are produced in the hope that a certain shape or size will endow the materials with special and novel properties.^{34,160-163} Hierarchically structured macro/mesoporous titania is reported to increase the surface area and enhance light harvesting, simultaneously.¹⁶⁴ The next section describes two processing methods, namely sol-gel method and hydrothermal method, that we used in the experiments for core materials processing and TiO₂ coating.

2.3.5 Sol-gel Method

One of most common processing methods for semiconductors utilized in the scientific research is the sol-gel method. The sol-gel method refers to the hydrolysis and condensation of precursors, which are usually inorganic metal salts or metal organic compounds such as metal alkoxides.⁵³ In general, the method can be divided into three parts: hydrolysis, condensation, and annealing.

TiO₂ processing is discussed here to explain the basic mechanism and process of the sol-gel method. The preparation process starts from TiCl₄, which is then dissolved into the appropriate alcohol, represented as R-OH (R refers to alkyl group), to form the solution with the absence of water, as shown in equation (15). Water is then added into solution for hydrolysis under acid or base condition to substitute OR- with a hydroxyl (equation 16). The relatively high electronegativity of Ti weakens the O-H

bond such that condensation can occur between $\text{Ti}(\text{OR})_{4-n}(\text{OH})_n$ to form a 2-D or 3-D Ti-O network. The solution undergoes a dramatic increase of viscosity and, in some cases, changes color. The gel then contracts and expels solvent from its pores to form a solid mass. This process is called aging. Continued solvent removal using conventional thermal heating leads to the formation of a xerogel. If supercritical drying is used, an aerogel is formed. The gel is stabilized by calcining at high temperature, which removes surface-bond R-OH. At a sufficiently high temperature, the pores collapse and a dense ceramic is formed.^{165,166}



The other configurations for sol-gel includes the Pechini Method,¹⁶⁷ the Citrate Gel Method,¹⁶⁸ and the Glycine Nitrate Process.¹⁶⁹ The fundamental mechanism of these processing methods is analogous to the traditional sol-gel method but employs different gel formation processes. Several factors have an influence on the final particle size and morphology. For instance, the pH of the precursor can be adjusted to control the size of particles.¹⁷⁰ In addition, adding a structure directing reagent is one way to prepare high surface area semiconductors, such as mesoporous materials.¹⁷¹ Another significant parameter to control the particle size is annealing temperature, which determines the growth rate.¹⁷²

The sol-gel method is advantageous compared to other processing methods. Compared with the methods to produce similar ceramics, the calcining temperature is

lower, particularly for polymeric gels, which is the characteristic feature of sol-gel method.¹⁶⁶ Moreover, the size and morphology can be easily controlled by adjusting the formation of the gel and annealing temperature. During the sol-gel process, reactants can be mixed at a molecular level and are thus apt to produce spherical and chemically uniform powders. Doping elements can be added quantitatively into the mixture. The ability of the sol-gel method to coat large and complex surfaces is also outstanding, even compared with other methods, which is a primary reason to utilize this technique for fabricating core-shell heterostructured powders.¹⁷³⁻¹⁷⁵ The disadvantage of the sol-gel method is that large shrinkage of the gel during calcination makes dimensional control of large articles difficult, and as a result it is usually used to produce films, fibers, and powders.¹⁶⁶ In addition, the formation of secondary phases at high temperature and the formation of agglomerates are also disadvantages of the sol-gel method for specific applications.

2.3.6 Hydrothermal Method

Hydrothermal processing can be defined as any heterogeneous reaction in the presence of aqueous solvents or mineralizers under high pressure and temperature conditions to dissolve and recrystallize materials that are relatively insoluble under ordinary conditions.¹⁷⁶ A mineralizer refers to a substance or solvent that promotes crystallization.¹⁷⁶ Processes involving other solvents as the reaction medium are more commonly called as solvothermal processes. Examples of solvothermal processes are

glycothermal, alcohothermal, ammonothermal, carbonothermal, lyothermal, depending on what solvent is utilized in the chemical reaction. The mechanism of those methods is basically the same.

Hydrothermal processing takes advantage of some special properties of supercritical fluids. If the temperature and pressure is above some critical value, the liquid will transform to a supercritical fluid, which exhibits properties of both liquid and gas. The most characteristic property of a supercritical fluid is to dissolve chemical compounds that are hard to dissolve under ambient conditions.¹⁷⁷ Although hydrothermal processing does not generally reach supercritical temperatures and pressures, it takes advantage of the increase in solubility and reactivity for solutes at elevated temperature and pressure.¹⁶⁵ The traditional processing temperature is relatively low (100-300 °C) compared with other methods such as sol-gel and combustion.

The whole hydrothermal process is divided into dissolution, diffusion, nucleation, and growth. The primary variable parameters for processing are temperature, pressure, pH of solution, reaction time, mineralizer types, and concentration.¹⁷⁸⁻¹⁸³ Those parameters can be utilized to control the size and morphology of the final product because of their influence on the nucleation and growth process. Currently, the hydrothermal process is employed for the growth of single crystals,¹⁸⁴ fine particles,¹⁸⁵ nanomaterials,¹⁸⁶ and composites.¹⁸⁷

One characteristic advantage of the hydrothermal method is that the product can be synthesized at low temperature. This saves energy and avoids the formation of hard

agglomerates.¹⁸³ The sol-gel method is sometimes coupled with the hydrothermal method to prepare high surface area mesoporous nanoparticles. The high annealing temperature for crystallization in the sol-gel method makes the pore structure in the nanoparticles collapse, leading to the formation of dense ceramics. The relatively low temperature for crystallization of amorphous phases by the hydrothermal method can prevent the collapse of pores and protect the mesoporous structure.¹⁸⁸ In addition, the hydrothermal method can achieve high chemical homogeneity at a molecular scale.¹⁸⁹

2.4 References

- (1) Rabe, K. M.; Ahn, C. H.; Triscone, J. M. *Physics of Ferroelectrics: A Modern Perspective*; Springer, 2007.
- (2) Bhardwaj, A. The Composition Dependence of the Photochemical Reactivity of Barium Strontium Titanates, Carnegie Mellon University, 2008.
- (3) M.E.Lines; A.M.Glass *Principles and applications of ferroelectrics and related materials*; Oxford:Clarendon Press 1977.
- (4) Damjanovic, D. *Reports on Progress in Physics* **1998**, *61*, 1267.
- (5) Ahn, C. H.; Rabe, K. M.; Triscone, J. M. *Science* **2004**, *303*, 488.
- (6) M.E.Lines; A.M.Glass *Principles and Applications of Ferroelectrics and Related Materials*. ; Clarendon Press, Oxford 2001.
- (7) Braithwaite, N.; Weaver, G. *Materials in action series - Electronic Materials inside electronic devices*; Alden Press (London & Northampton) Ltd: London 1998.
- (8) Mitsui, T.; Tatsuzaki, I.; Nakamura, E. *An Introduction to the Physics of Ferroelectrics*; Gordon and Breach Science Publishers, 1976.
- (9) Tiwari, D.; Dunn, S. *Journal of Materials Science* **2009**, *44*, 5063.
- (10) Akdogan, E. K.; Rawn, C. J.; Porter, W. D.; Payzant, E. A.; Safari, A. *Journal of Applied Physics* **2005**, *97*, 084305.
- (11) Yashima, M.; Hoshina, T.; Ishimura, D.; Kobayashi, S.; Nakamura, W.; Tsurumi, T.; Wada, S. *Journal of Applied Physics* **2005**, *98*, 014313.
- (12) Uchino, K.; Sadanaga, E.; Hirose, T. *Journal of the American Ceramic Society* **1989**, *72*, 1555.
- (13) Li, X. P.; Shih, W. H. *Journal of the American Ceramic Society* **1997**, *80*, 2844.
- (14) Alexe, M.; Harnagea, C.; Hesse, D.; Gosele, U. *Applied Physics Letters* **2001**, *79*, 242.
- (15) Tsunekawa, S.; Ito, S.; Mori, T.; Ishikawa, K.; Li, Z. Q.; Kawazoe, Y. *Physical Review B* **2000**, *62*, 3065.

- (16) Zhang, L.; Zhong, W. L.; Wang, C. L.; Peng, Y. P.; Wang, Y. G. *European Physical Journal B* **1999**, *11*, 565.
- (17) Morrison, S. R. *Electrochemistry at semiconductor and oxidized metal electrodes*; Plenum Press: New York, 1980.
- (18) Giocondi, J. L.; Rohrer, G. S. *Journal of the American Ceramic Society* **2003**, *86*, 1182.
- (19) Schultz, A. M.; Salvador, P. A.; Rohrer, G. S. *Chemical Communications* **2012**, *48*, 2012.
- (20) Schultz, A. The Growth and Photochemical Activity of Hematite Films on Perovskite Substrates, Carnegie Mellon University 2012.
- (21) Fujishima, A.; Honda, K. *Nature* **1972**, *238*, 37.
- (22) Hashimoto, K.; Irie, H.; Fujishima, A. *Japanese Journal of Applied Physics Part 1-Regular Papers Brief Communications & Review Papers* **2005**, *44*, 8269.
- (23) Kitano, M.; Hara, M. *Journal of Materials Chemistry* **2010**, *20*, 627.
- (24) N.Serpone; Pelizzetti, E. *Photocatalysis*; Wiley: New York, 1989.
- (25) Rajeshwar, K. *Journal of Applied Electrochemistry* **2007**, *37*, 765.
- (26) Rufino M. Navarro Yerga, M. C. A. G., F. del Valle, Jose A. Villoria de la Mano, and Jose L. G. Fierro. *ChemSusChem* **2009**, *2*, 471.
- (27) Kudo, A.; Miseki, Y. *Chemical Society Reviews* **2009**, *38*, 253.
- (28) Zhang, Z.; Wang, C. C.; Zakaria, R.; Ying, J. Y. *The Journal of Physical Chemistry B* **1998**, *102*, 10871.
- (29) Beydoun, D.; Amal, R.; Low, G.; McEvoy, S. *Journal of Nanoparticle Research* **1999**, *1*, 439.
- (30) Bhardwaj, A.; Burbure, N. V.; Gamalski, A.; Rohrer, G. S. *Chemistry of Materials* **2010**, *22*, 3527.
- (31) Albery, W. J.; Bartlett, P. N. *Journal of the Electrochemical Society* **1984**, *131*, 315.
- (32) Masao, K.; Ichiro, O. *Photocatalysis Science and Technology*; Springer, 2002.
- (33) Banin, U.; Cao, Y. W.; Katz, D.; Millo, O. *Nature* **1999**, *400*, 542.
- (34) Peng, X. G.; Manna, L.; Yang, W. D.; Wickham, J.; Scher, E.; Kadavanich, A.; Alivisatos, A. P. *Nature* **2000**, *404*, 59.
- (35) Wang, Y.; Herron, N. *The Journal of Physical Chemistry* **1991**, *95*, 525.
- (36) Zhang, H. Z.; Banfield, J. F. *The Journal of Physical Chemistry B* **2000**, *104*, 3481.
- (37) Hernandez-Alonso, M. D.; Fresno, F.; Suarez, S.; Coronado, J. M. *Energy & Environmental Science* **2009**, *2*, 1231.
- (38) Sclafani, A.; Herrmann, J. M. *The Journal of Physical Chemistry* **1996**, *100*, 13655.
- (39) Kavan, L.; Grätzel, M.; Gilbert, S. E.; Klemenz, C.; Scheel, H. J. *Journal of the American Chemical Society* **1996**, *118*, 6716.
- (40) Park, N. G.; van de Lagemaat, J.; Frank, A. J. *The Journal of Physical Chemistry B* **2000**, *104*, 8989.
- (41) Hurum, D. C.; Agrios, A. G.; Gray, K. A.; Rajh, T.; Thurnauer, M. C. *The Journal of Physical Chemistry B* **2003**, *107*, 4545.
- (42) Chan, C. K.; Porter, J. F.; Li, Y. G.; Guo, W.; Chan, C. M. *Journal of the American Ceramic Society* **1999**, *82*, 566.
- (43) Zhang, Q. H.; Gao, L.; Guo, J. K. *Applied Catalysis B-Environmental* **2000**, *26*, 207.
- (44) Gao, L.; Zhang, Q. H. *Scripta Materialia* **2001**, *44*, 1195.

- (45) Maeda, K.; Domen, K. *Journal of Physical Chemistry Letters* **2010**, *1*, 2655.
- (46) Maeda, K.; Teramura, K.; Lu, D.; Saito, N.; Inoue, Y.; Domen, K. *Angewandte Chemie International Edition* **2006**, *45*, 7806.
- (47) Maeda, K.; Teramura, K.; Lu, D. L.; Takata, T.; Saito, N.; Inoue, Y.; Domen, K. *The Journal of Physical Chemistry B* **2006**, *110*, 13753.
- (48) Maeda, K.; Teramura, K.; Lu, D. L.; Takata, T.; Saito, N.; Inoue, Y.; Domen, K. *Nature* **2006**, *440*, 295.
- (49) Maeda, K.; Teramura, K.; Lu, D. L.; Saito, N.; Inoue, Y.; Domen, K. *The Journal of Physical Chemistry C* **2007**, *111*, 7554.
- (50) Maeda, K.; Takata, T.; Hara, M.; Saito, N.; Inoue, Y.; Kobayashi, H.; Domen, K. *Journal of the American Chemical Society* **2005**, *127*, 8286.
- (51) Reber, J. F.; Rusek, M. *The Journal of Physical Chemistry* **1986**, *90*, 824.
- (52) Buhler, N.; Meier, K.; Reber, J. F. *The Journal of Physical Chemistry* **1984**, *88*, 3261.
- (53) Chen, X.; Mao, S. S. *Chemical Reviews* **2007**, *107*, 2891.
- (54) Serpone, N.; Lawless, D.; Disdier, J.; Herrmann, J. M. *Langmuir* **1994**, *10*, 643.
- (55) Zhu, J. F.; Deng, Z. G.; Chen, F.; Zhang, J. L.; Chen, H. J.; Anpo, M.; Huang, J. Z.; Zhang, L. Z. *Applied Catalysis B-Environmental* **2006**, *62*, 329.
- (56) Choi, W.; Termin, A.; Hoffmann, M. R. *The Journal of Physical Chemistry* **1994**, *98*, 13669.
- (57) Devi, L. G.; Murthy, B. N. *Catalysis Letters* **2008**, *125*, 320.
- (58) Asahi, R.; Morikawa, T.; Ohwaki, T.; Aoki, K.; Taga, Y. *Science* **2001**, *293*, 269.
- (59) Ohno, T.; Akiyoshi, M.; Umebayashi, T.; Asai, K.; Mitsui, T.; Matsumura, M. *Applied Catalysis A-General* **2004**, *265*, 115.
- (60) Ren, W. J.; Ai, Z. H.; Jia, F. L.; Zhang, L. Z.; Fan, X. X.; Zou, Z. G. *Applied Catalysis B-Environmental* **2007**, *69*, 138.
- (61) Li, D.; Haneda, H.; Labhsetwar, N. K.; Hishita, S.; Ohashi, N. *Chemical Physics Letters* **2005**, *401*, 579.
- (62) Zhang, Y.; Schultz, A. M.; Salvador, P. A.; Rohrer, G. S. *Journal of Materials Chemistry* **2011**, *21*, 4168.
- (63) Wang, X. H.; Li, J. G.; Kamiyama, H.; Moriyoshi, Y.; Ishigaki, T. *The Journal of Physical Chemistry B* **2006**, *110*, 6804.
- (64) Oregan, B.; Gratzel, M. *Nature* **1991**, *353*, 737.
- (65) Gratzel, M. *Chemistry Letters* **2005**, *34*, 8.
- (66) Maeda, K.; Eguchi, M.; Youngblood, W. J.; Mallouk, T. E. *Chemistry of Materials* **2008**, *20*, 6770.
- (67) Gratzel, M. *Nature* **2001**, *414*, 338.
- (68) Byrd, H.; Clearfield, A.; Poojary, D.; Reis, K. P.; Thompson, M. E. *Chemistry of Materials* **1996**, *8*, 2239.
- (69) Sayama, K.; Mukasa, K.; Abe, R.; Abe, Y.; Arakawa, H. *Journal of Photochemistry and Photobiology A: Chemistry* **2002**, *148*, 71.
- (70) Wu, Q.; Li, D.; Wu, L.; Wang, J.; Fu, X.; Wang, X. *Journal of Materials Chemistry* **2006**, *16*, 1116.
- (71) Huang, H.; Li, D.; Lin, Q.; Zhang, W.; Shao, Y.; Chen, Y.; Sun, M.; Fu, X. *Environmental Science & Technology* **2009**, *43*, 4164.

- (72) Huang, H.; Li, D.; Lin, Q.; Shao, Y.; Chen, W.; Hu, Y.; Chen, Y.; Fu, X. *The Journal of Physical Chemistry C* **2009**, *113*, 14264.
- (73) Kim, Y. J.; Gao, B.; Han, S. Y.; Jung, M. H.; Chakraborty, A. K.; Ko, T.; Lee, C.; Lee, W. I. *The Journal of Physical Chemistry C* **2009**, *113*, 19179.
- (74) Chen, X.; Shen, S.; Guo, L.; Mao, S. S. *Chemical Reviews* **2010**, *110*, 6503.
- (75) Zhang, X.; Zhang, L.; Xie, T.; Wang, D. *The Journal of Physical Chemistry C* **2009**, *113*, 7371.
- (76) Kawai, T.; Sakata, T. *Nature* **1980**, *286*, 474.
- (77) Sakata, T.; Kawai, T. *Chemical Physics Letters* **1981**, *80*, 341.
- (78) Bamwenda, G. R.; Tsubota, S.; Nakamura, T.; Haruta, M. *Journal of Photochemistry and Photobiology A-Chemistry* **1995**, *89*, 177.
- (79) Ozawa, H.; Haga, M. A.; Sakai, K. *Journal of the American Chemical Society* **2006**, *128*, 4926.
- (80) Lee, S. G.; Lee, S.; Lee, H. I. *Applied Catalysis a-General* **2001**, *207*, 173.
- (81) Zong, X.; Yan, H. J.; Wu, G. P.; Ma, G. J.; Wen, F. Y.; Wang, L.; Li, C. *Journal of the American Chemical Society* **2008**, *130*, 7176.
- (82) Nada, A. A.; Barakat, M. H.; Hamed, H. A.; Mohamed, N. R.; Veziroglu, T. N. *International Journal of Hydrogen Energy* **2005**, *30*, 687.
- (83) Ni, M.; Leung, M. K. H.; Leung, D. Y. C.; Sumathy, K. *Renewable & Sustainable Energy Reviews* **2007**, *11*, 401.
- (84) Galinska, A.; Walendziewski, J. *Energy & Fuels* **2005**, *19*, 1143.
- (85) Li, Y.; Lu, G.; Li, S. *Chemosphere* **2003**, *52*, 843.
- (86) Kozlova, E. A.; Korobkina, T. P.; Vorontsov, A. V. *International Journal of Hydrogen Energy* **2009**, *34*, 138.
- (87) Kozlova, E. A.; Korobkina, T. P.; Vorontsov, A. V.; Parmon, V. N. *Applied Catalysis A: General* **2009**, *367*, 130.
- (88) Bamwenda, G. R.; Arakawa, H. *Solar Energy Materials and Solar Cells* **2001**, *70*, 1.
- (89) Higashi, M.; Abe, R.; Takata, T.; Domen, K. *Chemistry of Materials* **2009**, *21*, 1543.
- (90) Abe, R.; Sayama, K.; Domen, K.; Arakawa, H. *Chemical Physics Letters* **2001**, *344*, 339.
- (91) Abe, R.; Sayama, K.; Sugihara, H. *The Journal of Physical Chemistry B* **2005**, *109*, 16052.
- (92) Bamwenda, G. R.; Sayama, K.; Arakawa, H. *Journal of Photochemistry and Photobiology A-Chemistry* **1999**, *122*, 175.
- (93) Sasaki, Y.; Iwase, A.; Kato, H.; Kudo, A. *Journal of Catalysis* **2008**, *259*, 133.
- (94) Fujihara, K.; Ohno, T.; Matsumura, M. *Journal of the Chemical Society, Faraday Transactions* **1998**, *94*, 3705.
- (95) Arakawa, H.; Sayama, K. *Catalysis Surveys from Japan* **2000**, *4*, 75.
- (96) Sayama, K.; Arakawa, H. *The Journal of Physical Chemistry* **1993**, *97*, 531.
- (97) Sayama, K.; Arakawa, H. *Journal of Photochemistry and Photobiology A-Chemistry* **1996**, *94*, 67.
- (98) Kudo, A.; Ueda, K.; Kato, H.; Mikami, I. *Catalysis Letters* **1998**, *53*, 229.
- (99) Kudo, A.; Omori, K.; Kato, H. *Journal of the American Chemical Society* **1999**, *121*, 11459.

- (100) Ohmori, T.; Takahashi, H.; Mametsuka, H.; Suzuki, E. *Physical Chemistry Chemical Physics* **2000**, *2*, 3519.
- (101) Singh, A. P.; Kumari, S.; Tripathi, A.; Singh, F.; Gaskell, K. J.; Shrivastav, R.; Dass, S.; Ehrman, S. H.; Satsangi, V. R. *The Journal of Physical Chemistry C* **2010**, *114*, 622.
- (102) Diamant, Y.; Chen, S. G.; Melamed, O.; Zaban, A. *The Journal of Physical Chemistry B* **2003**, *107*, 1977.
- (103) Chen, C.; Ma, W.; Zhao, J. *Chemical Society Reviews* **2010**, *39*, 4206.
- (104) Han, F.; Kambala, V. S. R.; Srinivasan, M.; Rajarathnam, D.; Naidu, R. *Appl. Catal. A-Gen* **2009**, *359*, 25.
- (105) Giocondi, J. L.; Rohrer, G. S. *The Journal of Physical Chemistry B* **2001**, *105*, 8275.
- (106) Giocondi, J. L.; Rohrer, G. S. *Chemistry of Materials* **2001**, *13*, 241.
- (107) Burbure, N. V.; Salvador, P. A.; Rohrer, G. S. *Journal of the American Ceramic Society* **2006**, *89*, 2943.
- (108) Hoffmann, M. R.; Martin, S. T.; Choi, W.; Bahnemann, D. W. *Chemical Reviews* **1995**, *95*, 69.
- (109) Matsunaga, T.; Tomoda, R.; Nakajima, T.; Nakamura, N.; Komine, T. *Applied and Environmental Microbiology* **1988**, *54*, 1330.
- (110) Baly, E. C. C.; Heilbron, I. M.; Barker, W. F. *Journal of the Chemical Society* **1921**, *119*, 1025.
- (111) Fujishima, A.; Rao, T. N.; Tryk, D. A. *Journal of Photochemistry and Photobiology C: Photochemistry Reviews* **2000**, *1*, 1.
- (112) Shapovalov, V. I. *Glass Physics and Chemistry*, *36*, 121.
- (113) Tachikawa, T.; Fujitsuka, M.; Majima, T. *The Journal of Physical Chemistry C* **2007**, *111*, 5259.
- (114) Zhu, J.; Zach, M. *Current Opinion in Colloid & Interface Science* **2009**, *14*, 260.
- (115) Nowotny, M. K.; Bak, T.; Nowotny, J. *The Journal of Physical Chemistry B* **2006**, *110*, 16270.
- (116) Nowotny, M. K.; Bak, T.; Nowotny, J.; Sorrell, C. C. *Physica status solidi (b)* **2005**, *242*, R88.
- (117) Nowotny, M. K.; Bogdanoff, P.; Dittrich, T.; Fiechter, S.; Fujishima, A.; Tributsch, H. *Materials Letters* **2010**, *64*, 928.
- (118) Kamat, P. V. *The Journal of Physical Chemistry C* **2007**, *111*, 2834.
- (119) Bao, N.; Shen, L.; Takata, T.; Lu, D.; Domen, K. *Chemistry Letters* **2006**, *35*, 318.
- (120) Jitputti, J.; Suzuki, Y.; Yoshikawa, S. *Catalysis Communications* **2008**, *9*, 1265.
- (121) Jia, H.; Xiao, W. J.; Zhang, L.; Zheng, Z.; Zhang, H.; Deng, F. *The Journal of Physical Chemistry C* **2008**, *112*, 11379.
- (122) Song, X.; Gao, L. *The Journal of Physical Chemistry C* **2008**, *112*, 15299.
- (123) Lu, F.; Cai, W.; Zhang, Y. *Advanced Functional Materials* **2008**, *18*, 1047.
- (124) Liu, G.; Yu, J. C.; Lu, G. Q.; Cheng, H. M. *Chemical Communications* **2011**, 47.
- (125) Pan, J.; Liu, G.; Lu, G. Q.; Cheng, H. M. *Angewandte Chemie International Edition* **2011**, *50*, 2133.
- (126) Zhang, H.; Han, Y.; Liu, X.; Liu, P.; Yu, H.; Zhang, S.; Yao, X.; Zhao, H. *Chemical Communications* **2010**, *46*, 8395.

- (127) Yang, H. G.; Sun, C. H.; Qiao, S. Z.; Zou, J.; Liu, G.; Smith, S. C.; Cheng, H. M.; Lu, G. Q. *Nature* **2008**, *453*, 638.
- (128) Yang, H. G.; Liu, G.; Qiao, S. Z.; Sun, C. H.; Jin, Y. G.; Smith, S. C.; Zou, J.; Cheng, H. M.; Lu, G. Q. *Journal of the American Chemical Society* **2009**, *131*, 4078.
- (129) Ye, L.; Tian, L.; Peng, T.; Zan, L. *Journal of Materials Chemistry* **2011**, *21*, 12479.
- (130) Liu, G.; Sun, C.; Yang, H. G.; Smith, S. C.; Wang, L.; Lu, G. Q. M.; Cheng, H. M. *Chem Commun* **2010**, *46*, 755.
- (131) Guan, G.; Kida, T.; Kusakabe, K.; Kimura, K.; Fang, X.; Ma, T.; Abe, E.; Yoshida, A. *Chemical Physics Letters* **2004**, *385*, 319.
- (132) Shen, S.; Guo, L. *Journal of Solid State Chemistry* **2006**, *179*, 2629.
- (133) Jing, D.; Guo, L. *Catalysis Communications* **2007**, *8*, 795.
- (134) Nozik, A. J. *Applied Physics Letters* **1977**, *30*, 567.
- (135) Glass, A. M.; von der Linde, D.; Negran, T. J. *Applied Physics Letters* **1974**, *25*, 233.
- (136) Ambacher, O.; Smart, J.; Shealy, J. R.; Weimann, N. G.; Chu, K.; Murphy, M.; Schaff, W. J.; Eastman, L. F.; Dimitrov, R.; Wittmer, L.; Stutzmann, M.; Rieger, W.; Hilsenbeck, J. *Journal of Applied Physics* **1999**, *85*, 3222.
- (137) Bard, A. J.; Faulkner, L. R. *Electrochemical methods : fundamentals and applications* 2nd ed.; John Wiley & Sons, Inc.: New York, 2001.
- (138) Inoue, Y.; Sato, K.; Sato, K.; Miyama, H. *The Journal of Physical Chemistry* **1986**, *90*, 2809.
- (139) Giocondi, J. L.; Rohrer, G. S. *Topics in Catalysis* **2008**, *49*, 18.
- (140) Inoue, Y.; Okamura, M.; Sato, K. *The Journal of Physical Chemistry* **1985**, *89*, 5184.
- (141) Burbure, N. V.; Salvador, P. A.; Rohrer, G. S. *Chemistry of Materials* **2010**, *22*, 5823.
- (142) Burbure, N. V.; Salvador, P. A.; Rohrer, G. S. *Chemistry of Materials* **2010**, *22*, 5831.
- (143) Elder, S. H.; Cot, F. M.; Su, Y.; Heald, S. M.; Tyryshkin, A. M.; Bowman, M. K.; Gao, Y.; Joly, A. G.; Balmer, M. L.; Kolwaite, A. C.; Magrini, K. A.; Blake, D. M. *Journal of the American Chemical Society* **2000**, *122*, 5138.
- (144) Hirakawa, T.; Kamat, P. V. *Journal of the American Chemical Society* **2005**, *127*, 3928.
- (145) Luo, J. H.; Maggard, P. A. *Advanced Materials* **2006**, *18*, 514.
- (146) Gao, B.; Kim, Y. J.; Chakraborty, A. K.; Lee, W. I. *Appl. Catal. B-Environ.* **2008**, *83*, 202.
- (147) Joo, S. H.; Park, J. Y.; Tsung, C.-K.; Yamada, Y.; Yang, P.; Somorjai, G. A. *Nature Materials* **2009**, *8*, 126.
- (148) Ye, M.; Zhang, Q.; Hu, Y.; Ge, J.; Lu, Z.; He, L.; Chen, Z.; Yin, Y. *Chemistry – A European Journal* **2010**, *16*, 6243.
- (149) Diamant, Y.; Chappel, S.; Chen, S. G.; Melamed, O.; Zaban, A. *Coordination Chemistry Reviews* **2004**, *248*, 1271.
- (150) Li, S.; Steigerwald, M. L.; Brus, L. E. *ACS Nano* **2009**, *3*, 1267.
- (151) Li, S.; Lin, Y. H.; Zhang, B. P.; Li, J. F.; Nan, C. W. *Journal of Applied Physics*

- 2009**, 105.
- (152) Albery, W. J.; Philip, N. B. *Journal of The Electrochemical Society* **1984**, 131, 315.
- (153) Vogel, R.; Pohl, K.; Weller, H. *Chemical Physics Letters* **1990**, 174, 241.
- (154) Hotchandani, S.; Kamat, P. V. *The Journal of Physical Chemistry* **1992**, 96, 6834.
- (155) Zaban, A.; Micic, O. I.; Gregg, B. A.; Nozik, A. J. *Langmuir* **1998**, 14, 3153.
- (156) Jang, J. S.; Hong, S. J.; Kim, J. Y.; Lee, J. S. *Chemical Physics Letters* **2009**, 475, 78.
- (157) Jang, J. S.; Li, W.; Oh, S. H.; Lee, J. S. *Chemical Physics Letters* **2006**, 425, 278.
- (158) Jang, J. S.; Ji, S. M.; Bae, S. W.; Son, H. C.; Lee, J. S. *Journal of Photochemistry and Photobiology A: Chemistry* **2007**, 188, 112.
- (159) Jang, J. S.; Choi, S. H.; Kim, H. G.; Lee, J. S. *The Journal of Physical Chemistry C* **2008**, 112, 17200.
- (160) Ma, W. L.; Yang, C. Y.; Gong, X.; Lee, K.; Heeger, A. J. *Advanced Functional Materials* **2005**, 15, 1617.
- (161) Vayssieres, L. *Advanced Materials* **2003**, 15, 464.
- (162) Testino, A.; Bellobono, I. R.; Buscaglia, V.; Canevali, C.; D'Arienzo, M.; Polizzi, S.; Scotti, R.; Morazzoni, F. *Journal of the American Chemical Society* **2007**, 129, 3564.
- (163) Zhang, F. X.; Guan, N. J.; Li, Y. Z.; Zhang, X.; Chen, J. X.; Zeng, H. S. *Langmuir* **2003**, 19, 8230.
- (164) Wang, X. C.; Yu, J. C.; Ho, C. M.; Hou, Y. D.; Fu, X. Z. *Langmuir* **2005**, 21, 2552.
- (165) Cushing, B. L.; Kolesnichenko, V. L.; O'Connor, C. J. *Chemical Reviews* **2004**, 104, 3893.
- (166) Rahaman, M. N. *Ceramic Processing and Sintering (second edition)*, 2003.
- (167) Pechini, M. Method of Preparing Lead and Alkaline Earth Titanates and Niobates and Coating Method Using the Same to Form a Capacitor. In *United States Patent*; Office, U. S. P., Ed. US, 1967.
- (168) Marcilly, C.; Courty, P.; Delmon, B. *Journal of the American Ceramic Society* **1970**, 53, 56.
- (169) Chick, L. A.; Pederson, L. R.; Maupin, G. D.; Bates, J. L.; Thomas, L. E.; Exarhos, G. J. *Materials Letters* **1990**, 10, 6.
- (170) Tokumoto, M. S.; Pulcinelli, S. H.; Santilli, C. V.; Briois, V. *The Journal of Physical Chemistry B* **2003**, 107, 568.
- (171) Kobayashi, S.; Hamasaki, N.; Suzuki, M.; Kimura, M.; Shirai, H.; Hanabusa, K. *Journal of the American Chemical Society* **2002**, 124, 6550.
- (172) Zhang, Q. Y.; Pita, K.; Ye, W.; Que, W. X. *Chemical Physics Letters* **2002**, 351, 163.
- (173) Jiang, L.; Wang, L.; Zhang, J. *Chemical Communications* **2010**, 46, 8067.
- (174) Nakamura, K. J.; Ide, Y.; Ogawa, M. *Materials Letters* **2011**, 65, 24.
- (175) Yu, M.; Lin, J.; Fang, J. *Chemistry of Materials* **2005**, 17, 1783.
- (176) Byrappa, K.; Adschiri, T. *Progress in Crystal Growth and Characterization of Materials* **2007**, 53, 117.
- (177) Comstock, M. J. *Supercritical Fluid Science and Technology*; American Chemical Society, 1989.
- (178) Chad, R. P.; Elliott, B. S. *Journal of the American Ceramic Society* **1999**, 82, 1702.

- (179) Somiya, S.; Roy, R. *Bulletin of Materials Science* **2000**, *23*, 453.
- (180) Sridhar, K.; Menon, V. C.; Li, Q. H.; Rustum, R.; Ainger, F. *Journal of the American Ceramic Society* **1996**, *79*, 1409.
- (181) Cheng, H.; Ma, J.; Zhao, Z.; Qi, L. *Chemistry of Materials* **1995**, *7*, 663.
- (182) Yang, G. B.; Li, Y. X.; Yin, Q. R.; Wang, P. L.; Cheng, Y. B. *Materials Letters* **2002**, *55*, 46.
- (183) Chen, C.; Cheng, J.; Yu, S.; Che, L.; Meng, Z. *Journal of Crystal Growth* **2006**, *291*, 135.
- (184) Dem'yanets, L.; Li, L.; Uvarova, T. *Journal of Materials Science* **2006**, *41*, 1439.
- (185) Lencka, M. M.; Anderko, A.; Riman, R. E. *Journal of the American Ceramic Society* **1995**, *78*, 2609.
- (186) Zhan, B. Z.; White, M. A.; Sham, T. K.; Pincock, J. A.; Doucet, R. J.; Rao, K. V. R.; Robertson, K. N.; Cameron, T. S. *Journal of the American Chemical Society* **2003**, *125*, 2195.
- (187) Byrappa, K.; Dayananda, A.; Sajan, C.; Basavalingu, B.; Shayan, M.; Soga, K.; Yoshimura, M. *Journal of Materials Science* **2008**, *43*, 2348.
- (188) Carp, O.; Huisman, C. L.; Reller, A. *Progress in Solid State Chemistry* **2004**, *32*, 33.
- (189) Yoshimura, M.; Byrappa, K. *Journal of Materials Science* **2008**, *43*, 2085.

3. Materials and Experimental Methods

This chapter introduces fundamental information about the materials utilized in this dissertation, including their structures, synthesis methods, physical properties, and chemical properties. In addition, it explains the experimental apparatus and the characterization techniques that were employed.

3.1 Materials

The micron-sized core materials were fabricated from commercially available powders. Those powders that were not available commercially were synthesized in-house. Before describing the experimental methods, the important materials properties are described so that the reader can better understand our experimental setup and the reasoning behind the choice of materials.

3.1.1 BaTiO₃

As discussed in Chapter 2, BaTiO₃ was the first perovskite oxide compound identified as a ferroelectric.¹ The Curie temperature for BaTiO₃ crystal is 120 °C.¹ Above the Curie temperature, BaTiO₃ has a paraelectric cubic structure (space group: $Pm\bar{3}m$) with the lattice parameter $a=4.0 \text{ \AA}$.² When the temperature is less than the Curie temperature, BaTiO₃ crystal transforms to a ferroelectric tetragonal phase ($P4mm$). The [001] direction or the c-axis is the dipole direction in each domain.³

The structure schematic and the origin of ferroelectricity are shown in figure 2-1.

The band gap energy of BaTiO₃ is reported to be in the range of 3.0 eV to 3.2 eV.^{4,5} The measured spontaneous polarization for the different ferroelectric phases of BaTiO₃ are 33 μC/cm² (rhombohedral), 36 μC/cm² (orthorhombic) and 27 μC/cm² (tetragonal), respectively.⁶ Domains are separated by either 90 ° or 180 ° domain walls in the tetragonal room temperature phase, depending on the change in the polarization direction.⁷ At the room temperature, BaTiO₃ is usually oxygen-deficient and, therefore, an n-type conductor.⁸

The most common way to synthesize BaTiO₃ powders is solid state reaction: barium carbonate and titanium dioxide are mixed and then calcined at high temperature.⁹ Other methods, such as sol-gel and hydrothermal methods, are also used to obtain powders with different sizes and morphologies.^{10,11}

3.1.2 SrTiO₃

SrTiO₃ also belongs to the perovskite family and its structure at room temperature is cubic with a lattice parameter $a = 3.905 \text{ \AA}$.¹² The band gap energy of SrTiO₃ is reported to be 3.2 eV to 3.6 eV.^{4,13} Analogous to BaTiO₃, SrTiO₃ also exhibits n-type conductivity at room temperature and standard atmosphere.¹⁴

SrTiO₃ is a paraelectric, n-type semiconductor at room temperature. At 120 K, the structure transforms to a tetragonal phase through an antiferrodistortive transition.¹⁵ However, the surface of SrTiO₃ is reported to exhibit ferroelectric-like

properties due to the surface layer termination.¹⁶⁻¹⁸ Dipolar fields can arise from charged domains on polar surfaces.¹⁸ The bulk paraelectric phase also can be converted into a ferroelectric by epitaxial strain at room temperature.¹⁹

3.1.3 PbTiO₃

Another representative perovskite compound, PbTiO₃, undergoes a paraelectric-ferroelectric transition at 487 °C.²⁰ The ferroelectric phase has a tetragonal structure (*P4mm*) with a polarization of about 75 μC/cm² measured at room temperature. The theoretically calculated polarization is 88 μC/cm².^{1,21} The spontaneous polarization in PbTiO₃ is parallel to the c-axis of the tetragonal unit cell and the crystal distortion and results from the displacement of Ti and O atoms relative to Pb (analogous to BaTiO₃).²² The experimental lattice constant for cubic phase is 3.865 Å.²³ The tetragonal phase has lattice parameters of a = 3.942 Å and c = 4.011 Å.²⁴ As for tetragonal BaTiO₃, the ferroelectric domains are separated by 90° and 180° domain walls. At ambient temperature, PbTiO₃ crystal exhibits n-type electronic conductivity.^{25,26} The band gap energy for PbTiO₃ is reported to be 3.0 eV to 3.4 eV.^{27,28} Some literature reports indicate a more narrow band gap energy for PbTO₃, ≈ 2.8 eV, and report photocatalytic activity under visible light.²⁹ The origin of these differences remains unclear.

3.1.4 FeTiO₃

FeTiO₃, ilmenite, is a common mineral from which titania and titanium are extracted.³⁰ FeTiO₃ is economically important because it can be used to produce industrial TiO₂ pigments. The structure of FeTiO₃, which is temperature and pressure dependent, is different from the traditional ABO₃ structure and is more complex. The ilmenite structure is the stable form of FeTiO₃ at ambient temperature and pressures.³¹ Ilmenite is based on a hexagonal-close-packed oxygen lattice with metal atoms occupying two-thirds of the available octahedral sites to form honeycomblike layers of edge-shared octahedral. The lattice parameters of ilmenite FeTiO₃ are $a = 5.088 \text{ \AA}$ and $c = 14.083 \text{ \AA}$.³¹

FeTiO₃ is a mixed-valence transition metal oxide with two different oxidation states for both iron, Fe²⁺ and Fe³⁺, and titanium, Ti³⁺ and Ti⁴⁺.³² In general, FeTiO₃ is regarded to be a p-type semiconductor with a band gap energy of 2.5 eV to 2.9 eV.³³⁻³⁵ Pure ilmenite is synthesized by a solid state reaction of TiO₂ and Fe₂O₃ above 1200 °C.³⁶ An hydrothermal method was reported to fabricate FeTiO₃ nanodiscs at 220 °C.³⁵

3.1.5 BiFeO₃

Bismuth ferrite is perhaps the only material that is both a ferromagnetic and a strong ferroelectric at room temperature.³⁷ Because of these properties, it is considered as one of the best potential materials for ferroelectric memory devices. Its unexpected large remnant polarization, which attracted the world's attention in

2003,³⁸ was found for thin films of BiFeO₃. Bismuth ferrite at room temperature has a rhombohedral structure (*R3c*),³⁹ as shown in figure 3-1.⁴⁰ The lattice parameters of the rhombohedral structure are $a = 5.6343 \text{ \AA}$ and $\alpha = 59.348^\circ$.⁴¹ Bi₂Fe₄O₉ and Bi₂₅FeO₃₉ are the main secondary phases that are likely to result from the synthesis. As bismuth is prone to volatilize at high temperatures, Bi₂Fe₄O₉ is the most common secondary phase observed in the products of high temperature reactions used to synthesize BiFeO₃.⁴² Its Curie temperature is reported to be between 810 °C to 830 °C.⁴³ BiFeO₃ is a p-type semiconductor,⁴⁴ with an optical band gap at room temperature that is reported to be between 2.3 to 2.8 eV.³⁷ The ferroelectric polarization of bulk BiFeO₃ is along the diagonals of the unit cell ([111] for the pseudocubic indices). A high polarization was reported in films with 50-60 $\mu\text{C}/\text{cm}^2$.³⁸ Ferroelectric BiFeO₃, with a narrow band gap, is used as core material in a heterostructure for visible light photochemical reaction in this research.

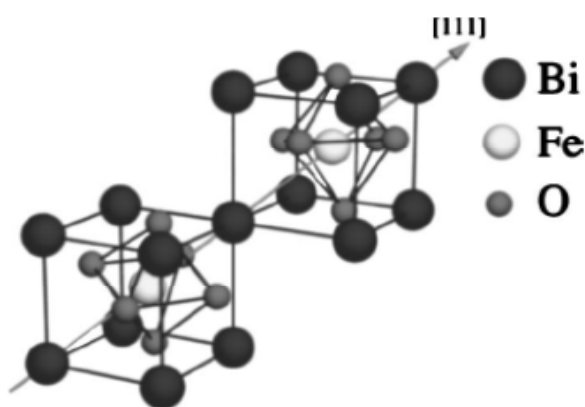


Figure 3-1 Schematic illustration of BiFeO₃ structure. (This figure is reproduced from reference 40.)

3.1.6 LaFeO₃

Perovskite LaFeO₃ is regarded as an important functional material and has many

possible applications as oxidation catalysts or gas sensors.⁴⁵ LaFeO_3 is non-ferroelectric with an orthorhombically distorted perovskite structure with the lattice parameters $a = 5.560 \text{ \AA}$, $b = 5.567 \text{ \AA}$ and $c = 7.864 \text{ \AA}$.^{46,47} LaFeO_3 is a p-type electrical conductor with a band gap of 2.0 eV to 2.5 eV, depending on the preparation method and material morphology.⁴⁸⁻⁵⁰ Non-ferroelectric LaFeO_3 is used as a control core material for comparison to BiFeO_3 .

3.1.7 YFeO_3

Analogous to LaFeO_3 , YFeO_3 is also an orthoferrite with weak ferromagnetic properties over its strong antiferromagnetic behavior; it has potential applications in magnetic field sensors and magneto-optical data storage devices.⁵¹ The Neel temperature is 644.5 K.⁵² YFeO_3 crystallizes in a distorted perovskite structure with an orthorhombic unit cell with the following lattice parameters: $a = 5.594 \text{ \AA}$, $b = 7.605 \text{ \AA}$, and $c = 5.281 \text{ \AA}$.⁵³ In addition, YFeO_3 is a p-type semiconductor with a band gap of 2.6 eV.^{54,55} YFeO_3 is also used in the present work as a nonferroelectric control core material for comparison to BiFeO_3 .

3.2 Experimental Setup

3.2.1 Core Preparation

Several types of perovskite, BaTiO_3 (ferroelectric), SrTiO_3 (non-ferroelectric),

PbTiO₃ (ferroelectric), BiFeO₃ (ferroelectric), LaFeO₃ (nonferroelectric), and YFeO₃ (nonferroelectric), as well as ilmenite FeTiO₃ (nonferroelectric), were chosen as the core materials. Al₂O₃ has a wide band gap and was used as the core material in control experiments as a material with a significantly larger bandgap than BaTiO₃ core SrTiO₃. BaTiO₃, SrTiO₃, PbTiO₃, FeTiO₃, Al₂O₃ are commercially available. BiFeO₃, LaFeO₃, and YFeO₃ were produced as described below. BaTiO₃ and SrTiO₃ were processed by molten salt flux method to obtain faceted powders. The following section presents a brief introduction to the fabrication of faceted (Ba,Sr)TiO₃ and powders of (Bi, La, Y)FeO₃.

3.2.1.1 Preparation of Faceted (Ba,Sr)TiO₃

Commercially available micron-sized powders of barium titanate (BaTiO₃, ALPHA AESAR, 99.7%) and strontium titanate (SrTiO₃, ACROS ORGANICS, >99%) were used as precursors to prepare faceted microcrystals. Faceted BaTiO₃ and SrTiO₃ powders were synthesized by the molten salt flux method, as reported previously.⁵⁶ Equal weights of BaTiO₃ and KCl (ACROS ORGANICS, >99%) were combined with ethanol, ball milled for several minutes, stirred continuously for 2 hours, and then dried at 70 °C for 12 h. The dried powder was transferred to an Al₂O₃ crucible and calcined at 1100 °C for 5 h with 5 °C/min heating/cooling rate. KCl was then removed by filtering with boiling water and washing repeatedly with distilled water. The faceted powder was then dried at 70 °C for 12 h.

3.2.1.2 *BiFeO₃ Preparation*

Micron-sized BiFeO₃ powders with different morphologies were prepared with a hydrothermal method that was modified from previously reported hydrothermal methods.⁵⁷ Equal amounts of 0.005 mol bismuth nitrate pentahydrate (Bi(NO₃)₃·5H₂O, ACROS ORGANICS, 98%) and iron nitrate nonahydrate (Fe(NO₃)₃·9H₂O, ACROS ORGANICS, 99+%) used as the starting materials were dissolved into 50 mL of 0.5 M dilute nitric acid (HNO₃, ACROS ORGANICS, 68%) solution under magnetic stirring at 70 °C for 30 minutes. After complete dissolution, 4 M potassium hydroxide (KOH, ACROS ORGANICS, 85.3%) solution was added dropwise into the above solution with constant stirring to co-precipitate Bi(OH)₃ and Fe(OH)₃ completely. The pH of the final solution was kept at 14. Then, the brown precipitate was filtered and washed several times using distilled water to remove K⁺, OH⁻, and NO₃⁻ ions. 50 mL of KOH was mixed with the precipitate in a 100 mL beaker. Potassium nitrate (KNO₃, ACROS ORGANICS, 99+%) was added into the mixture as a co-mineralizer to control the growth of powders. The suspension was stirred and dispersed at room temperature for 20 minutes and then transferred to a 125 mL acid digestion vessel with Teflon PFA inner walls (Parr Instrument Company), the structure of which is shown in figure 3-2.⁵⁸ The vessel was kept at 180 °C for different durations under auto generated pressure (related to the temperature and amount of water). After natural cooling to room temperature, the products were collected and washed with distilled water by centrifugation for several times (usually 3) to remove the residual K⁺, OH⁻, and NO₃⁻ ions. Then, the product was dried at 80 °C for 5 hours.

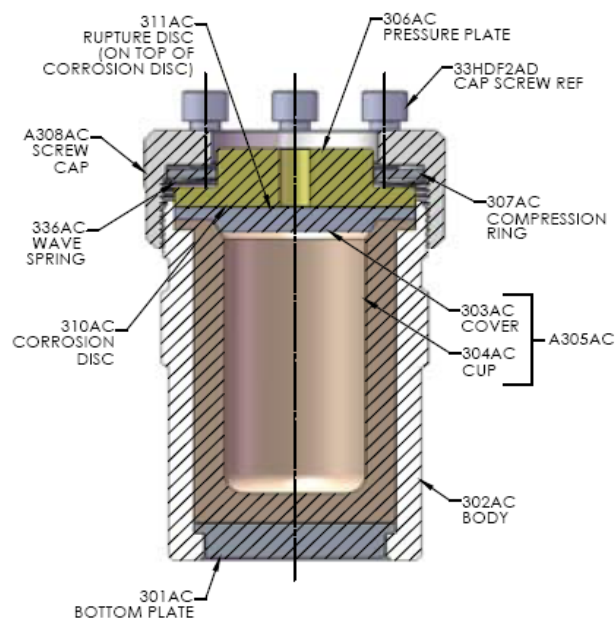


Figure 3-2 Structure of 125 mL acid digestion vessel. (This figure is reproduced from reference 58.)

3.2.1.3 LaFeO_3 Preparation

LaFeO_3 microcrystals were produced based on the EDTA initiated sol-gel method. 1.4 mol of EDTA ($\text{C}_{10}\text{H}_{16}\text{N}_2\text{O}_8$, ACROS, 99%) per mole of metal was dissolved into water at ambient temperature. 45 mL of ammonia (NH_3OH , FISHER SCIENTIFIC, 29.04%) was added dropwise, as slowly as possible, into the EDTA solution as slowly as possible to keep the pH around 7. 0.03 mol of lanthanum nitrate hexahydrate ($\text{La}(\text{NO}_3)_3 \cdot 6\text{H}_2\text{O}$, ACROS ORGANICS, 99.999%) and iron nitrate nonahydrate were mixed with the EDTA/ammonia solution. During this process, precipitation was avoided. The mixture was heated at 60 °C for 3 hours and then transferred to a drying oven for 2 days to obtain the black gel. The gel was then ground into powder and calcined at 600 °C (at a heating rate of 10° C /min) for 24 hours to burn off the organic compounds. The calcined powder was then annealed at

900° C for 24 hours (heated at 10 °C /min) for crystallization. The final product was collected after grinding the calcined powders.

3.2.1.4 *YFeO₃ Preparation*

Analogous to LaFeO₃, YFeO₃ microcrystals were fabricated using a sol-gel method with citric acid as a linking reagent. 0.03 mol of yttrium nitrate hexahydrate (Y(NO₃)₃·6H₂O, ACROS ORGANICS, 99%) and iron nitrate nonahydrate (Fe(NO₃)₃·9H₂O, ACROS ORGANICS, 99%+) were dissolved into 100 mL of 0.72 mol/L citric acid (C₆H₈O₇, ACROS ORGANICS, 99.5%) solution. 26.5 mL of ammonia was slowly added into the mixture. The color of the solution changed from red at pH = 3 to green at pH = 7. The pH of solution was neutral and stirred for 3 hours at 60° C. The solution was then dried at 130 °C for 2 days to form a xerogel. The ground powders were transferred to the furnace and annealed at 600° C (with a heating rate of 10° C /min) for 24 hours to burn off the organic compound. The calcined powder was ground again and then annealed at 900° C for 24 hours (with a heating rate of 10° C /min) for crystallization. The final product was collected after grinding the calcined powders.

3.2.2 Coating Process

Nanostructured (*ns*-)TiO₂ was prepared by the hydrolysis of TBOT^{59,60} (Ti(OC₄H₉)₄, ACROS ORGANICS, 99.0%), as described below. *ns*-TiO₂ was coated

on the microcrystalline (*mc*-) BaTiO₃ and SrTiO₃, for both commercial and faceted powders, as well as commercial *mc*-Al₂O₃, using an identical approach. A mixture of 9 mL water and 20 mL ethanol was first prepared. When used, core powders (\approx 1 g) were added to the mixture and dispersed using a 0.5 h ultrasonic treatment. HCl was added into the water/ethanol solutions to adjust the pH to be 3-4 (except for Al₂O₃ cores for which the pH was between 5 and 6). Another solution was prepared with a suitable amount (15 mL) of ethanol, 8.6 mL TBOT, and 1 mL of 2,4-pentanedione. The TBOT solution was added drop-wise to the water / ethanol solution over \approx 15 min. The mixture was stirred vigorously for 2h and then aged at 90 °C in a water bath for 9 h while stirring at 300 rpm. The final as-prepared product was obtained by centrifugation of the aged mixture, washing several times with ethanol, and drying at 80 °C for 24 h. Some of the as-prepared powder was sintered in air for 2 h at different temperatures to increase crystallinity and core-shell bonding. Samples were heated and cooled at 5 °C/min to temperatures between 400 °C and 600 °C. Commercial nanostructured (*ns*-) BaTiO₃ (US Research Nanomaterials, 99.9%) with the size of 100 nm from SEM was coated with *ns*-TiO₂ using the same procedure to the *mc*-BaTiO₃/*ns*-TiO₂ heterostructure powders. The powders were annealed at 500 °C for TiO₂ crystallization. PbTiO₃, FeTiO₃, and (Bi, La, Y)FeO₃ were coated with the same procedure but using 10 mL acetic acid to adjust pH (to avoid dissolution of the core).

Several control samples were also prepared or purchased. Degussa P25 TiO₂ (TiO₂, Parsippany, 99.5%) was purchased and served as the benchmark photocatalyst.

Mechanical mixtures of similar compositions to the heterostructured powders were also prepared. Equal weights of the core powders were mixed with Degussa P25 in ethanol and sonomechanically treated using an ultrasonic bath at 80 °C for 3 h. The mixtures were then dried at 70 °C for 12 h. The same sonomechanical procedure was used to treat Degussa P25. Some such mixtures were also further treated at elevated temperatures as described above.

All powders tested photocatalytically were loaded with 1 wt% Pt by an impregnation-reduction method.^{61,62} The as-prepared powders were impregnated with a known quantity of H₂PtCl₆ solution for 2 h while stirring. The powders with the adsorbed H₂PtCl₆ were reduced using a 5-fold excess of a NaOH and NaBH₄ for 2 h while stirring. The powders were then collected by centrifugation, rinsed with distilled water, and dried at 70 °C for 12 h.

3.2.3 Characterization

3.2.3.1 X-ray Powder Diffraction

X-ray diffraction (XRD) is a sensitive analytical tool that provides information about the crystallographic structure, crystallite size, chemical composition, crystallite orientation, interface properties, and homogeneity of samples. It is a useful characterization method that can quantify and qualify the crystalline phases in a solid.

All powders were characterized with x-ray diffraction using an x-ray diffractometer (PANalytical, X'Pert Pro, Philips, Netherlands) equipped with a

high-intensity CuK α radiation source. The wavelength for CuK α radiation is 1.5406 Å. The samples for analysis were ground using a mortar and pestle, followed by loading onto glass slides. Diffraction patterns were collected from 20 ° and 90 ° at a scanning rate of 3 °/minute with a step size of 0.05 °. The accelerating voltage was set to be 45 kV and the operating beam current was 45 mA.

3.2.3.2 *Scanning Electron Microscopy*

As shown in figure 3-3,⁶³ the interaction between the electron beam and a solid sample produces different types of emission. The electrons near the surface can be knocked out of the solid sample. Those electrons, called secondary electrons, can be detected by scanning electron microscopy (SEM) to analyze surface morphologies. SEM is advantageous to characterize powder morphology and size because of its ease of operation, simple sample preparation, large depth of field, and nanoscale resolution.

The morphologies of powders were investigated using a field emission scanning electron microscope (Philips XL-30) at accelerating voltages of 15 kV. Specifically, the powders for analysis were dispersed on carbon tape attached SEM stub. The excess loose powder was tapped off the stub.

3.2.3.3 *Transmission Electron Microscopy*

Transmission electron microscopy (TEM) is a powerful tool to analyze the internal structure of materials. In addition to internal structure analysis, another characteristic of TEM is to produce atomic-resolution images, which complement the

by SEM. The primary limitation for TEM is the complexity and difficulty of specimen preparation, which requires the sample to be thin enough for the beam to pass through. The specimen preparation for powders is however relatively simple. The difficulty for interpreting images is another disadvantage because TEM presents three dimensional structure on a two dimensional plane. In addition, the high energy electron beam used in TEM can damage the specimen irreversibly.

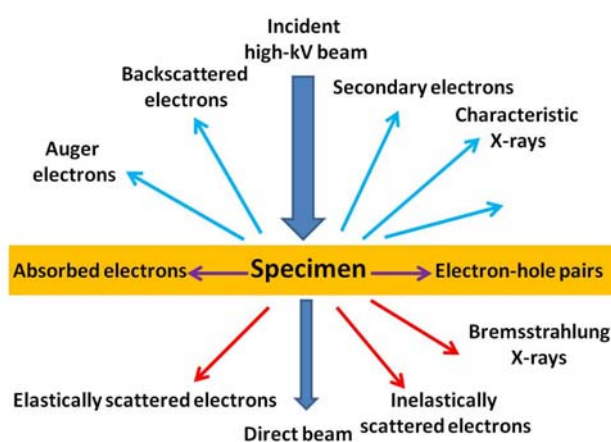


Figure 3-3 Emission produced by the interaction of an electron beam with a solid sample. (This figure is reproduced from reference 63.)

Transmission electron microscopy (2000EX, JEOL, Peabody, MA) was carried out using 200 kV for an accelerating voltage; it was used to determine the local structure of the heterostructured photocatalysts. Powders were ultrasonically dispersed in methanol and several drops of the suspension were distributed drop-wise onto the surface of a 200 mesh copper grid coated with a carbon support film. This grid was placed into the TEM. High Resolution images were taken with another transmission electron microscopy (F20, TECNAI, Hillsboro, OR) working at an accelerating voltage of 200 kV with a field emission electron gun.

3.2.3.4 Gas Adsorption Analysis

The surface area of particles can be evaluated by several methods. The most common technique is based on the theory developed by Brunauer, Emmett and Teller (BET). This theory establishes the mathematical model for the analysis of multilayer gas adsorption (N_2 is commonly utilized) on solid surfaces and deduces an equation to calculate the number of adsorbed molecules.⁶⁴ This method is an accurate and direct expression for specific surface area measurements for particles. Surface area is closely related to the particle size. Figure 3-4 illustrates how different characterization methods can be used to analyze “particle size”.⁶⁵ In general, “particle size” observed by SEM refers to the average aggregate size. “Particle size” derived from Scherrer’s equation⁶⁶ based on XRD line broadening is actually an average crystalline size. “Particle size” calculated from the BET surface area based on equation (3-1) is the average size of single particles, which may be composed of crystallites and aggregates.

$$(3-1) D = \frac{6000}{\rho S}$$

D is the average particle size (nm), ρ the powder density (g/cm^3), and S the specific surface area measured via the BET method.⁶⁵ Gas adsorption analysis also can be employed to determine pore size and volume based on the Barret, Joyner and Halenda (BJH) method.⁶⁷

In our experiment, the surface area was determined using nitrogen adsorption-desorption measurements (using a Nova 2200e, Quantachrome, FL), which were analyzed with the Brunauer-Emmett-Teller (BET) method. These

measurements were carried out at 77 K using a multi-point method after the sample was vacuum-degassed for 3 hours at 300 °C to remove moisture. The BET surface area measurement is based on the isothermal curve of gas adsorption and desorption at low relative pressure ($0.05 < P/P_0 < 0.3$). The mean pore size and volume were determined from the same measurements using the Barret-Joyner-Halenda (BJH) model. The pore volume was measured at the $P/P_0 = 0.99$ point.

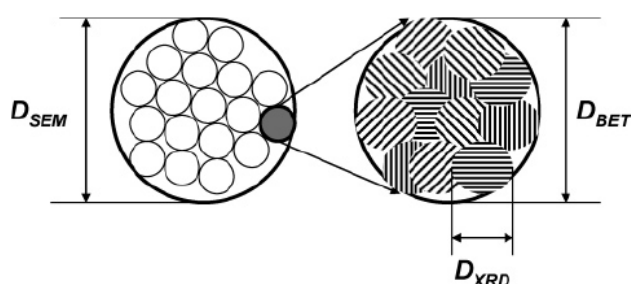


Figure 3-4 Schematic representation of various characterization methods for particle size. (This figure is reproduced from reference 65.)

3.2.3.5 Diffuse Reflectance Spectroscopy and Absorbance Spectroscopy

Diffuse reflectance spectroscopy (DRS) was used to analyze the optical properties of core-shell photocatalyst. Herein, the optical properties refer to the absorption of core-shell powders. Because it is not possible to measure the optical absorbance of powders, the reflectance is measured and then converted to the absorption by Kubelka-Munk (K-M) function. Reflectance is defined as the fraction of incident radiation reflected by a surface and the reflectance is generally divided into the specular reflectance and diffuse reflectance. In our experiment, the primary reflectance is diffuse reflectance and the reflectance spectra were recorded by a UV-vis spectrophotometer (USB2000 Ocean Optics) equipped with R600-7 reflectance probe

optimized for 250-800 nm region. The probe is composed of a bundle of 7 optical fibers in the stainless steel ferrule, involving 6 illumination fibers around 1 detecting fiber, with the diameter of 600 μm . The probe was then positioned with RPH-1 Probe holder at 45° for diffuse reflectance. The RPH-1 probe holder is an anodized aluminum platform with two holes, one at 45° and one at 90°, for diffuse reflectance and specular reflectance measurements, respectively. The reflectance data is calculated by the SpectraSuite Software and expressed as a percentage (% R_λ) following the equation below:⁶⁸

$$\%R_\lambda = \frac{S_\lambda - D_\lambda}{R_\lambda - D_\lambda} \times 100\%$$

where S_λ is the sample intensity at wavelength λ , D_λ is the dark intensity at wavelength λ , R_λ is the reference intensity at wavelength λ . The dark spectrum was recorded by measuring the reflectance from a flat standard surface with the UV-visible light source off. The PTFE standard sample with uniform reflectance between 250 nm and 2000 nm was utilized as the reference. After the reflectance data were recorded, the K-M function was used to convert the data to obtain the absorbance of the sample:⁶⁹

$$F(R) = \frac{k}{s} = \frac{(1 - R)^2}{2R}$$

where k and s are absorption and scattering coefficients, respectively, and R is the reflectance at the front face. $F(R)$ is the Kubelka-Munk function and is an indicator of light absorption ability, with higher $F(R)$ values representing stronger photoabsorption capability.

Absorbance spectroscopy was used to measure the absorbance change of dye

solutions before and after the photochemical reaction. Absorbance can be defined and expressed by Beer's law:

$$A = \log \frac{I_0}{I} = \log \frac{1}{T} = \alpha lc$$

where A is absorbance of the solution, I_0 is the incident intensity, I is the transmitted intensity, T is the transmittance, α is absorption coefficient of the solution, l is the light path length, and c is the concentration of the absorber in solution. The value of absorbance reflects the absorption photons that promote electrons from the highest occupied molecular orbital (HOMO) to the lowest unoccupied molecular orbital (LUMO) in the absorbing molecule.³ In our experiment, the intensity of absorbance is linearly proportional to the concentration of dye and can be used to evaluate photochemical dye degradation.

The absorbance spectra were recorded using a UV-vis spectrophotometer (USB2000, Ocean Optics) with a 5 W direct attached UV/VIS/NIR Deuterium tungsten light source (200-1100 nm). The absorbance data is calculated by the SpectraSuite Software and expressed as a percentage (% R_λ) following the equation below:⁶⁸

$$\%A_\lambda = -\log \left(\frac{S_\lambda - D_\lambda}{R_\lambda - D_\lambda} \right)$$

where S_λ is the sample intensity at wavelength λ , D_λ is the dark intensity at wavelength λ , R_λ is the reference intensity at wavelength λ . The dark spectrum was recorded by measuring the absorbance of the standard when the lighting source was turned off. The reference spectrum was recorded by measuring the absorbance of deionized water.

3.2.3.6 Gas Chromatography

Gas chromatography (GC) was used to determine the volume of hydrogen produced from the photocatalysts. The basic operating mechanism of a gas chromatography is to vaporize the sample in the heated injector, separate the components in a column and then analyze the components with a detector. The detector utilized in this experiment is called a thermal conductivity detector (TCD). In this experiment, the volume of hydrogen synthesized from the reaction was quantified by periodically withdrawing gas from the headspace in the reactor using a 0.5 mL syringe and injecting it into the gas chromatograph (Shimadzu, MD; GC-14A, TCD). Ar was employed as the carrier gas.

3.2.4 Photocatalytic Activity Characterization

3.2.4.1 Photocatalytic Hydrogen Production

The photocatalytic activities of powders were evaluated by measuring hydrogen generation. The powders were suspended in a water-methanol mixture in a gas-tight reactor system (similar to those described elsewhere)⁷⁰ and illuminated by a 450 W medium-pressure mercury immersion lamp (ACE Glass, NJ). The schematic of reaction system is shown in figure 3-5. This lamp emits approximately 40 %-48 % of total energy in the ultraviolet portion of the spectrum and 40 %-43 % in the visible light region. The residual part of spectrum is balanced in the infrared. The detailed spectral intensity distribution is shown in table 3-1. The lamp was inserted into a borosilicate immersion well (ACE Glass, NJ) to allow the transmittance of irradiation

with wavelengths longer than 280 nm. The exact transmittance graph of the borosilicate immersion well is shown in figure 3-6.⁷¹ The immersion well was held inside the 500 mL inner reaction chamber. A quartz immersion well (ACE Glass, NJ) was utilized for selected experiments to allow the transmittance of irradiation from the whole spectrum emitted from the lamp. A certain mass (0.4 g, 1 wt% Pt) of photocatalyst was added to a distilled water / methanol (92 / 8 mL) solution and placed in the outer reaction chamber. Platinum provides reaction sites and decreases the activation energy for hydrogen production.^{72,73} Methanol is one of the most common sacrificial reagents and serves as a hole scavenger, forming CO₂ rather than O₂.⁷³⁻⁷⁵ The system was evacuated several times prior to irradiation. The pressure prior to reaction was 5 Torr. The reaction vessel was maintained at room temperature by adjusting the cooling water flow rate.

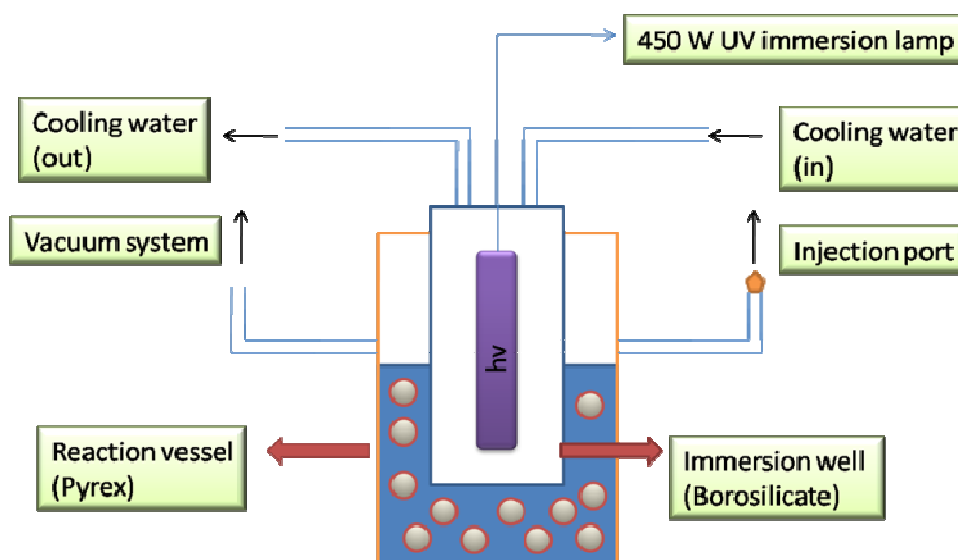


Figure 3-5 Schematic of photocatalytic hydrogen production reactor setup.

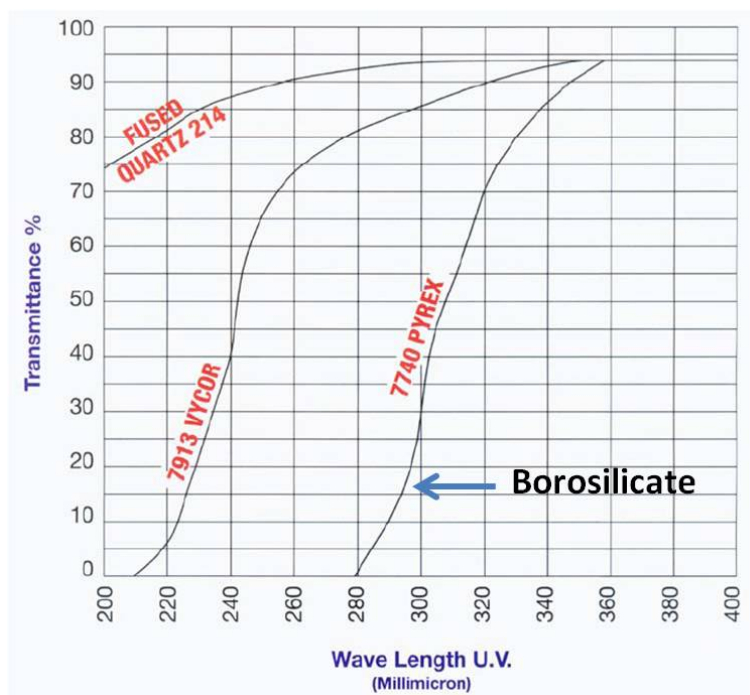


Figure 3-6 Transmittance graph of the borosilicate immersion well. (This figure is reproduced from reference 71.)

Table 3-1 Spectral energy distribution of 450 W medium-pressure mercury immersion lamp.

Wavelength (nm)	Intensity (W)	Wavelength (nm)	Intensity (W)	Wavelength (nm)	Intensity (W)
1367	2.6	1129	3.3	1014	10.5
578	20.0	546	24.5	436	20.2
405	11.0	366	25.6	334	2.4
313	13.2	303	7.2	297	4.3
289	1.6	280	2.4	275	0.7
270	1.0	265	4.0	257	1.5

3.2.4.2 Photocatalytic Dye Degradation

Another method used to evaluate the photocatalytic activity of powdered photocatalysts was organic dye degradation. The rate of degradation of methylene blue (MB) under UV and visible light was used as a measure of photochemical activity. Commercial available methylene blue (Fisher Scientific) was purchased in

powder form. A fixed amount of powder was dissolved into 4 L deionized water so that the concentration of the dye solution was 10^{-5} M. The solution was stored in the 4 L flask sealed with glass stopper. A schematic of experiment setup is shown in figure 3-7.

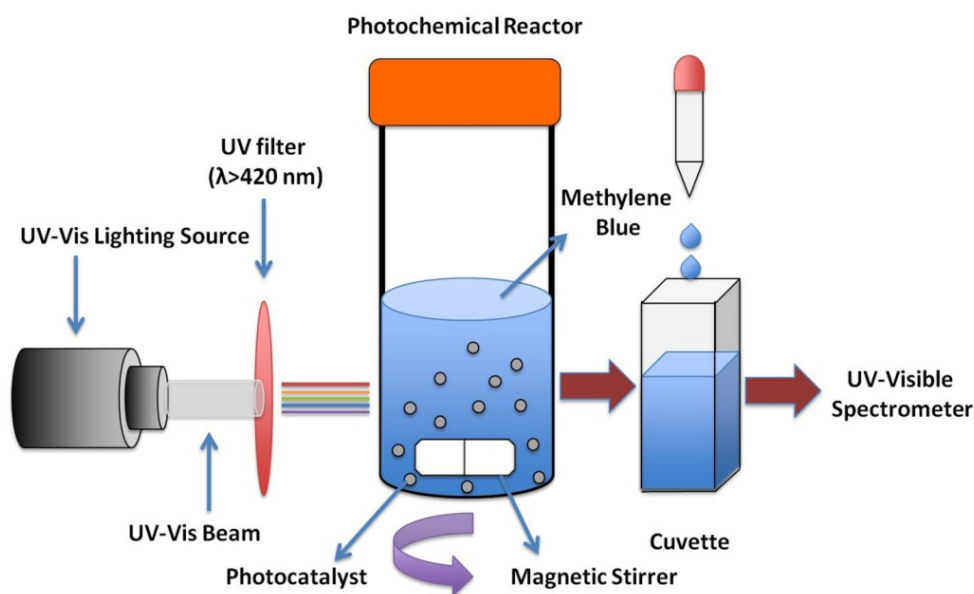


Figure 3-7 Schematic of photocatalytic dye degradation setup.

A 300 W high pressure mercury lamp was used as the illumination source. The emission spectrum of this mercury lamp is shown in figure 3-8.³ From this figure, it can be seen that the intensity of this lamp is greater than $30 \text{ mW}/(\text{m}^2 \text{ nm})$ from 300 nm to 800 nm. There is a sharp decrease in the intensity of the light below 300 nm. The band gaps of the semiconductor photocatalysts used in these experiments are between 2.0 eV to 3.2 eV, which means that they absorb light between 390 nm to 620 nm. Based on figure 3-7, the energy of photons from the illumination source is sufficient to excite the electrons in the semiconductor photocatalysts studied here.

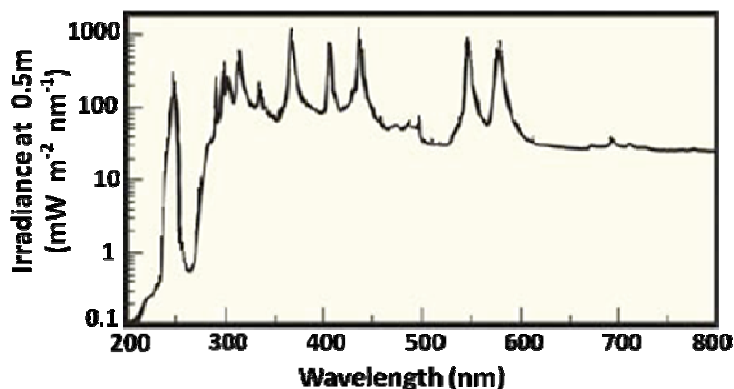


Figure 3-8 Emission spectrum of 300 W mercury lamp used in the experiment. (This figure is reproduced from reference 3.)

To investigate the visible light reactivity of photocatalysts, a UV cutoff filter (Oriel, $\lambda > 420$ nm) with 20 cm^2 window was placed in front of the 100 mL home-made quartz photochemical reactor to absorb the UV light. An aqueous suspension of 0.3 g of photocatalyst was added to 65 mL of 10^{-5} M MB solution prepared in the previous step and poured into the 100 mL quartz photochemical reactor. Prior to irradiation, the suspension was stirred continuously for 2 hours in the dark to saturate the powders with the dye solution and reach the adsorption/desorption equilibrium between the powder and solution. The photochemical reaction was carried out for 5 hours and 5 mL samples were removed each hour with dropper for absorption measurements. The degradation of methylene blue was evaluated by comparing the intensity of the absorbance peak at 663.89 nm (denoted as C) and the initial intensity (denoted as C_0) before irradiation.

3.3 References

- (1) Rabe, K. M.; Ahn, C. H.; Triscone, J. M. *Physics of Ferroelectrics: A Modern Perspective*; Springer, 2007.
- (2) K.H. Hellwege; Hellwege, A. M. *Ferroelectrics and Related Substances*; Springer Verlag: Berlin, 1969; Vol. 3.

- (3) Bhardwaj, A. The Composition Dependence of the Photochemical Reactivity of Barium Strontium Titanates, Carnegie Mellon University, 2008.
- (4) Cardona, M. *Physical Review* **1965**, *140*, A651.
- (5) Casella, R. C.; Keller, S. P. *Physical Review* **1959**, *116*, 1469.
- (6) Zhong, W.; King-Smith, R. D.; Vanderbilt, D. *Physical Review Letters* **1994**, *72*, 3618.
- (7) Arlt, G.; Sasko, P. *Journal of Applied Physics* **1980**, *51*, 4956.
- (8) Chan, N. H.; Sharma, R. K.; Smyth, D. M. *Journal of the American Ceramic Society* **1981**, *64*, 556.
- (9) Berbenni, V.; Marini, A.; Bruni, G. *Thermochimica Acta* **2001**, *374*, 151.
- (10) Wang, Y. W.; Xu, H.; Wang, X. B.; Zhang, X.; Jia, H. M.; Zhang, L. Z.; Qiu, J. R. *The Journal of Physical Chemistry B* **2006**, *110*, 13835.
- (11) Hernandez, B. A.; Chang, K. S.; Fisher, E. R.; Dorhout, P. K. *Chemistry of Materials* **2002**, *14*, 480.
- (12) Dawber, M.; Lichtensteiger, C.; Cantoni, M.; Veithen, M.; Ghosez, P.; Johnston, K.; Rabe, K. M.; Triscone, J. M. *Physical Review Letters* **2005**, *95*.
- (13) Mavroides, J. G. *Materials Research Bulletin* **1978**, *13*, 1379.
- (14) Ellialtioglu, S.; Wolfram, T.; Henrich, V. E. *Solid State Communications* **1978**, *27*, 321.
- (15) Fleury, P. A.; Scott, J. F.; Worlock, J. M. *Physical Review Letters* **1968**, *21*, 16.
- (16) Bickel, N.; Schmidt, G.; Heinz, K.; Muller, K. *Physical Review Letters* **1989**, *62*, 2009.
- (17) Haeni, J. H.; Irvin, P.; Chang, W.; Uecker, R.; Reiche, P.; Li, Y. L.; Choudhury, S.; Tian, W.; Hawley, M. E.; Craigo, B.; Tagantsev, A. K.; Pan, X. Q.; Streiffner, S. K.; Chen, L. Q.; Kirchoefer, S. W.; Levy, J.; Schlom, D. G. *Nature* **2004**, *430*, 758.
- (18) Giocondi, J. L.; Rohrer, G. S. *Journal of the American Ceramic Society* **2003**, *86*, 1182.
- (19) Antons, A.; Neaton, J. B.; Rabe, K. M.; Vanderbilt, D. *Physical Review B* **2005**, *71*, 024102.
- (20) T. Mitsui; S. Nomura; Adachi, M. *Oxides, Landolt-Bornstein: Numerical Data and Functional Relationships in Science and Technology, Group III*; Springer: Berlin, 1981.
- (21) Saghi-Szabo, G.; Cohen, R. E.; Krakauer, H. *Physical Review Letters* **1998**, *80*, 4321.
- (22) Damjanovic, D. *Reports on Progress in Physics* **1998**, *61*, 1267.
- (23) Sani, A.; Hanfland, M.; Levy, D. *Journal of Physics-Condensed Matter* **2002**, *14*, 10601.
- (24) Shirane, G.; Hoshino, S. *Journal of the Physical Society of Japan* **1951**, *6*, 265.
- (25) Lehnen, P.; Dec, J.; Kleemann, W. *Journal of Physics D-Applied Physics* **2000**, *33*, 1932.
- (26) Bhide, V. G.; Deshmukh, K. G.; Hegde, M. S. *Physica* **1962**, *28*, 871.
- (27) Piskunov, S.; Heifets, E.; Eglitis, R. I.; Borstel, G. *Computational Materials Science* **2004**, *29*, 165.
- (28) de Lazaro, S.; Longo, E.; Sambrano, J. R.; Beltran, A. *Surface Science* **2004**, *552*, 149.
- (29) Arney, D.; Watkins, T.; Maggard, P. A. *Journal of the American Ceramic Society* **2010**, in press.
- (30) Haggerty, S. E.; Sautter, V. *Science* **1990**, *248*, 993.
- (31) Wilson, N. C.; Russo, S. P.; Muscat, J.; Harrison, N. M. *Physical Review B* **2005**, *72*, 024110.
- (32) Zhang, B.; Katsura, T.; Shatskiy, A.; Matsuzaki, T.; Wu, X. *Physical Review B* **2006**, *73*, 134104.

- (33) Ishikawa, Y.; Sawada, S. *Journal of the Physical Society of Japan* **1956**, *11*, 496.
- (34) Ginley, D. S.; Butler, M. A. *Journal of Applied Physics* **1977**, *48*, 2019.
- (35) Kim, Y. J.; Gao, B.; Han, S. Y.; Jung, M. H.; Chakraborty, A. K.; Ko, T.; Lee, C.; Lee, W. I. *The Journal of Physical Chemistry C* **2009**, *113*, 19179.
- (36) Naylor, B. F.; Cook, O. A. *Journal of the American Chemical Society* **1946**, *68*, 1003.
- (37) Gustau, C.; James, F. S. *Advanced Materials* **2009**, *21*, 2463.
- (38) Wang, J.; Neaton, J. B.; Zheng, H.; Nagarajan, V.; Ogale, S. B.; Liu, B.; Viehland, D.; Vaithyanathan, V.; Schlom, D. G.; Waghmare, U. V.; Spaldin, N. A.; Rabe, K. M.; Wuttig, M.; Ramesh, R. *Science* **2003**, *299*, 1719.
- (39) Moreau, J. M.; Michel, C.; Gerson, R.; James, W. J. *Journal of Physics and Chemistry of Solids* **1971**, *32*, 1315.
- (40) Neaton, J. B.; Ederer, C.; Waghmare, U. V.; Spaldin, N. A.; Rabe, K. M. *Physical Review B* **2005**, *71*, 014113.
- (41) Kubel, F.; Schmid, H. *Acta Crystallographica Section B-Structural Science* **1990**, *46*, 698.
- (42) G. D, A.; W. J, J.; R, G. *Journal of the American Ceramic Society* **1967**, *50*, 437.
- (43) Fischer, P.; Polomska, M.; Sosnowska, I.; Szymanski, M. *Journal of Physics C-Solid State Physics* **1980**, *13*, 1931.
- (44) Poghosian, A. S.; Abovian, H. V.; Avakian, P. B.; Mkrtchian, S. H.; Haroutunian, V. M. *Sensors and Actuators B-Chemical* **1991**, *4*, 545.
- (45) Li, K.; Wang, D.; Wu, F.; Xie, T.; Li, T. *Materials Chemistry and Physics* **2000**, *64*, 269.
- (46) Zheng, W.; Liu, R.; Peng, D.; Meng, G. *Materials Letters* **2000**, *43*, 19.
- (47) Nakayama, S. *Journal of Materials Science* **2001**, *36*, 5643.
- (48) Bocquet, A. E.; Fujimori, A.; Mizokawa, T.; Saitoh, T.; Namatame, H.; Suga, S.; Kimizuka, N.; Takeda, Y.; Takano, M. *Physical Review B* **1992**, *45*, 1561.
- (49) Arima, T.; Tokura, Y.; Torrance, J. B. *Physical Review B* **1993**, *48*, 17006.
- (50) Shein, I.; Shein, K.; Kozhevnikov, V.; Ivanovskii, A. *Physics of the Solid State* **2005**, *47*, 2082.
- (51) Ripka, P.; Vertesy, G. *Journal of Magnetism and Magnetic Materials* **2000**, *215*, 795.
- (52) Shen, H.; Xu, J. Y.; Wu, A. H.; Zhao, J. T.; Shi, M. L. *Materials Science and Engineering B-Advanced Functional Solid-State Materials* **2009**, *157*, 77.
- (53) Geller, S. *Journal of Chemical Physics* **1956**, *24*, 1236.
- (54) Butler, M. A.; Ginley, D. S.; Eibschutz, M. *Journal of Applied Physics* **1977**, *48*, 3070.
- (55) Mathur, S.; Veith, M.; Rapalaviciute, R.; Shen, H.; Goya, G. F.; Martins Filho, W. L.; Berquo, T. S. *Chemistry of Materials* **2004**, *16*, 1906.
- (56) Giocondi, J. L.; Rohrer, G. S. *Topics in Catalysis* **2008**, *49*, 18.
- (57) Chen, F.; Zhang, Q. F.; Li, J. H.; Qi, Y. J.; Lu, C. J.; Chen, X. B.; Ren, X. M.; Zhao, Y. *Applied Physics Letters* **2006**, *89*, 092910.
- (58) Hitoki, G.; Takata, T.; Kondo, J. N.; Hara, M.; Kobayashi, H.; Domen, K. *Chemical Communications* **2002**, 1698.
- (59) Li, S.; Lin, Y. H.; Zhang, B. P.; Li, J. F.; Nan, C. W. *Journal of Applied Physics* **2009**, *105*, 054310.
- (60) Ye, M.; Zhang, Q.; Hu, Y.; Ge, J.; Lu, Z.; He, L.; Chen, Z.; Yin, Y. *Chemistry – A European Journal* **2010**, *16*, 6243.

- (61) Vorontsov, A. V.; Stoyanova, I. V.; Kozlov, D. V.; Simagina, V. I.; Savinov, E. N. *Journal of Catalysis* **2000**, *189*, 360.
- (62) He, Z. Q.; Xie, L.; Tu, J. J.; Song, S.; Liu, W. P.; Liu, Z. W.; Fan, J. Q.; Liu, Q.; Chen, J. M. *The Journal of Physical Chemistry C* **2010**, *114*, 526.
- (63) Williams, D. B.; Carter, C. B. *Transmission Electron Microscopy : A Textbook for Materials Science*; Springer: New York, 1996.
- (64) Brunauer, S.; Emmett, P. H.; Teller, E. *Journal of the American Chemical Society* **1938**, *60*, 309.
- (65) Baiju, K. V.; Shukla, S.; Sandhya, K. S.; James, J.; Warriar, K. G. K. *The Journal of Physical Chemistry C* **2007**, *111*, 7612.
- (66) Cullity, B. D.; Stock, S. R. *Elements of X-Ray Diffraction*; Addison-Wesley Publishing Co: MA, 1978.
- (67) Barrett, E. P.; Joyner, L. G.; Halenda, P. P. *Journal of the American Chemical Society* **1951**, *73*, 373.
- (68) "USB2000 Fiber Optic Spectrometer Installation and Operation Manual."
- (69) Wang, X. C.; Yu, J. C.; Ho, C. M.; Hou, Y. D.; Fu, X. Z. *Langmuir* **2005**, *21*, 2552.
- (70) Jain, V. P.; Proctor, A. *Journal of Agricultural and Food Chemistry* **2006**, *54*, 5590.
- (71) "ACE Glass Lamp General Operating Instructions."
- (72) Maeda, K.; Domen, K. *Journal of Physical Chemistry Letters* **2010**, *1*, 2655.
- (73) Kudo, A.; Miseki, Y. *Chemical Society Reviews* **2009**, *38*, 253.
- (74) Kato, H.; Kudo, A. *Journal of Physical Chemistry B* **2002**, *106*, 5029.
- (75) Shi, J. Y.; Chen, J.; Feng, Z. C.; Chen, T.; Lian, Y. X.; Wang, X. L.; Li, C. *The Journal of Physical Chemistry C* **2007**, *111*, 693.

4. Photocatalytic Activity of (Ba, Sr)TiO₃/TiO₂

In this chapter, the photocatalytic properties of heterostructured powders, which is designed based on the model proposed in Chapter 1, will be described. Measurements of hydrogen production from ferroelectric BaTiO₃ and nonferroelectric SrTiO₃ will be used to test the influence of the internal field effect on the photocatalytic reactivity of these heterostructured photocatalysts. To investigate the effect of the interface between the core and shell, a mechanical mixture of P25 and BaTiO₃ was employed as a control. BaTiO₃ nanoparticles were used as the core materials and coated with nanostructured TiO₂ with the same processing procedures that were used to make the microcrystalline (*mc*-) BaTiO₃/nanostructured (*ns*-)TiO₂ heterostructures. The comparison of these two heterostructures reveals the influence of core size on the photocatalytic activity of the heterostructured photocatalyst. Meanwhile, micron-sized Al₂O₃ coated with TiO₂ was utilized to determine how the photocatalytic activity is affected by a core that does not absorb light.

4.1 Hydrogen Production from BaTiO₃/TiO₂

4.1.1 BaTiO₃/TiO₂ (Sol-gel)

4.1.1.1 Phase Characterization

The powder x-ray diffraction patterns of several representative photocatalysts are

given in figure 4-1 for: platinized (a) *mc*-Faceted BaTiO₃ (*mc*: micron sized), (b) *ns*-TiO₂ (*ns*: nanostructured) annealed at 500 °C in air, and (c) *mc*-F-BaTiO₃ core/*ns*-TiO₂ (F: faceted) shell annealed at 500 °C in air. All powders in this chapter are platinized with 1 wt% loading. All diffraction peaks could be indexed to BaTiO₃ (JCPDS 05-0626), anatase TiO₂ (JCPDS 46-1237), or rutile TiO₂ (JCPDS 33-1381), with the latter two marked in (b) as A and R, respectively. The photocatalytic properties of TiO₂ are believed to be affected by crystalline quality and phase composition.^{1,2} The effect of annealing temperature on the crystallinity and other parameters of core-shell particles will be discussed in detail in Chapter 5. The diffraction pattern of the BaTiO₃/TiO₂ composite confirms no extra phases were formed, which is consistent with the well-known phase equilibria of this system. The percentage of anatase and rutile in TiO₂ can be calculated by the following equation:³

$$(4-1) W_R = \frac{0.79A_r}{0.79A_r + A_a}$$

Where W_R is the mass fraction of rutile, A_r is the integrated intensity of the anatase (101) peak, and A_a is the integrated intensity of rutile (110) peak. The amount of rutile in the composite was different from the amount of rutile in the titania without BaTiO₃. This suggests that the BaTiO₃ affects the crystallization of the titania.

4.1.1.2 Morphology of Core Materials

Field emission scanning electron microscopy (SEM) was performed to characterize the particle size and morphology of powders utilized in this experiment. Figure 4-2 shows the commercial BaTiO₃ powders and the faceted particles treated in

molten salts. The inset shows a higher magnification of the faceted material. The powders treated in molten salt show facets with a well defined morphology and relatively flat surfaces. The morphology of the as-received powders is irregular; the particle size is non-uniform and the surfaces are rougher.

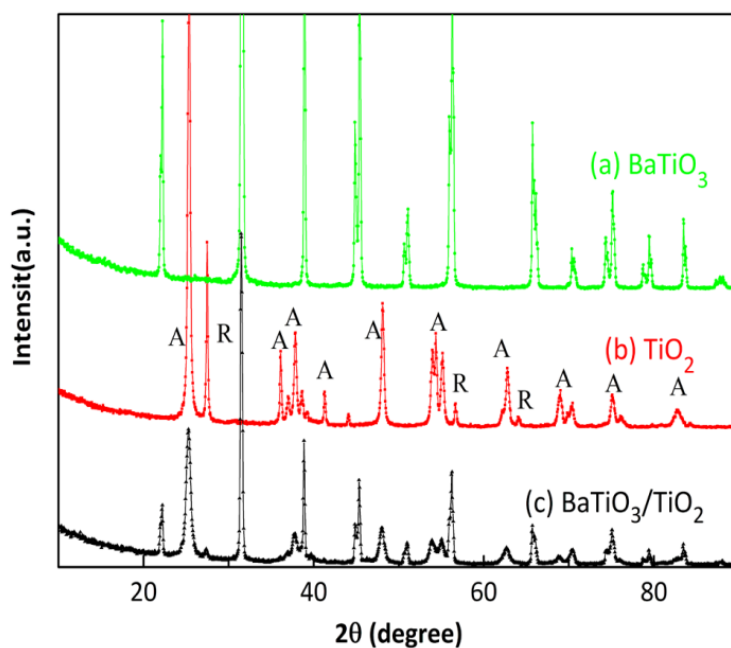


Figure 4-1 Powder x-ray diffraction patterns of platinumized (a) BaTiO₃, (b) TiO₂, and (c) BaTiO₃/TiO₂ annealed at 600 °C.

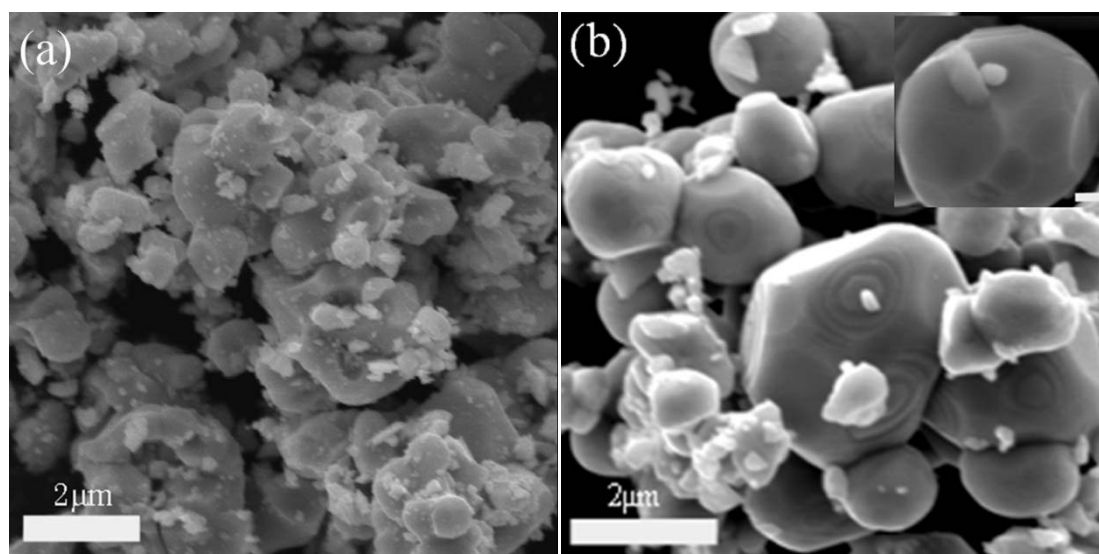


Figure 4-2 The morphology of BaTiO₃ powders (a) before treatment and (b) after molten salt treatment (The inset is high magnification of powders prepared from molten salt method. The inside scale bar is referred to 300 nm.)

4.1.1.3 Heterostructure Characterization

Transmission electron microscopy (TEM) was used to characterize the core/shell structure of heterostructured BaTiO₃/TiO₂. In figure 4-3, bright field (BF) TEM images are shown of the *mc*-BaTiO₃ core/*ns*-TiO₂ shell powders that were annealed at 600 °C and impregnated with Pt. These heterostructured powders had XRD patterns similar to that shown in figure 4-1. In figure 4-3, the dark (electron opaque) region corresponds to the micron-sized BaTiO₃ crystallite, the light grey regions to free space, and the interfacial region with mottled contrast to the *ns*-TiO₂ shell. The interface between the core and shell is sharp and clear in figure 4-3 (a), at low magnification, though curvature to the particle and varying local through-thickness coating densities render the interface less clear in the higher magnification image. The *ns*-TiO₂ shell is shown in figure 4-3 (a) to surround the BaTiO₃ microcrystal, though the local thickness varies significantly. This image is representative of the coated microcrystalline powders and confirms the core-shell nature of heterostructured powders. An image taken at a higher magnification is shown in figure 4-3 (b), in which the mottled contrast of the shell arises from details of the nanostructure and morphology of the coating. The shell thickness is in the range of 80 nm to 100 nm (in this region) and the TiO₂ particles are faceted in shape and range from 20-40 nm in diameter. The small black dots on the surfaces of TiO₂ are Pt particles. Though the core particles are uniformly coated, it is not clear how dense these shells are from the TEM cross-section, but the multi-scale nature of the microstructure is clearly preserved during this high temperature annealing.

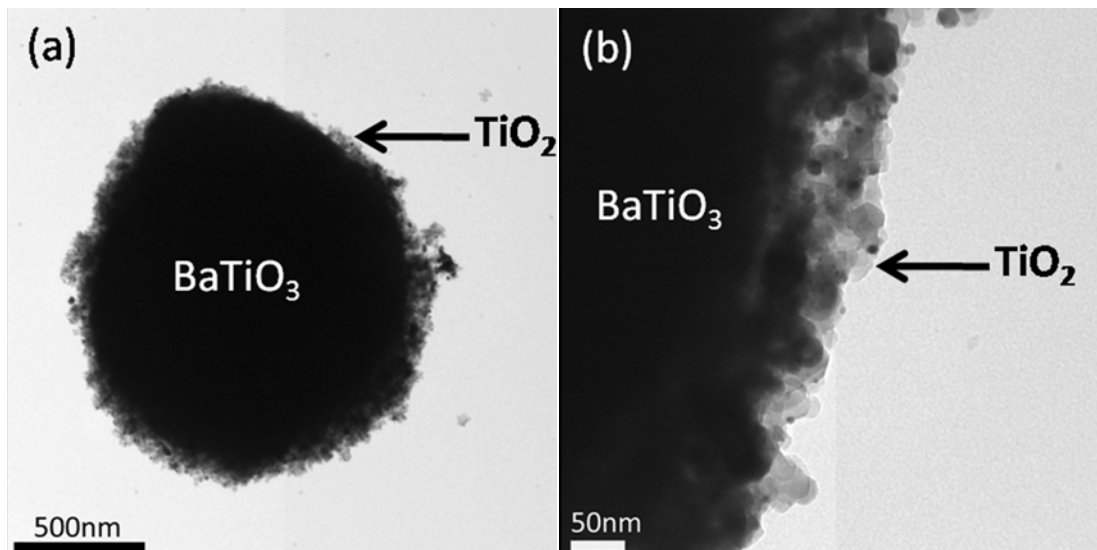


Figure 4-3 Bright field TEM images of a platinumized heterostructured particle composed of a *mc*-BaTiO₃ core and a *ns*-TiO₂ shell annealed at 600 °C. (a) shows the entire particle and (b) shows a higher magnification of the coating.

4.1.1.4 Surface Area Characterization

To determine the surface areas of the heterostructured particles and the pore morphologies of the nanostructured shells, gas adsorption measurements were carried out and analyzed with the BET and BJH methods. The results are listed in table 4-1. The isothermal curve of adsorption and desorption, and pore size distribution calculated from the desorption branch of the isothermal curve of *mc*-FBaTiO₃/*ns*-TiO₂, are shown in figure 4-4. Figure 4-4 (a) shows that the pore size distribution is narrow and the most common pore size is about 4 nm. The BJH measurement shows the mean pore radius of the sample is 4.3 nm. These measurements confirmed the mesoporous structure of the heterostructure. When the mean pore size and pore volume of the components (BaTiO₃ and TiO₂) and the heterostructure are compared, it is clear that the mesoporous structure arises from the processing method rather than the components. The mesoporosity is primary from the

pores between different TiO₂ grains. The addition of organic molecule 2,4 pentanedione also can serve as a structural-directing agent to form the mesoporous structure. The isothermal curve of N₂ adsorption/desorption is shown in figure 4-4 (b). The hysteresis loop of the isothermal curve can be observed and this isotherm is a type IV curve (BDDT classification). This also provides confirmation that the *mc*-BaTiO₃/*ns*-TiO₂ heterostructure has a mesoporous structure. The surface area and pore morphologies data shown in table 4-1 show that heterostructures created from faceted and commercial BaTiO₃ are comparable.

Table 4-1 Surface area and pore morphologies of F-BaTiO₃/TiO₂, C-BaTiO₃/TiO₂ and TiO₂ annealed at 600°C and commercial BaTiO₃.

Composition	Surface area (m ² /g)	Pore volume (cc/g)	Pore radius D _v (r) (Å)	V _{H₂,6h} μmol/m ²	R _{H₂} μmol•g ⁻¹ h ⁻¹
F-BaTiO ₃ /TiO ₂	44	0.14	43	28	205
C-BaTiO ₃ /TiO ₂	36	0.10	43	19	114
TiO ₂	16	0.06	19	18	48
BaTiO ₃	0.8	0.003	16	0	0

The SEM images indicated that the particle size is in the 1-2 μm range so that if the particles completely dense, the surface area should be around 1± 0.5 m²/g according to equation (3-1) discussed in Chapter 3. However, the core-shell heterostructures show much higher surface areas than the components. During processing, the organics in the three-dimensional TiO₂ network are gradually emitted, leaving pores between TiO₂ crystals.^{4,5} The presence of the micron-sized core BaTiO₃ improves the thermal stability of the heterostructured powders and keeps the pore from collapsing at the annealing temperature. At a sufficiently high temperature, the

pore structure will eventually collapse and dense TiO₂ will be produced. It is significant that increased thermal stability of the pore makes it possible to anneal the supported *ns*-TiO₂ to a relatively higher temperature and improve the crystallinity and interfacial bonding with only a slight loss of overall surface area.

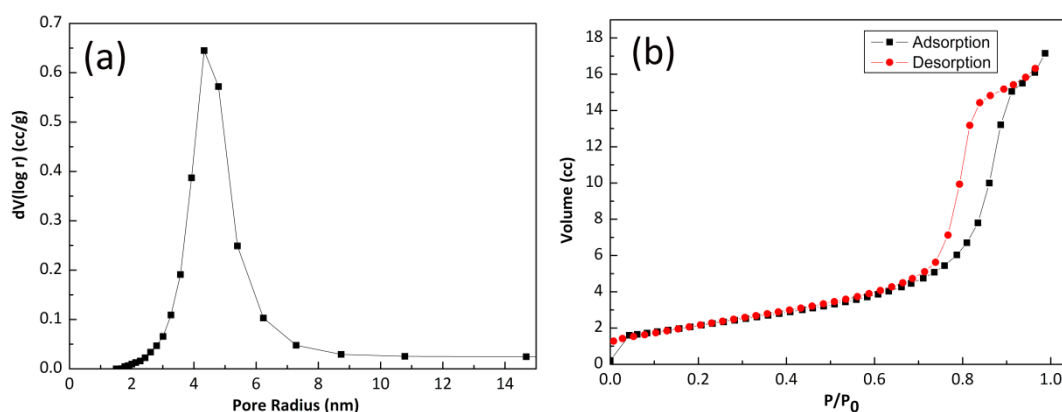


Figure 4-4 Surface area characterization of *mc*-F-BaTiO₃/*ns*-TiO₂ annealed at 600 °C: (a) pore size distribution and (b) nitrogen adsorption-desorption isothermal.

4.1.1.5 Photocatalytic Hydrogen Production

The hydrogen activities of the platinum-impregnated photocatalysts were measured under UV illumination for a range of photocatalysts in a methanol/water mixture. For consistency, a similar nominal mass of ≈ 0.4 g of catalyst was used in all experiments. Figure 4-5 shows the specific volume of H₂ (V_{H_2} in mol/m²) produced as a function of time for F-BaTiO₃/*ns*-TiO₂, C-BaTiO₃/*ns*-TiO₂, *ns*-TiO₂ powders and the *mc*-BaTiO₃ powders. The titanate and the heterostructures were annealed at 600 °C. The specific volume makes it possible to compare materials with different surface areas. The amounts of hydrogen produced per hour (R_{H_2}), the most common measure in the literature, are listed in table 4-1.

Similar to literature reports,⁶ the *mc*-BaTiO₃ did not generate detectable H₂ under UV illumination. The heterostructured F-BaTiO₃/TiO₂ powder clearly exhibits a higher activity for photolytic hydrogen production than either component alone, both in the overall volume and the average rate (slope) of production (see table 4-1). For heterostructured catalysts treated at 600 °C, the source of core material (as-received or molten salt treated) was not a significant factor. No hydrogen was detected when the experiment was repeated without illumination, which means the hydrogen production observed in the above reaction is photoinduced.

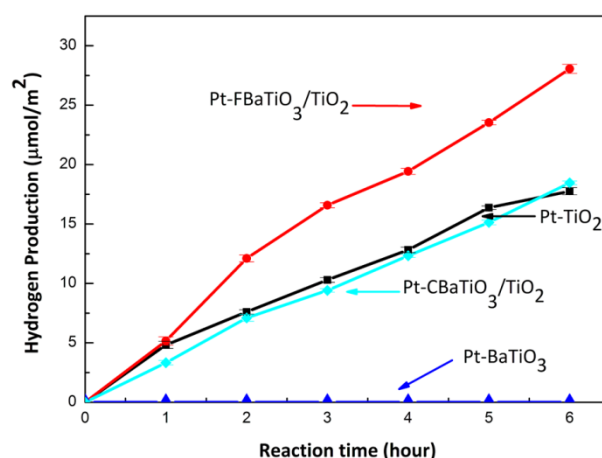


Figure 4-5 Time dependent hydrogen production per surface area from platinized BaTiO₃, TiO₂, F-BaTiO₃/TiO₂ and C-BaTiO₃/TiO₂ annealed at 600 °C.

4.1.2 BaTiO₃/TiO₂ (Sonomechanical Mixture)

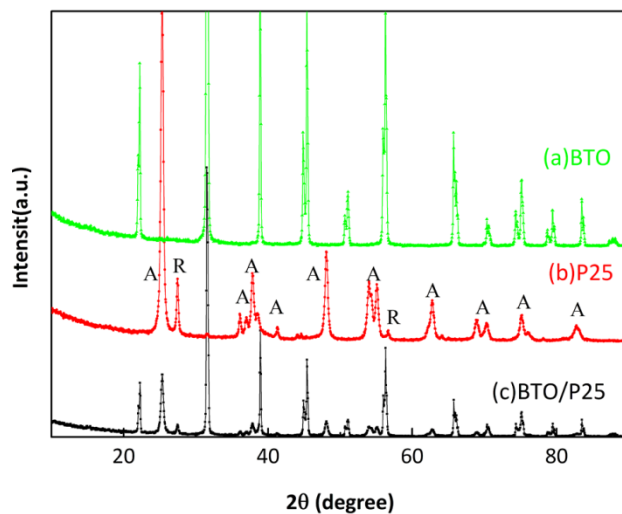


Figure 4-6 Powder x-ray diffraction patterns of platinumized (a) BaTiO₃, (b) P25 and (c) BaTiO₃/P25.

The photocatalytic properties of BaTiO₃ and TiO₂ (P25) were also measured. The XRD diffraction patterns of platinumized BaTiO₃, P25 and their sonomechanical mixture are shown in figure 4-6. Both rutile and anatase phases were observed. All diffraction peaks in the mixture of BaTiO₃ and P25 can be indexed to its components. The morphology of the mechanical mixture was investigated with SEM and shown in figure 4-7. The images show micron sized BaTiO₃ covered with small nano dots, presumably P25 nanoparticles.

The surface area and hydrogen production volume from the mechanical mixtures are shown in table 4-2 after mixing and after annealing at 500 °C. Based on the table, the addition of micronsized BaTiO₃ decreases the surface area from 49 and 45 m²/g to 28 and 12 m²/g for powders treated at room temperature and 500 °C. The values reported in table 4-2 for P25 are consistent with reported properties.⁷ The composites produce less hydrogen than the P25 by itself. This result confirms that the enhanced

photochemical properties of the core-shell composites cannot be achieved by simple mixing.

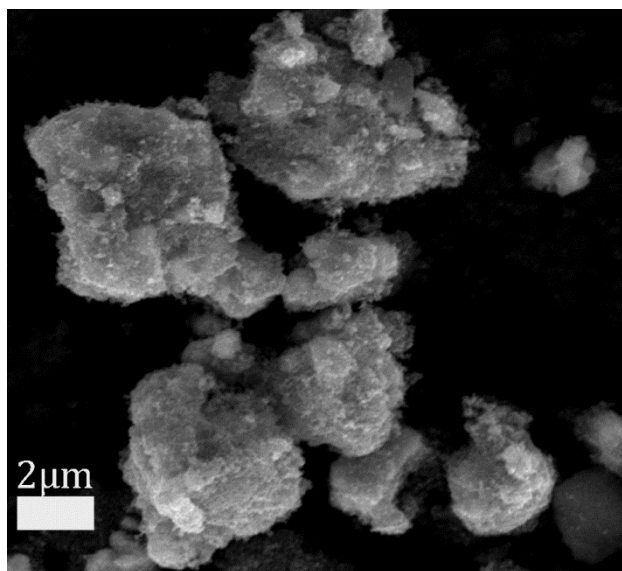


Figure 4-7 SEM images of a BaTiO₃ and P25 mechanical mixture.

Table 4-2 Summary of physical properties of a BaTiO₃/P25 mechanical mixture treated, P25, and P25 treated at 500°C.

Composition	Processing temperature (°C)	Surface area (m ² /g)	Pore volume (cc/g)	Pore radius Dv(r) (Å)	V _{H₂,6h} μmol/m ²	R _{H₂} μmol•g ⁻¹ h ⁻¹
F-BaTiO ₃ /P25	RT	28	0.17	152	12	56
F-BaTiO ₃ /P25	500	12	0.25	154	14	28
P25	RT	49	0.36	154	30	245
P25	500	45	0.42	155	24	180

4.2 Hydrogen Production from SrTiO₃/TiO₂

X-ray diffraction patterns of platinized SrTiO₃, TiO₂ and SrTiO₃/TiO₂ annealed at 500 °C are shown in figure 4-8. Similar to the pattern of BaTiO₃/TiO₂, all diffraction patterns can be indexed to anatase TiO₂ (JCPDS 46-1237), rutile TiO₂ (JCPDS 33-1381) or SrTiO₃ (JCPDS 35-734). No unexpected phases are present. The Pt co-catalyst does not produce detectable diffraction because it makes up a small fraction (~ 1 wt %) of the total sample and has a small grain size (1-5 nm).

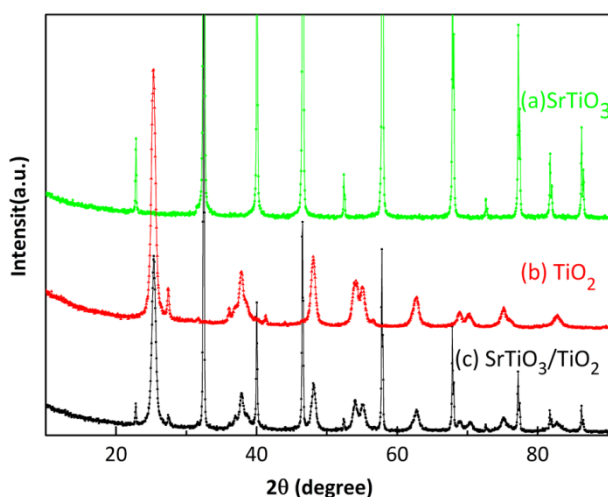


Figure 4-8 Powder x-ray diffraction patterns of platinized (a) SrTiO₃, (b) TiO₂, and (c) SrTiO₃/TiO₂ annealed at 500°C.

Figure 4-9 shows a bright field TEM image of micron-sized, faceted SrTiO₃ (*mc*-SrTiO₃) coated with nanostructured TiO₂ (*ns*-TiO₂). This figure shows that the micron-sized core is surrounded uniformly by nanostructured TiO₂ with a grain size of 10-20 nm. The high magnification TEM images in figure 4-8-(b) show that a nanostructured titania shell has formed around a SrTiO₃ core. The 40 nm TiO₂ layer is composed of faceted polycrystalline grains. The micron-sized SrTiO₃ core and the nanostructured TiO₂ coating have surface areas of 1 m²/g and 70 m²/g, respectively.

The surface area of heterostructured SrTiO₃/TiO₂ has an intermediate value (47 m²/g).

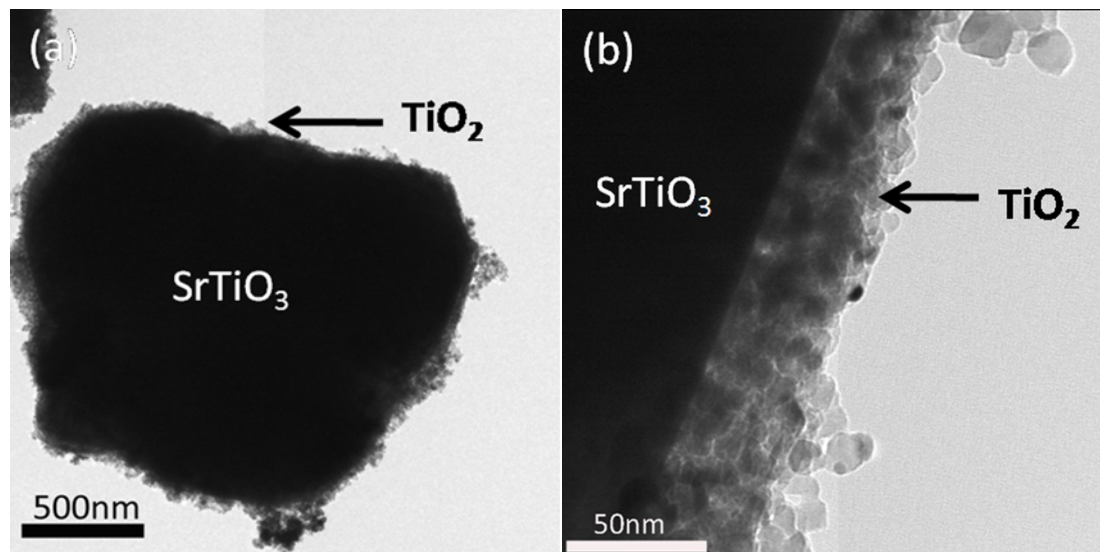


Figure 4-9 Bright field TEM images of a platinumized heterostructured particle composed of a *mc*-SrTiO₃ core and *ns*-TiO₂ shell annealed at 500 °C: (a) shows the entire particle and (b) shows a higher magnification of the coating.

Table 4-3 Surface properties of FSTO/TiO₂ annealed at 500°C, and its components.

Composition	Surface area (m ² /g)	Pore volume (cc/g)	Pore radius Dv(r) (Å)	V _{H₂,6h} μmol/m ²	R _{H₂} μmol•g ⁻¹ h ⁻¹
FSTO/TiO ₂	47	0.16	48	22	172
STO	1	0.005	20	3	0.5
TiO ₂	70	0.21	43	12	140

Figure 4-10 shows the V_{H₂} produced as a function of time for the *mc*-SrTiO₃/*ns*-TiO₂ heterostructured powders, the *mc*-SrTiO₃ powders, and the *ns*-TiO₂ powders (all annealed at 500 °C). Similar to the *mc*-BaTiO₃/*ns*-TiO₂ system, the *mc*-SrTiO₃/*ns*-TiO₂ heterostructured photocatalysts clearly exhibited a higher activity for H₂ production than either of the constituents. In nanocrystalline form, SrTiO₃ can split water to produce hydrogen^{8,9} under UV illumination, but the

microcrystalline powders do not have enough surface area to generate significant amounts of hydrogen. In addition, the hydrogen production rate was dependent on cocatalyst type and the Pt loading.^{10,11} The detailed influence of cocatalyst loading amount will be discussed in Chapter 5. Figures 4-10 indicates that the heterostructured photocatalysts annealed at 600 °C exhibit markedly improved photocatalytic properties (based on V_{H_2}) compared to either of the catalyst constituents.

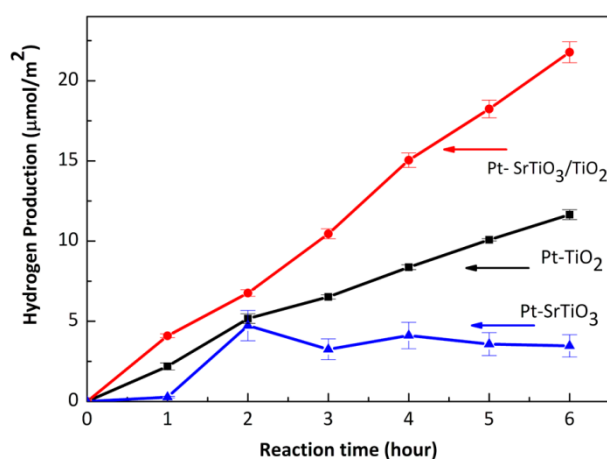


Figure 4-10 Hydrogen production from platinized SrTiO₃/TiO₂, TiO₂, and SrTiO₃ annealed at 500 °C (1 wt% Pt) in 100 mL 8 % methanol water solution.

4.3 Effect of the core

UV-vis spectroscopy was utilized to record the diffuse reflectance spectra of Pt-BaTiO₃/TiO₂ annealed at 500 °C and Pt-SrTiO₃/TiO₂ annealed at 600 °C, as shown in figure 4-11, respectively. The inset is the same spectrum focusing on the range between 350 nm and 450 nm, which is more detailed to compare the absorbance of the composite and its components.

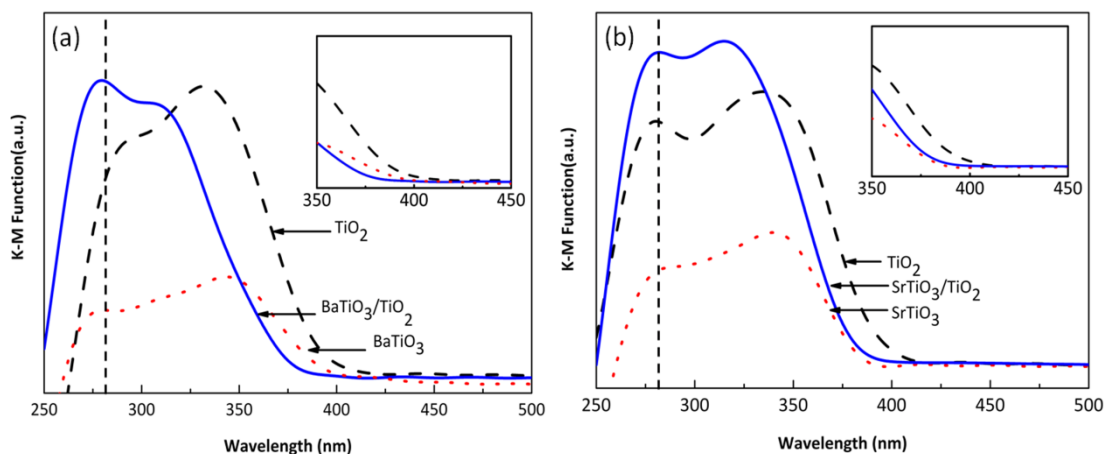


Figure 4-11 UV-vis diffuse reflectance spectra of (a) platinized BaTiO₃/TiO₂ and its components annealed at 500 °C (b) platinized SrTiO₃/TiO₂ and annealed at 600 °C.

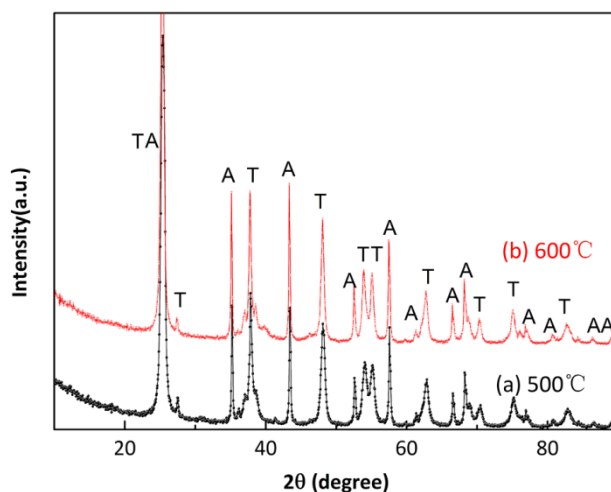


Figure 4-12 Powder x-ray diffraction patterns of Pt-Al₂O₃/TiO₂ annealed at (a) 500 °C and (b) 600 °C (A: Al₂O₃, T: TiO₂).

The reflectance spectra of the heterostructured powders are more like the core materials (BaTiO₃, SrTiO₃) than the shell (TiO₂), which means the core absorbs most of the light. The absorbance from rutile in the composites is not detected because it makes up such a small fraction of the material. This is consistent with a previous study of a heterostructured photocatalyst.¹²

To further investigate and the effect of light absorption in the core and the origin of the improved photocatalytic hydrogen production in the heterostructured powders,

micron-sized aluminum oxide (Al_2O_3) was used as the core material. Aluminum oxide has a band gap greater than 5 eV and, therefore, does not absorb the light used in this experiment.^{13,14} X-ray diffraction was performed to investigate the phase composition, as shown in figure 4-12. All diffraction peaks can be indexed to Al_2O_3 and TiO_2 . Based on the diffraction patterns, the materials do not react during preparation. Hydrogen production from those powders and its components are shown in figure 4-13. The results show that the hydrogen production rate and volume of evolved gas from $\text{Al}_2\text{O}_3/\text{TiO}_2$ are almost the same as TiO_2 alone. Platinized Al_2O_3 powder did not produce hydrogen, which is consistent with the previous research.^{15,16} However, it was reported that composite $\text{Al}_2\text{O}_3\text{-TiO}_2$ nanoparticles show an enhanced photocatalytic activity for hydrogen production and dye degradation because photogenerated charge carrier recombination is retarded by the presence of Al_2O_3 nanoparticles.^{15,17} In our experiment, the micron-sized Al_2O_3 coated with nanostructured TiO_2 shell did not exhibit improved photocatalytic activity for hydrogen production compared with its components.

Another control experiment was designed to investigate the influence of the core size on the photocatalytic activity of the heterostructure. A commercial BaTiO_3 nanoparticle were used as the core material and then coated with TiO_2 using the same procedure that was used to make the $mc\text{-BaTiO}_3/ns\text{-TiO}_2$. The surface area and pore morphology data are listed in table 4-4. The pore size distribution of $mc\text{-BaTiO}_3/ns\text{-TiO}_2$ and $ns\text{-BaTiO}_3/ns\text{-TiO}_2$ annealed at 500 °C was shown in figure 4-14. The surface area of $ns\text{-BaTiO}_3/ns\text{-TiO}_2$ is 84 m^2/g , which is larger than the value

of $61 \text{ m}^2/\text{g}$ for $mc\text{-BaTiO}_3/ns\text{-TiO}_2$. Besides the surface area, other pore morphologies parameters did not change greatly. The mean pore radius of $ns\text{-BaTiO}_3/ns\text{-TiO}_2$ ($\approx 4 \text{ nm}$) is a little lower than that of $mc\text{-BaTiO}_3/ns\text{-TiO}_2$ ($\approx 5 \text{ nm}$). This may be because micron-sized core provides a better support to the mesoporous structure than nano-sized core. The thermal stability of the pores is greared in the $mc\text{-BaTiO}_3/ns\text{-TiO}_2$ heterostructure. Figure 4-14 shows these two photocatalysts had similar pore size distributions and both of them are mesoporous. The surface area of the $ns\text{-BaTiO}_3$ is about ten times greater than the $mc\text{-BaTiO}_3$.

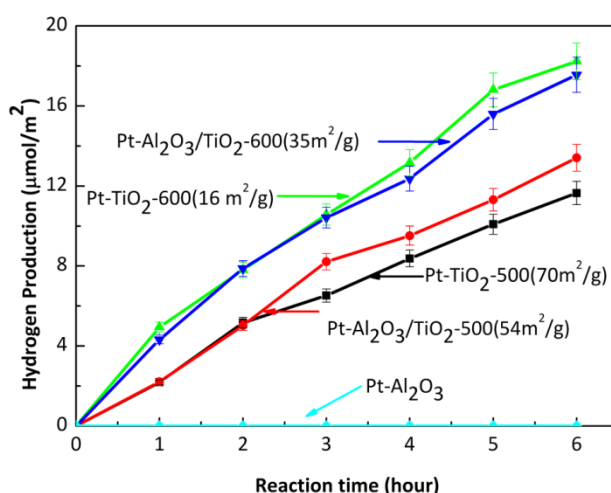


Figure 4-13 Hydrogen production from platinumized $\text{Al}_2\text{O}_3/\text{TiO}_2$ and its components annealed at $500 \text{ }^\circ\text{C}$ and $600 \text{ }^\circ\text{C}$ as well as BET surface area (-500, -600 represents the powders annealed at $500 \text{ }^\circ\text{C}$ and $600 \text{ }^\circ\text{C}$).

The rate of photocatalytic hydrogen production is shown in table 4-4 and figure 4-15. All of the photocatalyst were loaded with 1 wt% platinum. Based on these data, the hydrogen production rate from $mc\text{-BaTiO}_3/ns\text{-TiO}_2$ ($132 \text{ } \mu\text{mol}\cdot\text{g}^{-1}\text{h}^{-1}$) is about 2.4 times that from $ns\text{-BaTiO}_3/ns\text{-TiO}_2$ ($56 \text{ } \mu\text{mol}\cdot\text{g}^{-1}\text{h}^{-1}$). When the surface area is accounted for, $mc\text{-BaTiO}_3/ns\text{-TiO}_2$ produces $13 \text{ } \mu\text{mol}/\text{m}^2$ or about 3.3 times that produced by $ns\text{-BaTiO}_3/ns\text{-TiO}_2$ ($4 \text{ } \mu\text{mol}/\text{m}^2$). Therefore, $mc\text{-BaTiO}_3/ns\text{-TiO}_2$

produced more hydrogen at a higher rate than *ns*-BaTiO₃/*ns*-TiO₂, even though *mc*-BaTiO₃/*ns*-TiO₂ has smaller surface area. No hydrogen was produced by *mc*-BaTiO₃ or *ns*-BaTiO₃.

Table 4-4 Physical properties of *mc*-BaTiO₃/*ns*-TiO₂ and *ns*-BaTiO₃/*ns*-TiO₂ annealed at 500°C, as well as their components.

Composition	Surface area (m ² /g)	Pore volume (cc/g)	Pore radius D _v (r) (Å)	V _{H₂,6h} μmol/m ²	R _{H₂} μmol•g ⁻¹ h ⁻¹
<i>mc</i> -BaTiO ₃ / <i>ns</i> -TiO ₂	61	0.2	48	13	132
<i>ns</i> -BaTiO ₃ / <i>ns</i> -TiO ₂	84	0.19	39	4	56
<i>mc</i> -BaTiO ₃	0.8	0.003	16	0	0
<i>ns</i> -BaTiO ₃	9	0.04	19	0	0

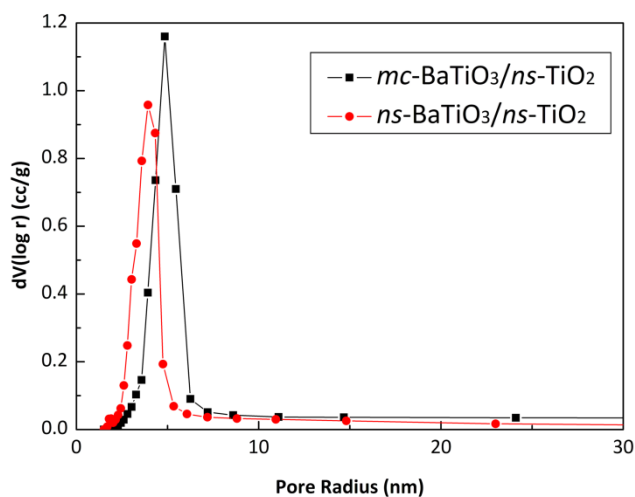


Figure 4-14 Pore size distribution of *mc*-BaTiO₃/*ns*-TiO₂ and *ns*-BaTiO₃/*ns*-TiO₂ annealed at 500 °C.

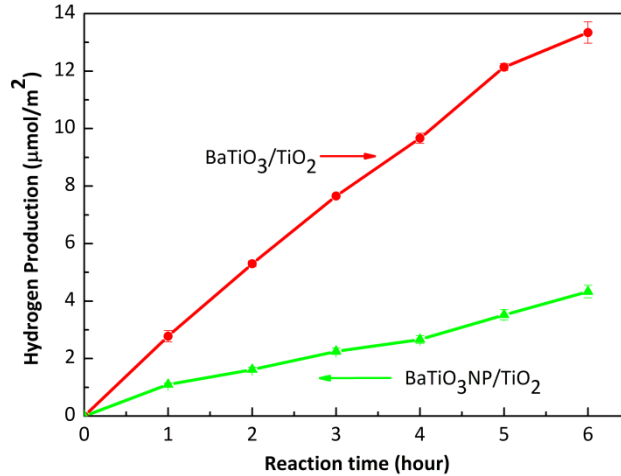


Figure 4-15 Hydrogen production from platinized *mc*-BaTiO₃/*ns*-TiO₂ and *ns*-BaTiO₃/*ns*-TiO₂ annealed at 500 °C.

4.4 Discussion

The most important observation in the previous experiments is that micron-sized (Ba, Sr)TiO₃ coated with nanostructured TiO₂ annealed at 600 °C and 500 °C, respectively, exhibits enhanced photocatalytic activity for hydrogen production compared to the components. To understand the reasons for these observations, schematic energy level diagrams of heterostructured BaTiO₃/TiO₂ are shown in figure 4-15. The simplified schematics were generated with a number of assumptions. The conduction band positions of BaTiO₃ and TiO₂ are assumed to be the same. It is reported that the flat band potential of BaTiO₃ is 0.05 V more negative than rutile.¹⁸ As discussed before, the flat band potential of anatase is reported to be 0.2 V more negative than rutile.¹⁹ Therefore, the difference of the flat band potential between BaTiO₃ and TiO₂ is small. The band gaps of anatase and rutile are 3.2 eV and 3.0 eV.²⁰⁻²² The bandgap of BaTiO₃ was reported to be 3.2 eV.^{23,24} The differences in the band gap for these three materials should be no more than 0.2 eV and thus the band

gaps of BaTiO₃ and TiO₂ are assumed to be the same. For an n-type semiconductor, the Fermi level is located at 0.1 eV below the conduction band if the donor state is considered to be 0.2 eV below the conduction band.^{25,26} The work function of TiO₂, which is the energy difference between the vacuum and Fermi level, is reported to be 4.2 eV.²⁷ TiO₂ has band bending at the interface contacting with the solution, which is represented as a surface potential (V_s). The flat Fermi level indicates that the system is in equilibrium. The redox potential difference between H₂/H⁺ and O₂/O⁻ is 1.23 V.²⁸

Figure 4-16 shows the situations for BaTiO₃/TiO₂ heterostructures with two different polarizations. When the coating is thinner than the depletion layer, the space charge region of the nanostructured coating cannot be relaxed to that of the bulk,²⁹ as shown in (a) and (b). In general, the thickness of the depletion layer should be about 100 nm.²⁹ The primary phase in the TiO₂ coating should be anatase and the X-ray suggests that the anatase makes up less than 10 % of the titania. The absorption coefficients for anatase and rutile are $2 \times 10^3/\text{cm}$ and $1 \times 10^5/\text{cm}$, respectively.^{30,31} The absorption coefficient of BaTiO₃ is similar to rutile.³¹ Therefore, a 50 nm thick anatase (rutile) film can absorb 1% (40%) of the photons and a 100 nm thick film can absorb 2% (67%) of the photons. Considering this, BaTiO₃ is the phase that absorbs most of the light. In addition, the observation that the heterostructured ceramics consisting of a non-absorbing Al₂O₃ core and a nanostructured TiO₂ coating have nearly the same photocatalytic activity as TiO₂ alone strengthens the argument that carriers created in the core contribute the reactivity of BaTiO₃/TiO₂ catalysts.

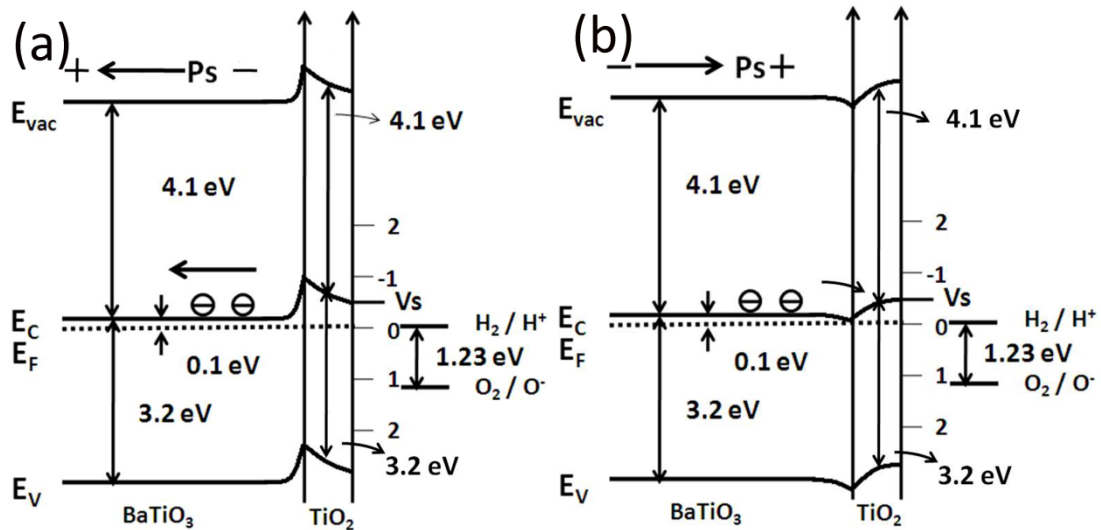


Figure 4-16 A highly simplified schematic representation of band structure diagram of heterostructured BaTiO₃/TiO₂ for (a) and (b) thin coating with different polarization directions. (E_{vac} , E_c , E_f and E_v represent the edge for vacuum level, conduction band, Fermi level and valance band, respectively. P_s refers to spontaneous polarization from ferroelectrics. The hydrogen and oxygen redox level are shown in the right.)

The polarization from the ferroelectric is also shown in the schematic. The direction towards the interface between BaTiO₃ and TiO₂ is designated as positive and away from the interface is negative. As discussed in Chapter 2, ferroelectric crystals can be divided into domains with different polarization directions. At the surfaces of positively polarized domains, the electron energy levels will bend downward and the opposite occurs in negative domains. When heterostructured BaTiO₃/TiO₂ is illuminated by photons with energies larger than the band gap of components, electrons are excited to the conduction band. With positive polarization, electrons will move towards the interface of the two solids, as shown in (b). To pass through the titania, the electrons will have to have enough energy to surmount the barrier. From previous research, the domains in bare BaTiO₃ with positive polarization promote reduction.^{31,32} The previous results for heterostructured BaTiO₃ coated with TiO₂ show the same domain in BaTiO₃ with and without the TiO₂ coating has the same

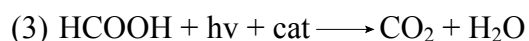
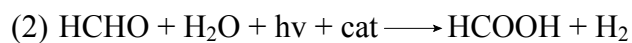
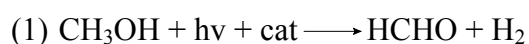
reaction.^{31,32} Therefore, this observation implies photogenerated charge carriers generated from the core can overcome the energy barrier in the interface and reach the surface of the coating to participate in the redox reaction. In addition, some electrons can be directly excited to states above the barrier and transport to the TiO₂ coating.³³ Electrons also can be transported to the coating surface by tunneling through the coating.^{31,32} It is also possible that the dipolar fields from the substrate can separate electrons and holes in the coating to increase the reactivity. These factors might explain why heterostructured BaTiO₃/TiO₂ displays enhanced photocatalytic activity compared to the separate phases.

The use of a microcrystalline core is important because the spontaneous polarization of ferroelectrics is significantly dependent on particle size; it decreases substantially in the nanoscale range.³⁴⁻³⁶ Also, the small size of nanoparticles does not permit significant band bending in uniform particles.³⁷ Both of these two factors will lead to the increase of photogenerated charge carrier recombination. This may explain why the *ns*-BaTiO₃/*ns*-TiO₂ exhibits lower photocatalytic reactivity for hydrogen production than *mc*-BaTiO₃/*ns*-TiO₂.

Heterostructured catalysts with non-ferroelectric SrTiO₃ cores have reactivities that are similar to those with BaTiO₃ cores. The conduction band position of SrTiO₃ is reported to be 0.2 eV higher than TiO₂.³⁸ The bandgap of SrTiO₃ is reported to be 3.2 eV.²³ Because of the similarities of BaTiO₃ and SrTiO₃, the schematics in figure 4-16 can all be used to represent the SrTiO₃/TiO₂ heterostructures. As discussed in Chapter 2, the surface layer termination of SrTiO₃ can be polar. The dipolar fields arise from

charged surface domains. This may contribute to the improved photocatalytic activity of heterostructured SrTiO₃/TiO₂. The enhanced photocatalytic activity of heterostructured SrTiO₃/TiO₂ nanofibers and nanotubes, has also been reported.³⁹⁻⁴⁴ The enhanced reactivity was attributed to electron transfer from SrTiO₃ to TiO₂.³⁹ The lower electron affinity and higher isoelectric point of SrTiO₃ compared to TiO₂ may lead to a potential step at the interface between them, which resembles a dipolar layer shuttling carriers towards the TiO₂ shell.^{43,44} This dipolar layer will shift the conduction band of TiO₂ to a negative position without the formation of an energy barrier at the interface.^{43,44} Those explanations for nanocomposites are consistent with our description based on the band structure diagram.

No carbon dioxide was observed to evolve from the solution. As discussed previously, methanol is a sacrificial reagent to scavenge the photogenerated holes to assist the separation of charge carriers. Therefore, carbon dioxide rather than oxygen is the oxidation product. The processes are shown as equation (1-3).^{45,46}



Carbon dioxide should be detected in the gas phase. However, it is reported that carbon dioxide produced from the above reaction will be dissolved into water, which acidifies the solution.¹¹ This is consistent with our observation.

4.5 Summary

In this chapter, photocatalytic hydrogen production from heterostructured (Ba,Sr)TiO₃ coated with a nanostructured TiO₂ shell was measured and the structural and physical properties of these materials were also determined. A sonomechanical mixture of BaTiO₃ and TiO₂ was utilized as a control experiment to investigate the effect of the interface between the core and the shell. Al₂O₃/TiO₂ core-shell structures were studied as another control to test the effect of a core that does not absorb light. A *ns*-BaTiO₃/*ns*-TiO₂ heterostructure, prepared in the same way as *mc*-BaTiO₃/*ns*-TiO₂, shows lower photocatalytic reactivity for hydrogen production. The results obtained from this chapter can be summarized as follows:

1. Micron-sized ferroelectric BaTiO₃ coated with nanostructured TiO₂ exhibits enhanced photocatalytic activity for hydrogen production under UV-visible irradiation compared to the component materials.
2. The nonferroelectric SrTiO₃ core/TiO₂ shell heterostructured powders annealed at 500 °C shows a similar enhancement of photocatalytic hydrogen production.
3. Sonomechanical mixtures of BaTiO₃ and TiO₂ (P25) do not display the improved reactivity.
4. Optical characterization of (Ba,Sr)TiO₃/TiO₂ shows that diffuse reflectance spectra of heterostructured powders are similar to that of the micron-sized core.
5. The *mc*-Al₂O₃/*ns*-TiO₂ heterostructured powder does not show improved photocatalytic activity for hydrogen production.
6. The *mc*-BaTiO₃/*ns*-TiO₂ heterostructure produces more hydrogen than

ns-BaTiO₃/*ns*-TiO₂ under the same conditions.

4.6 References

- (1) Sclafani, A.; Herrmann, J. M. *The Journal of Physical Chemistry* **1996**, *100*, 13655.
- (2) Hurum, D. C.; Agrios, A. G.; Gray, K. A.; Rajh, T.; Thurnauer, M. C. *The Journal of Physical Chemistry B* **2003**, *107*, 4545.
- (3) Fernandes Machado, N. R. C.; Santana, V. S. *Catalysis Today* **2005**, *107-108*, 595.
- (4) Carp, O.; Huisman, C. L.; Reller, A. *Progress in Solid State Chemistry* **2004**, *32*, 33.
- (5) Huang, H. J.; Li, D. Z.; Lin, Q.; Shao, Y.; Chen, W.; Hu, Y.; Chen, Y. B.; Fu, X. Z. *The Journal of Physical Chemistry C* **2009**, *113*, 14264.
- (6) Yamashita, Y.; Tada, M.; Kakihana, M.; Osada, M.; Yoshida, K. *Journal of Materials Chemistry* **2002**, *12*, 1782.
- (7) Ohno, T.; Sarukawa, K.; Tokieda, K.; Matsumura, M. *Journal of Catalysis* **2001**, *203*, 82.
- (8) Yamaguti, K.; Sato, S. *Journal of the Chemical Society-Faraday Transactions I* **1985**, *81*, 1237.
- (9) Ishii, T.; Kato, H.; Kudo, A. *Journal of Photochemistry and Photobiology A-Chemistry* **2004**, *163*, 181.
- (10) Domen, K.; Kudo, A.; Onishi, T.; Kosugi, N.; Kuroda, H. *The Journal of Physical Chemistry* **1986**, *90*, 292.
- (11) Puangpetch, T.; Sreethawong, T.; Chavadej, S. *International Journal of Hydrogen Energy* **2010**, *35*, 6531.
- (12) Gao, B.; Kim, Y. J.; Chakraborty, A. K.; Lee, W. I. *Appl. Catal. B-Environ.* **2008**, *83*, 202.
- (13) Ching, W. Y.; Xu, Y.-N. *Journal of the American Ceramic Society* **1994**, *77*, 404.
- (14) Xuan, Y.; Lin, H. C.; Ye, P. D.; Wilk, G. D. *Applied Physics Letters* **2006**, *88*, 263518.
- (15) Kim, W.; Tachikawa, T.; Majima, T.; Choi, W. *The Journal of Physical Chemistry C* **2009**, *113*, 10603.
- (16) Blake, D. M. "Bibliography of Work on the Heterogeneous Photocatalytic Removal of Hazardous Compounds from Water and Air," National Renewable Energy Laboratory, 2001.
- (17) Anderson, C.; Bard, A. J. *The Journal of Physical Chemistry B* **1997**, *101*, 2611.
- (18) Kung, H. H.; Jarrett, H. S.; Sleight, A. W.; Ferretti, A. *Journal of Applied Physics* **1977**, *48*, 2463.
- (19) Kavan, L.; Grätzel, M.; Gilbert, S. E.; Klemenz, C.; Scheel, H. J. *Journal of the American Chemical Society* **1996**, *118*, 6716.
- (20) Chen, X.; Mao, S. S. *Chemical Reviews* **2007**, *107*, 2891.
- (21) Grant, F. A. *Reviews of Modern Physics* **1959**, *31*, 646.
- (22) Pascual, J.; Camassel, J.; Mathieu, H. *Physical Review B* **1978**, *18*, 5606.
- (23) Cardona, M. *Physical Review* **1965**, *140*, A651.
- (24) Casella, R. C.; Keller, S. P. *Physical Review* **1959**, *116*, 1469.

- (25) Breckenridge, R. G.; Hosler, W. R. *Physical Review* **1953**, *91*, 793.
- (26) Berglund, C. N.; Braun, H. J. *Physical Review* **1967**, *164*, 790.
- (27) Imanishi, A.; Tsuji, E.; Nakato, Y. *The Journal of Physical Chemistry C* **2007**, *111*, 2128.
- (28) Morrison, S. R. *Electrochemistry at semiconductor and oxidized metal electrodes*; Plenum Press: New York, 1980.
- (29) Albery, W. J.; Philip, N. B. *Journal of The Electrochemical Society* **1984**, *131*, 315.
- (30) Park, Y. R.; Kim, K. J. *Thin Solid Films* **2005**, *484*, 34.
- (31) Burbure, N. V.; Salvador, P. A.; Rohrer, G. S. *Chemistry of Materials* **2010**, *22*, 5823.
- (32) Burbure, N. V.; Salvador, P. A.; Rohrer, G. S. *Chemistry of Materials* **2010**, *22*, 5831.
- (33) Zhang, X.; Zhang, L.; Xie, T.; Wang, D. *The Journal of Physical Chemistry C* **2009**, *113*, 7371.
- (34) Li, X. P.; Shih, W. H. *Journal of the American Ceramic Society* **1997**, *80*, 2844.
- (35) Akdogan, E. K.; Rawn, C. J.; Porter, W. D.; Payzant, E. A.; Safari, A. *Journal of Applied Physics* **2005**, *97*.
- (36) Asiaie, R.; Zhu, W.; Akbar, S. A.; Dutta, P. K. *Chemistry of Materials* **1996**, *8*, 226.
- (37) Kavan, L.; Gratzel, M.; Gilbert, S. E.; Klemenz, C.; Scheel, H. J. *Journal of the American Chemical Society* **1996**, *118*, 6716.
- (38) Bolts, J. M.; Wrighton, M. S. *The Journal of Physical Chemistry* **1976**, *80*, 2641.
- (39) Cao, T. P.; Li, Y. J.; Wang, C. H.; Shao, C. L.; Liu, Y. C. *Langmuir* **2011**, *27*, 2946.
- (40) Zhang, X. M.; Huo, K. F.; Hu, L. S.; Wu, Z. W.; Chu, P. K. *Journal of the American Ceramic Society* **2010**, *93*, 2771.
- (41) Yan, J. H.; Zhu, Y. R.; Tang, Y. G.; Zheng, S. Q. *Journal of Alloys and Compounds* **2009**, *472*, 429.
- (42) Zhang, J.; Bang, J. H.; Tang, C. C.; Kamat, P. V. *ACS Nano* **2010**, *4*, 387.
- (43) Diamant, Y.; Chen, S. G.; Melamed, O.; Zaban, A. *The Journal of Physical Chemistry B* **2003**, *107*, 1977.
- (44) Diamant, Y.; Chappel, S.; Chen, S. G.; Melamed, O.; Zaban, A. *Coordination Chemistry Reviews* **2004**, *248*, 1271.
- (45) Kawai, T.; Sakata, T. *Journal of the Chemical Society, Chemical Communications* **1980**, 694.
- (46) Wu, N. L.; Lee, M. S.; Pon, Z. J.; Hsu, J. Z. *Journal of Photochemistry and Photobiology A-Chemistry* **2004**, *163*, 277.

5. Effect of Geometric, Compositional, and Processing Parameters on Photocatalytic Properties of Heterostructured Powders

As introduced in Chapter 4, (Ba,Sr)TiO₃/TiO₂ heterostructured powders show improved photocatalytic activity for hydrogen production when compared with their individual components. In this chapter, the effects that different parameters related to the fabrication of the powders have on the photocatalytic activity of (Ba,Sr)TiO₃ heterostructures will be discussed. The core composition, the annealing temperature, the amount of Pt loading, and certain geometric features, specifically the thickness of the shell, will be investigated and optimized for hydrogen production. The optimization data can provide design guidance for heterostructured core-shell photocatalysts.

5.1 Effect of Annealing Temperature

Annealing temperature is one of most important processing parameters in the sol-gel method because it determines the crystallinity and structure of the final product, and therefore the catalytic properties. The influence of annealing temperature on the phase of the coating, surface area, pore structure, coating thickness, and photocatalytic activity for hydrogen production, will be discussed later.

5.2 Phase and Grain Size

The structure of platinized TiO₂ annealed at different temperatures was analyzed by XRD to investigate how phase composition changes with increasing temperature. The XRD patterns of sol-gel fabricated TiO₂ (see Chapter 3) annealed at 400, 500, and 600 °C are shown in figure 5-1. The ratio of intensities of peaks relating to rutile, denoted as R, to those relating to anatase, denoted as A, increases with elevated annealing temperatures. The decreased quantity of anatase and increased quantity of rutile at high temperatures is expected.^{1,2} In the literature, anatase is reported to convert to rutile at a temperature between 500 and 600 °C.^{3,4}

The x-ray diffraction patterns of platinized BaTiO₃/TiO₂, SrTiO₃/TiO₂ and TiO₂ annealed at 700 °C are shown in figure 5-2. The primary phase in the TiO₂ powder annealed at 700 °C is rutile. A few small peaks can be indexed as anatase. However, the primary phase for the TiO₂ shells in the BaTiO₃/TiO₂ and SrTiO₃/TiO₂ powders annealed at 700 °C is anatase. This result confirms that, in our designed microcrystalline core/nanostructured shell heterostructure, the core materials can stabilize anatase in the nanostructured coating. This support effect should be beneficial to performance, since anatase is reported to show higher photocatalytic activity than rutile.⁵ The core makes it possible to be used at higher processing temperatures, which favors crystallization, while avoiding the conversion from anatase to rutile.

The ratio between anatase and rutile can be calculated using the following equation (assuming randomly oriented crystallites):⁶

$$R \% = \frac{1}{1.265 \times \frac{I_A}{I_R}},$$

where R% is the percentage of rutile, I_A is the intensity of the anatase (101) peak, and I_R is the intensity of the rutile (110) peak, respectively. (TiO_2 is assumed to be composed of only anatase and rutile). The crystallite size of anatase was determined with Scherrer's equation:⁷

$$L = \frac{K\lambda}{\beta \cos\theta},$$

where L is the crystallite size, K is a constant taken as 0.94, λ is the wavelength of X-ray radiation, β is the line width at half maximum height, and θ is the angle of incidence or reflection.

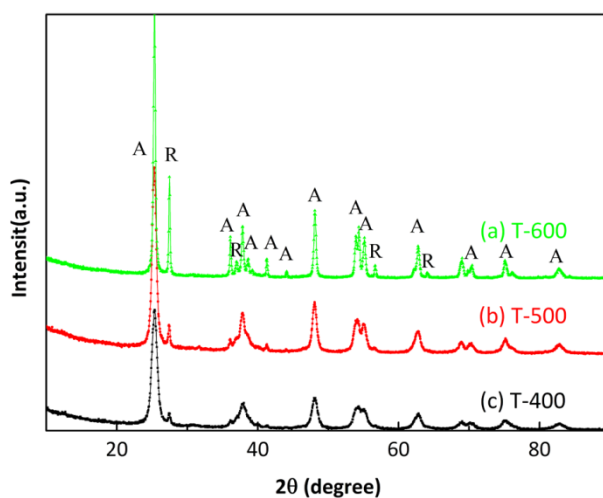


Figure 5-1 Comparison of powder x-ray diffraction patterns of platinumized TiO_2 annealed at 400-600 °C. (T-400 represents TiO_2 annealed at 400 °C, etc; A and R refer to anatase and rutile.)

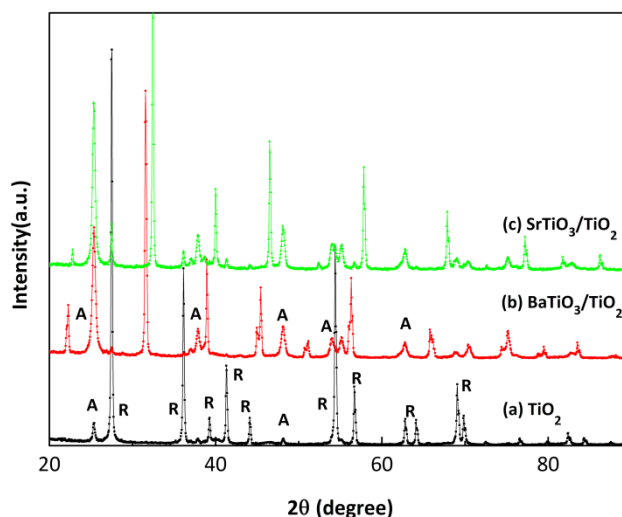


Figure 5-2 Comparison of powder x-ray diffraction patterns of platinized BaTiO₃/TiO₂, SrTiO₃/TiO₂, and TiO₂ annealed at 700 °C. (A and R refer to anatase and rutile.)

Table 5-1 The phase composition and TiO₂ grain sizes of BaTiO₃/TiO₂, SrTiO₃/TiO₂, and TiO₂ annealed at different temperatures.

Catalyst	Annealing temperature	Anatase Percentage	TiO ₂ Grain Size
	(°C)	(%)	(nm)
TiO ₂	400	91.6	10(A)
	500	89.9	13(A)
	600	77.5	27(A)
	700	5.6	48(R)
	800	0.4	50(R)
BaTiO ₃ /TiO ₂	400	93.6	10(A)
	500	93.3	12(A)
	600	93.6	14(A)
	700	95.7	20(A)
	800	66.5	25(A) 40(R)
SrTiO ₃ /TiO ₂	500	93.6	14(A)
	600	91.7	17(A)
	700	82.4	22(A)
	800	57.7	32(A) 44(R)
	900	2.8	50(R)

The results of the XRD experiments to determine the influence of annealing temperature on the phase composition and TiO₂ grain size are shown in table 5-1.

TiO₂ and BaTiO₃/TiO₂ heterostructures were annealed from 400 °C to 800 °C, while

SrTiO₃/TiO₂ was annealed from 500 °C to 900 °C. The conversion of anatase to rutile starts at 500 °C to 600 °C. This is consistent with the previous reports.^{3,4} This transformation is almost complete at 800 °C. The transformation of anatase to rutile in the (Ba,Sr)TiO₃/TiO₂ occurs at 700 °C to 800 °C. After annealing at 800 °C, the heterostructures are still half anatase. The transformation of anatase in the coatings is completed at 900 °C; 97 % of the TiO₂ phase in SrTiO₃/TiO₂ is rutile. From 500 to 800 °C, TiO₂ in BaTiO₃/TiO₂ heterostructure has slightly more anatase than that in the SrTiO₃/TiO₂ heterostructure, suggesting BaTiO₃ cores hindered the phase transformation to rutile slightly better than SrTiO₃ cores. However, the differences are relatively small.

In table 5-1, the grain sizes determined from XRD for the primary phase of the TiO₂ powders is given, except for the heterostructure annealed at 800 °C, for which the value of both phases is given. The anatase in the TiO₂ coating in the heterostructure shows a smaller grain size (25 nm in BaTiO₃/TiO₂ and 32 nm in SrTiO₃/TiO₂) than for the rutile (40 nm in BaTiO₃/TiO₂ and 44 nm in SrTiO₃/TiO₂), when the powders were annealed at the same temperature (800 °C). In the literature, rutile is reported to show a larger grain size than anatase when annealed at the same temperature.⁵ Therefore, it is not straightforward to compare the grain size of anatase and rutile at the different temperatures, without measurement. Nevertheless, the grain size of both anatase and rutile increased with an increase in the annealing temperature (as expected from thermal coarsening). The crystallite size of anatase in the TiO₂ increased from 10 nm to 27 nm when the annealing temperature increased from

400 °C to 600 °C. The crystallite size of rutile increased only slightly, from 48 nm to 50 nm, when the annealing temperature increased from 700 °C to 800 °C.

The crystallite sizes of both anatase and rutile in the (Ba,Sr)TiO₃/TiO₂ heterostructures are smaller than those in the TiO₂ powders, indicating the interaction with the core hinders crystallite size increases by thermal coarsening in the nanostructured coatings. This support effect is not obvious when the powders were annealed at low temperature. The sizes of anatase in TiO₂ and BaTiO₃/TiO₂ are the same (10 nm) when annealed at 400 °C. Thermal coarsening has little effect on the size of TiO₂ grains at 400 °C and 500 °C. Thermal coarsening is enhanced greatly from 600 °C and the size of anatase increases by nearly a factor of two. After 600 °C, the anatase transforms to rutile and the structure of TiO₂ is dense. Comparing the grain sizes of TiO₂ in BaTiO₃/TiO₂ and SrTiO₃/TiO₂ heterostructures, we notice that BaTiO₃ stabilizes the grain size better than SrTiO₃. The grain size of TiO₂ in BaTiO₃/TiO₂ is smaller than that in SrTiO₃/TiO₂ annealed at the same temperature.

5.2.1 Morphology

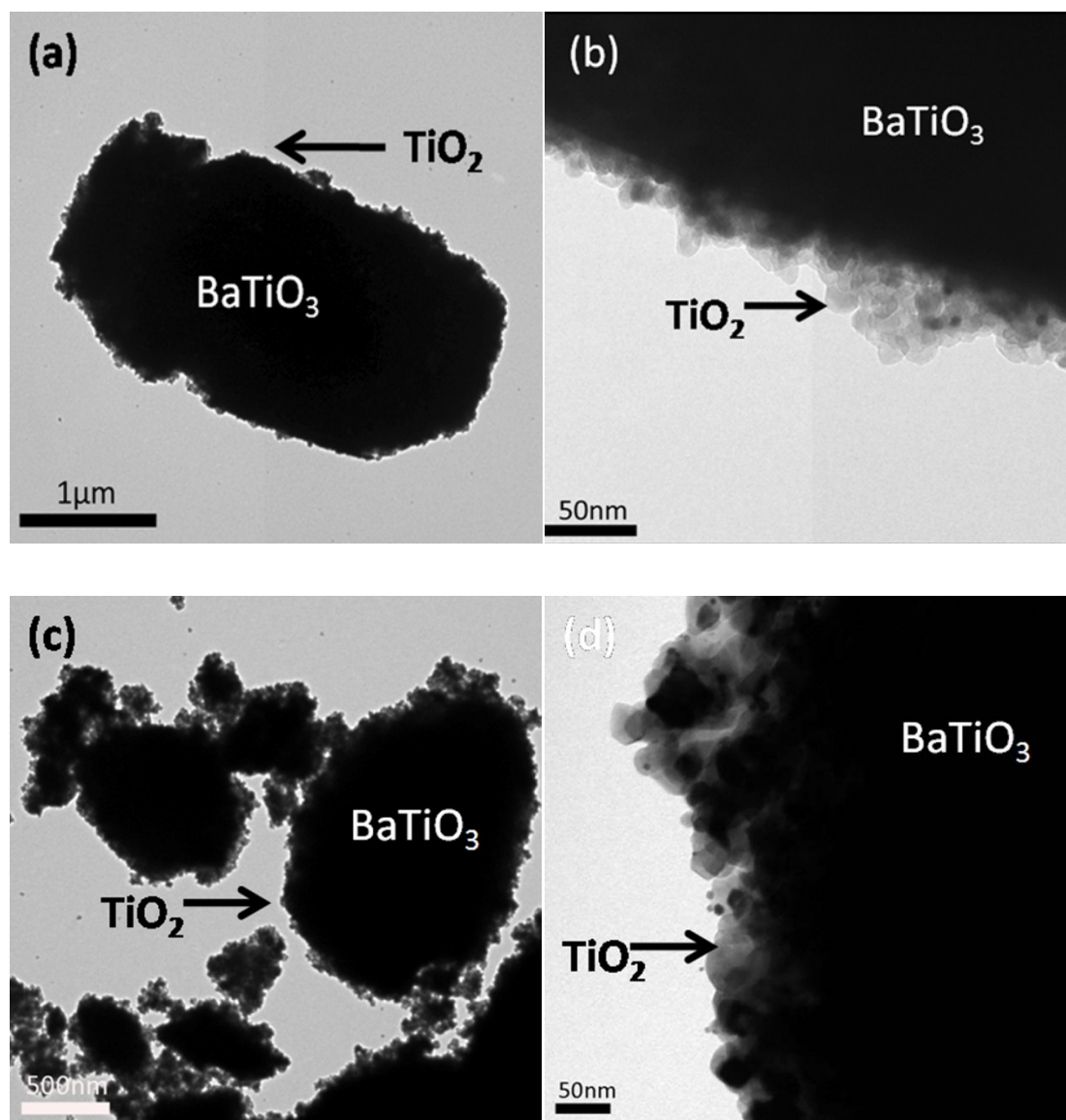


Figure 5-3 Bright field TEM images of a platinumized heterostructured particle composed of a *mc*- BaTiO_3 core and *ns*- TiO_2 shell annealed at $400\text{ }^\circ\text{C}$: (a) shows the entire particle, (b) shows a higher magnification of the coating, $500\text{ }^\circ\text{C}$: (c) shows the entire particles, and (d) shows a higher magnification of the coating.

The bright field TEM images of platinumized $\text{BaTiO}_3/\text{TiO}_2$ core-shell particles annealed at $400\text{ }^\circ\text{C}$ and $500\text{ }^\circ\text{C}$ are shown in figure 5-3. Compared with figure 4-3 (a similar coating annealed at $600\text{ }^\circ\text{C}$), the difference in particle size of nanostructured TiO_2 can be observed clearly. The particle sizes of TiO_2 in the coating increased from

10-15 nm (400 °C) to 15-35 nm (500 °C) to 20-40 nm (600 °C). It confirms that high annealing temperature causes coarsening in the titania coating. Bright field TEM images of platinumized SrTiO₃/TiO₂ heterostructure annealed at 800 °C, at different magnifications, are shown in figure 5-4. The interface between nanostructured TiO₂ coating and micron-sized SrTiO₃ core is marked with the white boundary line. From this image, the thermal coarsening of TiO₂ is clear and obvious. The particle size of TiO₂ ranges from 50 nm to 80 nm. This is consistent with the result from XRD. With increased particle size, the coating is expected to also be much denser.

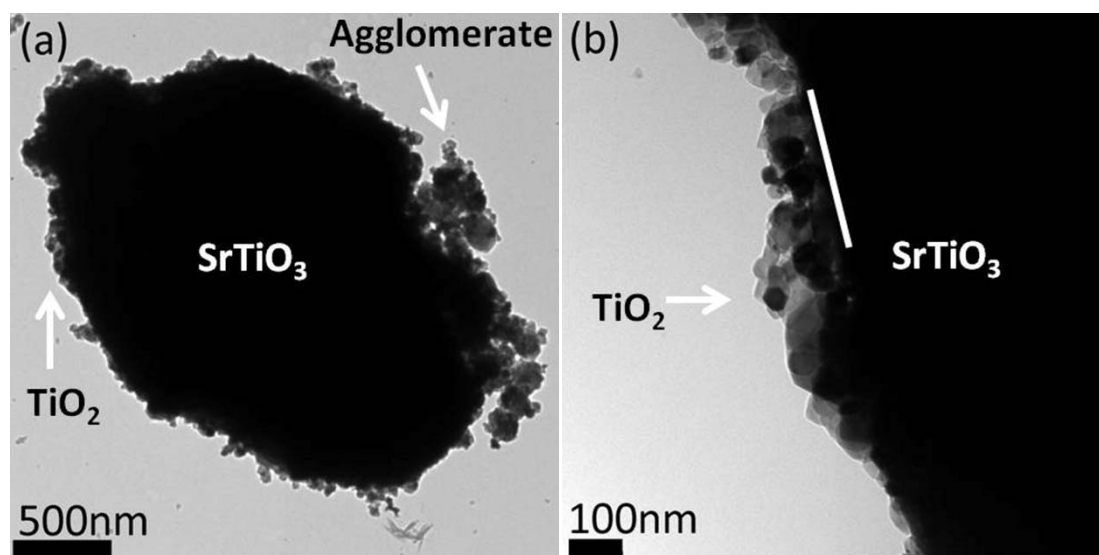


Figure 5-4 Bright field TEM images of a platinumized heterostructured particle composed of a *mc*-SrTiO₃ core and a *ns*-TiO₂ shell annealed at 800 °C: (a) shows the entire particle and (b) shows a higher magnification image of the coating.

For all heterostructured BaTiO₃/TiO₂ and SrTiO₃/TiO₂ (all other systems were also verified to have such microstructures, but are not shown), the *mc*-core/*ns*-shell heterostructure was achieved for all annealing temperatures and on both core compositions. Though the thickness of the coating varies slightly from location to

location, the range appears to be from 25 to 100 nm, except for the occasional surface agglomerate that was likely attached through a coalescence event in solution. This thickness is similar to the thickness of dense TiO₂ films that exhibited substrate controlled, domain specific reactivity at their surfaces.⁸⁻¹⁰ No direct relationship between the annealing temperature and coating thickness was discovered.

5.2.2 Surface Area and Pore Structure

The surface area and pore structure measured by the BET and BJH methods are summarized in table 5-2. Part of this data has been shown in Chapter 4. This table provides a pronounced positive inverse correlation between surface area and annealing temperature. An increased annealing temperature results in a decreased surface area, which agrees with the TEM and XRD results. The surface area of TiO₂ annealed at 800 °C is 1 m²/g, indicating that TiO₂ should have a grains size of about a micron. Though the surface area of the heterostructures also decreased with increasing annealing temperature, the decreasing rate of surface area for the heterostructures is obviously slower than that of TiO₂ alone. When the annealing temperature is higher than 500 °C for BaTiO₃/TiO₂ and 600 °C for SrTiO₃/TiO₂, respectively, the surface area of heterostructures is even larger than that of TiO₂ alone. The surface area of micron-sized BaTiO₃ and SrTiO₃ is close to 1 m²/g (which is not shown here). The decreased rate of pore collapse for the heterostructures indicates further that the interaction between the core and the shell leads to a stabilization of the shell. This

strong interaction hinders the collapse of pores in the nanostructured coating. The decrease of pore volume with increasing annealing temperature also confirms this explanation.

Table 5-2 Summary of physical properties of various photocatalysts annealed at different temperatures.

Catalyst	Annealing temperature (°C)	S (m ² /g)	V _p (cm ³ /g)	V _{H₂, 6h} (μmol/m ²)	R _{H₂, 6h} (μmol(g·h) ⁻¹)
TiO₂	400	93	0.19	11	171
	500	70	0.21	12	140
	600	16	0.06	18	48
	700	6	0.04	4	4
	800	1	0.004	0	0
BaTiO₃/TiO₂	400	72	0.15	9	108
	500	61	0.2	13	132
	600	44	0.14	28	205
	700	20	0.14	27	90
	800	15	0.09	18	45
SrTiO₃/TiO₂	500	47	0.16	22	132
	600	41	0.14	31	205
	700	22	0.13	12	44
	800	12	0.10	8	16
	900	7	0.02	0	0

5.2.3 Photocatalytic Hydrogen Production

The measured photocatalytic activity depends on the annealing temperature. As shown in table 4-2 in Chapter 4, when P25 was annealed at 500 °C, its value for V_{H₂,6h} (and R_{H₂}) dropped to 24 (180) from 30 (245) μmol·m⁻² (μmol·g⁻¹h⁻¹), concomitant with a slight loss in overall surface area. In contrast, the heterostructured

powders produced more hydrogen after being annealed at a higher temperature. The detailed values of hydrogen production per surface area and hydrogen production rate per mass for heterostructured powders and unsupported TiO₂ annealed at different temperatures is shown in table 5-2.

The photocatalytic activity of $V_{H_2,6h}(R_{H_2})$ for BaTiO₃/TiO₂ annealed at $T_A = 400, 500,$ and $600\text{ }^\circ\text{C}$ increases from 9 (108) to 13 (132) to 28 (205) $\mu\text{mol}\cdot\text{m}^{-2}$ ($\mu\text{mol}\cdot\text{g}^{-1}\text{h}^{-1}$), respectively. Similarly, these values improve for SrTiO₃/TiO₂ annealed at $T_A = 500$ and $600\text{ }^\circ\text{C}$, from 22 (172) to 31 (212) $\mu\text{mol}\cdot\text{m}^{-2}$ ($\mu\text{mol}\cdot\text{g}^{-1}\text{h}^{-1}$). In contrast to P25, the hydrogen production from the heterostructured powders increases with annealing temperature, even though they also experience a slight decrease in overall surface area. This increase in activity can be ascribed to either the improved crystallinity of the *ns*-TiO₂ coating or the improved bonding between the *ns*-TiO₂ coating and the *mc*-(Ba,Sr)TiO₃ core. With the further increase of annealing temperature from $700\text{ }^\circ\text{C}$ to $900\text{ }^\circ\text{C}$, hydrogen production begins to decrease. Hydrogen production per surface area from BaTiO₃/TiO₂ annealed at $700\text{ }^\circ\text{C}$ ($27\ \mu\text{mol}\cdot\text{m}^{-2}$) is close to the value of BaTiO₃/TiO₂ annealed at $600\text{ }^\circ\text{C}$ ($28\ \mu\text{mol}\cdot\text{m}^{-2}$), but the heterostructure annealed at $800\text{ }^\circ\text{C}$ produces much less ($18\ \mu\text{mol}\cdot\text{m}^{-2}$). The decrease of photocatalytic activity annealing above $600\text{ }^\circ\text{C}$ is more obvious for SrTiO₃/TiO₂. The hydrogen produced per surface area of SrTiO₃/TiO₂ is only $12\ \mu\text{mol}\cdot\text{m}^{-2}$ when the heterostructure is annealed at $700\text{ }^\circ\text{C}$, much less than the sample annealed at $600\text{ }^\circ\text{C}$ ($31\ \mu\text{mol}\cdot\text{m}^{-2}$). No detectable hydrogen was produced from

SrTiO₃/TiO₂ annealed at 900 °C. The hydrogen production rate changes in the same way as the amount of hydrogen produced per surface area.

It is also important to compare the amount of hydrogen evolved by the heterostructured materials to the amount of hydrogen evolved by freestanding *ns*-TiO₂ annealed at the same temperatures. When annealed at 400, 500, and 600 °C, the *ns*-TiO₂ powders yield 11, 12, and 18 μmol/m² of hydrogen, respectively. Like the heterostructure, the amount of hydrogen per area increases with annealing temperature, but not as significantly. However, the rate of hydrogen production per unit mass of catalyst actually decreased from 171 to 140 to 48 μmol•g⁻¹h⁻¹ for T_A = 400, 500, and 600 °C, respectively. The increase in the volume of hydrogen generated per unit surface area is likely to be related to the improved crystallinity of the *ns*-TiO₂ powder with increased annealing temperature. This contrasts the effect of annealing on P25, for which a decrease in the hydrogen generated per surface area was observed by annealing. However, the overall loss of activity per unit mass illustrates that the loss of surface area is more important than the improved crystallinity for the freestanding *ns*-TiO₂. Because the increase (with annealing temperature) in the amount of hydrogen generated per surface area by the heterostructured materials is greater than the marginal increase for the free-standing titania, it is unlikely to be caused by a simple increase in crystallinity.

The improved activity of the heterostructure with annealing may be the result of improved structural characteristics of the interface between the *mc*-(Ba,Sr)TiO₃ core cores and the *ns*-TiO₂ shells, allowing photogenerated carriers in the cores to be

transferred to the high surface area shells, similar to the activity of the dense thin film coatings on BaTiO₃.^{8,10,11} Compared with the sample annealed at 600 °C, the hydrogen production per surface area for the unsupported titania decreased greatly when the sample annealed at 700 °C and no hydrogen was detected at 800 °C. However, the heterostructures still can produce hydrogen when annealed at 800 °C. This is direct and clear evidence showing that the heterostructures have enhanced photocatalytic activity compared with their components alone.

5.3 Effect of Coating Thickness

The geometric features of coatings need to be studied because the interface where the TiO₂ coating meets the Pt cocatalyst is likely the place where photocatalytic water splitting occurs. The geometric dimensions of the coating are believed to determine the influence of the core on the catalytic activity. The previous results in our group showed that a BaTiO₃ substrate coated with a thin layer (\approx 10 - 100 nm) of a TiO₂ film exhibits photocatalytic activity for silver nitrate reduction that depends on the thickness of the TiO₂ layer,^{8,11} thicknesses similar to the current heterostructured coatings. It was shown earlier that the influence from the substrate is diminished with the increasing thickness of the film. Based on this point, it is interesting to investigate the relationship between photocatalytic activity and the thickness of the coatings.

The control of coating thickness is achieved by coating the core materials multiple times and using the same processing procedure as for the heterostructured

powders coated once (as discussed in Chapter 4). TEM bright field images of BaTiO₃/TiO₂ coated once, twice, and three times (each annealed at 500 °C) are shown in figure 5-5. Compared with the previous TEM bright field images of powders coated once, shown in figure 5-2-c and 5-2-d, most physical parameters, such as the crystal size of TiO₂ coatings, are similar between coatings having different numbers of coatings.

The surface area and pore structure data of those powders are shown in table 5-3. Based on this data, the pore volume of the heterostructure increased a little with an increase of coating cycles, but the change was not large. The pore size distribution of powders coated with different coating cycles is shown in figure 5-6. From this figure, it can be observed that the pore size distributions of BaTiO₃/TiO₂ heterostructures with different numbers of coating cycles did not show significant differences. The primary differences between these powders are simply the overall thicknesses of the coatings. Based on TEM images of the powders, the thickness of TiO₂ layers for powders coated twice was approximately 100-150 nm, essentially twice as large as for powders coated once (40-90 nm). The thickness of TiO₂ coated three times is \approx 150-250 nm, slightly smaller than three times the thickness of a single coating layer. These results show that the thickness of the coating can be controlled by varying the number of coating cycles. The surface area increased with the number of coating cycles. This is reasonable because with the increased coating thickness, there is more nanostructured, high surface area TiO₂ and this increases the total surface area of the heterostructure.

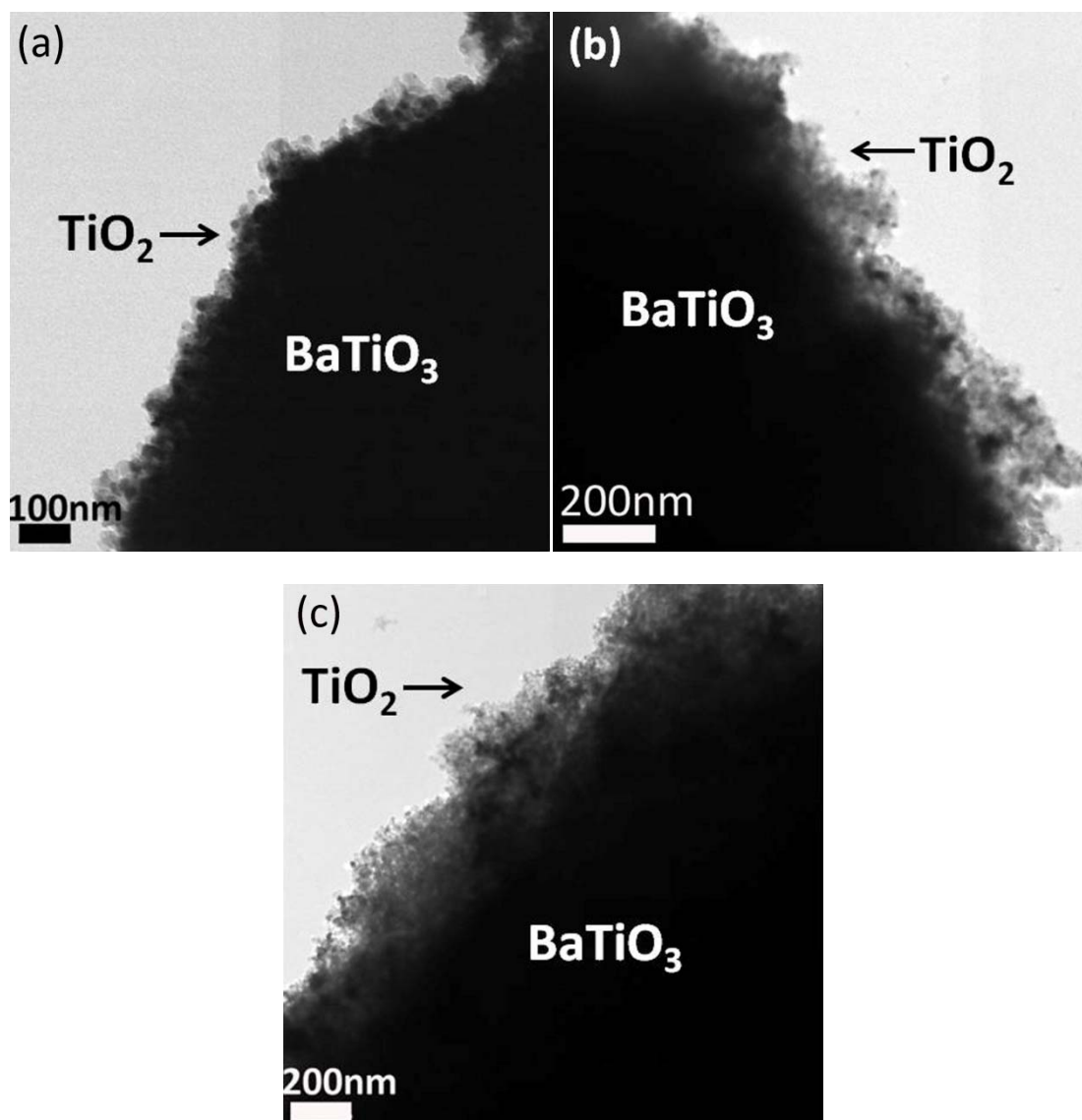


Figure 5-5 TEM bright field images of BaTiO₃/TiO₂ annealed at 500 °C with (a) one coating cycle, (b) two coating cycles, and (c) three coating cycles.

The photocatalytic activity of BaTiO₃/TiO₂ with different coating thicknesses is shown in table 5-5. These data show that BaTiO₃/TiO₂ powders coated twice produce more hydrogen at a great rate than samples coated once or three times. For samples coated once and twice, the volume of hydrogen produced after 6 hours of irradiation increases from 13 μmol/m² to 17 μmol/m². The hydrogen production rate also increased from 117 μmol(g·h)⁻¹ to 181 μmol(g·h)⁻¹. After a third coating cycle, the hydrogen production rate decreased to 125 μmol(g·h)⁻¹, even though BaTiO₃/TiO₂

coated with 3 cycles has a higher surface area. Because the processing was not changed, the reason for the change of reactivity is likely the difference of coating thickness; this will be discussed further in Section 5.5.

Table 5-3 Summary of physical properties of BaTiO₃/TiO₂ annealed at 500 °C with different coating cycles. (BTO/nTiO₂: n means coating cycles.)

Catalyst	S (m ² /g)	V _p (cm ³ /g)	V _{H₂, 6h} (μmol/m ²)	R _{H₂, 6h} (μmol(g·h) ⁻¹)
BTO/TiO ₂	61	0.20	13	117
BTO/2TiO ₂	64	0.25	17	181
BTO/3TiO ₂	68	0.26	11	125

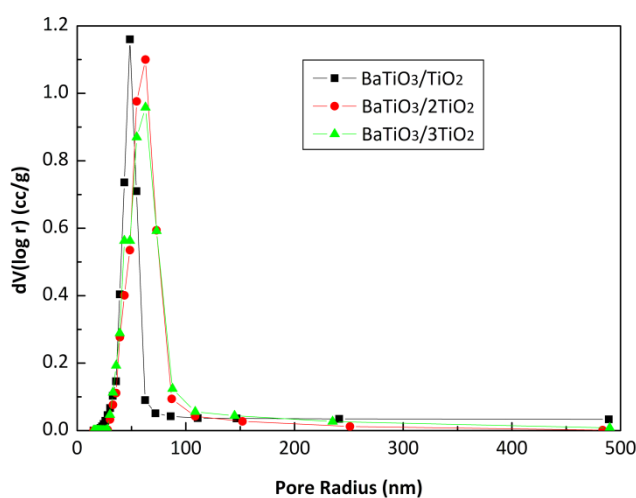


Figure 5-6 Pore size distribution of BaTiO₃/TiO₂ annealed at 500 °C with different coating cycles.

5.4 Effect of Pt Loading Content

Hydrogen production by heterostructured SrTiO₃/TiO₂ (annealed at 600°C) with different cocatalyst Pt loadings (in 100 mL of an 8 % methanol/water mixture) is shown in figure 5-7. The Pt weight percentage varies from 0.1 % to 2 %. The SrTiO₃/TiO₂ loaded with 1 % Pt was found to exhibit the greatest photocatalytic

activity for hydrogen production. In the range from 0.1 % to 2 %, the reactivity increases with increasing loading amount until 1 weight percent, and then drops a little when the loading is increased to 2 %. This phenomenon is consistent with a previous report on the effect of Pt loading on photocatalytic activity.¹²

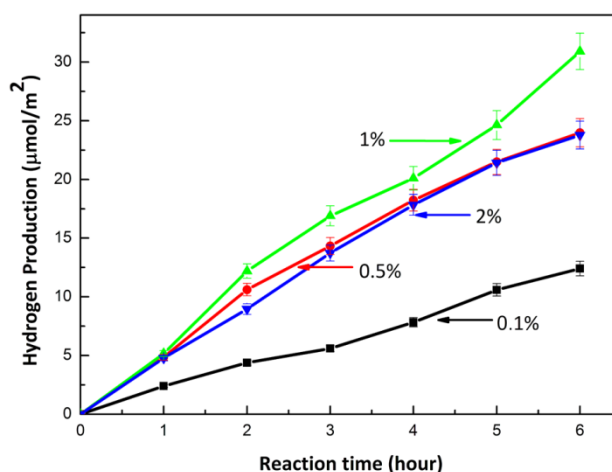


Figure 5-7 Hydrogen production from SrTiO₃/TiO₂ annealed at 600 °C with different amounts of Pt. (The number marked in the figure is referred to weight percentage relative to the entire photocatalyst mass.)

5.5 Discussion

In addition to the enhancement of (Ba,Sr)TiO₃/TiO₂ heterostructure for hydrogen production discussed in the Chapter 4, another observation made in this chapter is that the photocatalytic activity per surface area increases initially with increasing annealing temperature and reaches the highest value at $T_A = 600$ °C. This does not occur in unsupported TiO₂. As discussed in the Chapter 4, the core absorbs photons and transfer photoexcited charge carriers to the nanostructured shell. The heterostructured catalyst matches the length scales for both the absorption in the core and the reactivity at the surface, as long as the integrity of the interface allows charge transfer. Annealing at high temperature leads to improved shell crystallinity as well as

interface properties. It is believed that the intimate contact and the strong interaction at the heterostructured interface between the two solids also can be considered as one reason for enhanced photocatalytic activity with increasing annealing temperature. The sonomechanical mixture (see Section 4.1.2) of BaTiO₃ and commercial TiO₂ did not show improved photocatalytic hydrogen production, which confirms the importance of the interface between the components. This is a possible reason why (Ba,Sr)TiO₃/TiO₂ heterostructures show an increasing hydrogen production rate with annealing temperature from 108 μmol/(g·h) (BaTiO₃/TiO₂) at 400 °C to 205 μmol/(g·h) at 600 °C, while unsupported TiO₂ shows a decrease in reactivity with annealing temperature from 171 μmol/(g·h) to 48 μmol/(g·h). In addition, the increase of the photocatalytic activity per surface area for all photocatalysts, with increasing temperature to 600 °C, is attributed to increasing crystallinity of materials. The crystallinity increases with the increasing temperature,¹³ which decreases the recombination rate of charge carriers and is therefore beneficial for photocatalytic hydrogen production.

In addition to the quality of the interface and crystallinity, the phase composition of the nanostructured TiO₂ coating changes with the annealing temperature. The percentage of anatase TiO₂ in the BaTiO₃/TiO₂ heterostructures varies from 93.6% at 400 °C to 66.5% at 800 °C. It has been reported that anatase shows better photocatalytic activity for hydrogen production than rutile processed at the same conditions.⁵ This is one reason to explain why the photocatalytic reactivity per surface area of all photocatalyst begins to decrease after 600 °C, when the percentage of

anatase TiO_2 decreases greatly. TiO_2 annealed at 800 °C did not even produce detectable amounts of hydrogen. Because of the support, the anatase content of $\text{BaTiO}_3/\text{TiO}_2$ did not change greatly from 600 °C to 700 °C and thus the hydrogen production per surface area also did not change. The transformation from anatase to rutile also leads to changes in light absorption. The absorption coefficients for anatase and rutile are $2 \times 10^3/\text{cm}$ and $1 \times 10^5/\text{cm}$, respectively.^{11,14} Rutile will absorb more light before it reaches the core and this will influence the photocatalytic activity.

The density of the titania coating also increases with the annealing temperature. This has been confirmed by TEM images of $\text{SrTiO}_3/\text{TiO}_2$ annealed at 800 °C, as shown in figure 5-4, and decreasing pore volumes with the increasing temperature, as shown in table 5-2. Denser coatings make the infiltration of the solution more difficult. This means that electrons from the microcrystalline core need to travel longer distances to the outer TiO_2 coating to reach the active sites, which will increase the recombination rate of photogenerated charge carriers.

The results show that the heterostructure also can retard the phase transformation of anatase to rutile and prevent pore collapse, thus maintaining a keep high surface area and high photocatalytic activity after high temperature annealing. As shown in table 5-2, the $(\text{Ba,Sr})\text{TiO}_3/\text{TiO}_2$ heterostructures shows enhanced photocatalytic activity, both for hydrogen production per surface area and hydrogen production rate, compared with TiO_2 alone when the annealing temperature is 600 °C or higher. While no hydrogen is detected when TiO_2 annealed at 800 °C is used as a catalyst, $(\text{Ba,Sr})\text{TiO}_3/\text{TiO}_2$ still produces hydrogen after annealing at 800 °C ($18 \mu\text{mol}/\text{m}^2$ and 8

$\mu\text{mol}/\text{m}^2$). The use of a microcrystalline core and nanostructured shell for heterostructured photocatalyst design needs to be further investigated. The surface area of all photocatalysts decreased with increasing annealing temperature. This is a primary reason leading to the decrease of hydrogen production rate for the photocatalysts annealed at high temperature.

The influence of annealing temperature on photocatalytic activity is quite complex and it is hard to attribute to the change of photocatalytic activity to the change of a single factor. The annealing temperature influences the interface quality, phase composition, light absorption, crystallinity, mesoporosity and surface area. Still, there is a window wherein the performance can be optimized, as shown.

The primary observation for the influence of coating thickness on photocatalytic activity of the heterostructures is that the photocatalytic activity of heterostructured $\text{BaTiO}_3/\text{TiO}_2$ initially increases to a peak and then decrease with increasing coating thickness. This phenomenon can be explained by figure 5-8. This figure is a highly simplified schematic energy level diagram for $\text{BaTiO}_3/\text{TiO}_2$ with thick/thin coating and positive/negative polarization. The assumptions for the schematic drawing are the same as those used to construct figure 4-16. Figure 5-8 (c) and (d) are used to explain why $\text{BaTiO}_3/\text{TiO}_2$ heterostructures with thin coatings show enhanced photocatalytic activity compared to the components alone. The detailed explanation has been discussed in Chapter 4. Figure 5-8 (a) and (b) are used to explain the situation of $\text{BaTiO}_3/\text{TiO}_2$ with thick coating. In general, the thickness of the depletion layer should be about 100 nm.¹⁵ When the coating thickness is larger than the depletion layer width,

the bands can relax to the bulk level in the center of the coating. In this case, the photocatalytic activity of BaTiO₃/TiO₂ should be the same as the bulk TiO₂. Based on our experiment, it can be noticed in table 5-3 that the amount of hydrogen produced per surface area from BaTiO₃/3TiO₂ (the number before TiO₂ represents coating cycles.) is about 11 μm/m², which is quite close to the value of TiO₂ alone (12 μm/m²). This is consistent with our speculation.

When the coating thickness is smaller than the depletion layer width, the band structure of BaTiO₃/TiO₂ is drawn in figure 5-8 (c) and (d). Initially, increasing thickness means increasing the number of surface active sites for hydrogen production. Increasing the coating thickness for BaTiO₃/TiO₂ increases the photocatalytic hydrogen production. However, when the coating thickness is larger than the depletion layer width, the band bending of TiO₂ can be fully relaxed to the bulk level. In addition, according to the internal fields discussed in Chapter 4, it is inferred that with increasing coating thickness, the effects from the core will decrease or even vanish and the photocatalytic reactivity will be the same as the bulk coating material. The third reason is that with the increasing coating thickness, the electrons transferring from the core material to the shell need to migrate longer distances to participate the redox reaction. This will increase the possibility of charge carrier recombination and thus decrease the photocatalytic hydrogen production.

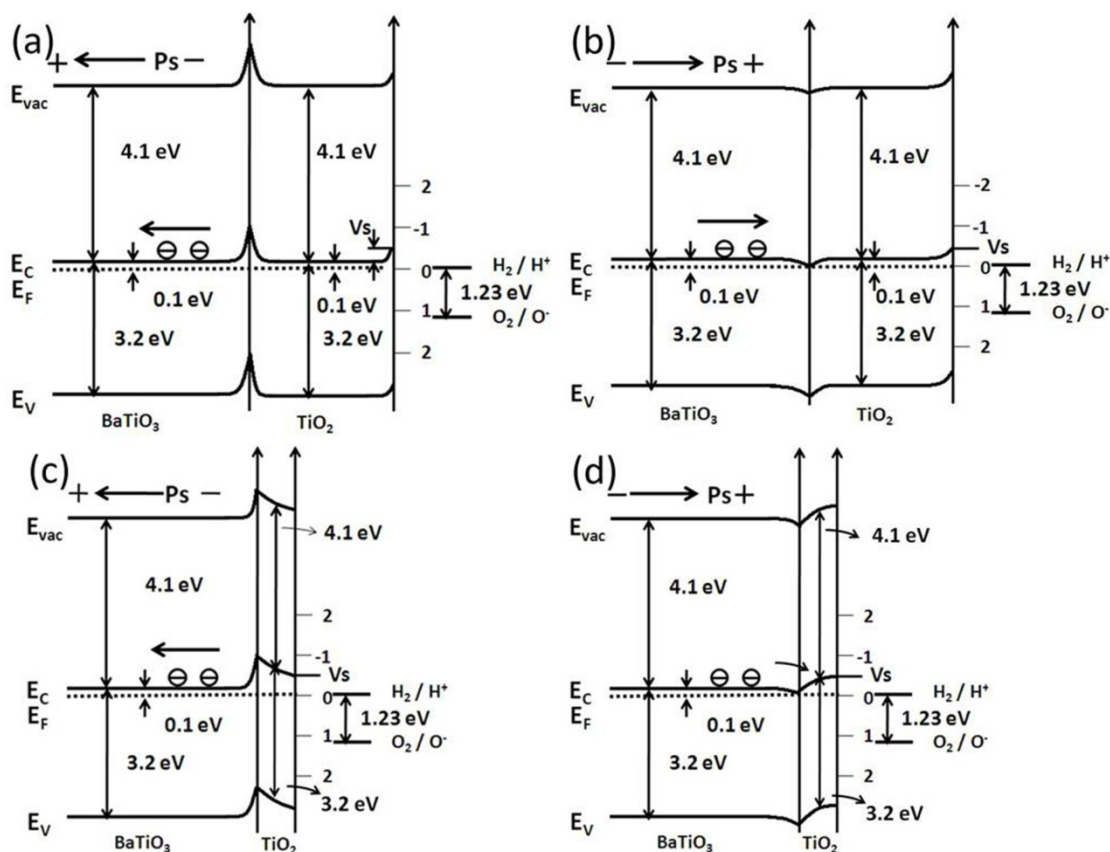


Figure 5-8 A highly simplified schematic representation of band structure diagram of heterostructured BaTiO₃/TiO₂ for: (a)(b) thick and (c)(d) thin coatings with different polarization directions. (E_{vac} , E_c , E_f and E_v represent the edge for vacuum level, conduction band, Fermi level and valance band, respectively. P_s refers to spontaneous polarization from ferroelectrics. The hydrogen and oxygen redox level are shown in the right.)

The amount of added Pt, which serves as a cocatalyst, was optimized for heterostructured SrTiO₃/TiO₂. The result shows that photocatalytic hydrogen production reached the maximum value when SrTiO₃/TiO₂ is loaded with 1% Pt. Increasing photocatalytic hydrogen production from 0.1% to 1% can be attributed to the increase of active sites for hydrogen production. More effective cocatalyst loading promotes Schottky barrier formation between TiO₂ and Pt, leading to the effective separation of charge carriers.¹² The observation that the photocatalytic hydrogen production rate decreases with increased Pt loading is probably explained by

agglomeration and growth of Pt nanoparticles on SrTiO₃ surface.¹⁶ In addition, Pt also can promote the back reaction of hydrogen and oxygen to form water.¹⁷ Increased loading increases the back reaction.

5.6 Summary

In this chapter, three detailed parameters corresponding to the heterostructured powders are optimized to investigate their effects on photocatalytic activity. The following results are summarized:

1. Annealing temperature affects the physical properties and photocatalytic activity of heterostructured powders. With increasing annealing temperature, the photocatalytic hydrogen production rate from the heterostructured powders initially increases, while their components exhibit an opposite trend. (Ba,Sr)TiO₃/TiO₂ heterostructures shows the highest reactivity for hydrogen production when annealed at 600 °C and then their photocatalytic activity decreases with further increases in annealing temperature.
2. The coating thickness is directly related to photocatalytic activity of heterostructured powders. BaTiO₃/TiO₂ coated twice shows the highest photocatalytic activity for hydrogen production, compared with the heterostructure coated with one or three times.
3. Cocatalyst loading has an influence on photocatalytic hydrogen production. SrTiO₃/TiO₂ with 1 wt% Pt loading reaches the highest reactivity among the loading amounts studied.

5.7 References

- (1) Chan, C. K.; Porter, J. F.; Li, Y. G.; Guo, W.; Chan, C. M. *Journal of the American Ceramic Society* **1999**, *82*, 566.
- (2) Porter, J. F.; Li, Y.-G.; Chan, C. K. *Journal of Materials Science* **1999**, *34*, 1523.
- (3) Wu, N. L.; Lee, M. S.; Pon, Z. J.; Hsu, J. Z. *Journal of Photochemistry and Photobiology A-Chemistry* **2004**, *163*, 277.
- (4) Gao, L.; Zhang, Q. H. *Scripta Materialia* **2001**, *44*, 1195.
- (5) Hurum, D. C.; Agrios, A. G.; Gray, K. A.; Rajh, T.; Thurnauer, M. C. *Journal of Physical Chemistry B* **2003**, *107*, 4545.
- (6) Kozlova, E. A.; Korobkina, T. P.; Vorontsov, A. V.; Parmon, V. N. *Applied Catalysis A: General* **2009**, *367*, 130.
- (7) Cullity, B. D.; Stock, S. R. *Elements of X-Ray Diffraction*; Addison-Wesley Publishing Co: MA, 1978.
- (8) Burbure, N. V.; Salvador, P. A.; Rohrer, G. S. *Chemistry of Materials* **2010**, *22*, 5831.
- (9) Burbure, N. V.; Salvador, P. A.; Rohrer, G. S. *Chemistry of Materials* **2010**, *22*, 5823.
- (10) Burbure, N. V.; Salvador, P. A.; Rohrer, G. S. *Journal of the American Ceramic Society* **2006**, *89*, 2943.
- (11) Burbure, N. V.; Salvador, P. A.; Rohrer, G. S. *Chemistry of Materials* **2010**, *22*, 5823.
- (12) Yi, H.; Peng, T.; Ke, D.; Ke, D.; Zan, L.; Yan, C. *International Journal of Hydrogen Energy* **2008**, *33*, 672.
- (13) Kudo, A.; Miseki, Y. *Chemical Society Reviews* **2009**, *38*, 253.
- (14) Park, Y. R.; Kim, K. J. *Thin Solid Films* **2005**, *484*, 34.
- (15) Albery, W. J.; Philip, N. B. *Journal of The Electrochemical Society* **1984**, *131*, 315.
- (16) Hwang, D. W.; Kim, H. G.; Kim, J.; Cha, K. Y.; Kim, Y. G.; Lee, J. S. *Journal of Catalysis* **2000**, *193*, 40.
- (17) Osterloh, F. E. *Chemistry of Materials* **2008**, *20*, 35.

6. Photocatalytic Activity of $\text{PbTiO}_3/\text{TiO}_2$ Heterostructured Catalysts

As shown in Chapter 4, the $mc\text{-(Ba,Sr)TiO}_3/ns\text{-TiO}_2$ core-shell material exhibits enhanced hydrogen production compared to its components under UV-visible light irradiation. An important next step is to demonstrate that heterostructured catalysts can function under visible light irradiation (without UV contributions). Ultimately, technologically useful photocatalysts are likely to function under visible light irradiation. In this chapter, the narrow band gap ferroelectric semiconductor PbTiO_3 , which is reported to absorb the visible light, is used as the micron-sized core material and coated with nanostructured TiO_2 . Its photocatalytic activity for methylene blue dye degradation will be investigated and it will be demonstrated that the heterostructured catalyst is more effective (at dye degradation) than its components under visible light irradiation. Structural characterization is performed to confirm the core/shell structure. Pb-doped TiO_2 is used as a control material to investigate the influence of Pb-doping on light absorption and photocatalytic activity of the coating material. Finally, we discuss a model of the electronic energy states of the core/shell system that provides a rationale for the enhancement of photocatalytic activity of $mc\text{-PbTiO}_3/ns\text{-TiO}_2$ catalysts.

6.1 Structural Characterization of $\text{PbTiO}_3/\text{TiO}_2$ Heterostructure

6.1.1 Phase Composition

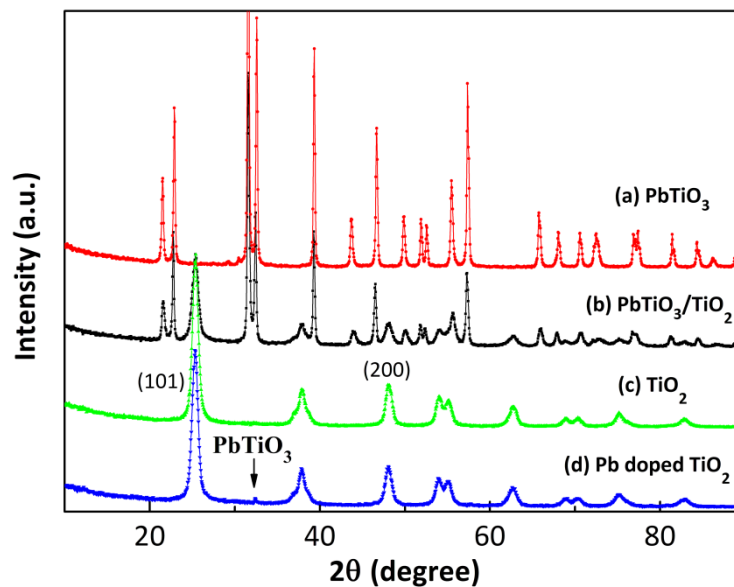


Figure 6-1 X-ray diffraction patterns of (a) PbTiO_3 , (b) $\text{PbTiO}_3/\text{TiO}_2$, (c) TiO_2 , and (d) Pb-doped TiO_2 annealed at 500 °C.

X-ray diffraction patterns of the $\text{PbTiO}_3/\text{TiO}_2$ core-shell particles, the component phases, and 1 mol% Pb-doped titania, all annealed at 500 °C, are shown in figure 6-1. All diffraction peaks could be indexed to the standard patterns of PbTiO_3 (JCPDS 78-0299) and anatase TiO_2 (JCPDS 46-1237). The pattern for the composite is consistent with a superposition of the two component phases, indicating that almost no reaction occurs between PbTiO_3 and TiO_2 . This observation is consistent with the PbO-TiO_2 phase diagram.¹ Compared with the diffraction pattern of TiO_2 , Pb-doped TiO_2 shows a small peak at $2\theta = 32.4^\circ$, which is consistent with the most intense peak in the PbTiO_3 pattern, i.e., reflection from the (110). This indicates that the doping

exceeded the solubility limit of Pb in TiO₂ and that a small amount of the ternary compound was formed. The 2θ peaks at 25.2° and 47.8° are indexed to (101) and (200) planes of anatase, (as marked in figure 6-1) and were used to calculate the lattice parameters of TiO₂, Pb-doped TiO₂, and *ns*-TiO₂ in the heterostructure. The results are shown in table 6-1. Because the ionic radius of Pb is much larger than Ti, it is expected that substitution at the Ti site will cause some lattice expansion. The data in table 6-1 indicate a significant lattice expansion occurred for the Pb-doped TiO₂ and a slight lattice expansion occurred for the TiO₂ in the heterostructures. The expansion of the unit cell indicates that Pb was substitutionally incorporated in the doped titania, with the amount being below the targeted value (owing to the PbTiO₃ formation) for the Pb-doped TiO₂. The intermediate value of the lattice parameters for the TiO₂ coating in the PbTiO₃/TiO₂ heterostructure indicates only a small amount of Pb interdiffuses to the coating through the interface (being less than the ≈ 1 mol% in the doped sample).

Table 6-1 Comparison of anatase d-spacings and lattice parameters for titania, Pb-doped TiO₂, and TiO₂ in the heterostructures (labeled H-TiO₂).

Material	d ₁₀₁ (Å)	d ₂₀₀ (Å)	a (Å)	c (Å)	cell volume (Å ³)
TiO ₂	3.501	1.889	3.778	9.315	133.0
H-TiO ₂	3.508	1.890	3.780	9.418	134.6
Pb-doped TiO ₂	3.515	1.892	3.784	9.492	135.9

6.1.2 Morphology

The TEM images in figure 6-2 illustrate the morphology and microstructure of

the heterostructured powders annealed at 500 °C. A typical particle is shown at low magnification in figure 6-2(a) and at higher resolution in figures 6-2(b&c). The interface between the *mc*-PbTiO₃ and *ns*-TiO₂ is highlighted in figures 6-2(b&c). The PbTiO₃ core is electron opaque and appears black in the images. The nanocrystalline TiO₂ shell appears as a semi-transparent layer surrounding the core. The partially transparent layer shows a granular contrast that corresponds to titania particles with an approximate diameter of 10 nm, which is consistent with the value of 9 nm calculated based on a Scherer analysis of the breadth of the x-ray peaks shown above. A sharp and clear interface between the micron-sized core and the nanostructured coatings can be observed. The thickness of the titania layer is not constant and varies in the range of 50-100 nm, except for the occasional agglomerate attached to the surface.

A high resolution TEM (HRTEM) image taken from the interface is shown in figure 6-2(c). The measured spacing of lattice fringes in the titania coating was 3.5 Å, corresponding to the interplanar distance of the (101) plane of anatase TiO₂. A selected-area electron diffraction (SAED) pattern of TiO₂ coating is presented in Figure 6-2(d). The SAED pattern shows a series of concentric circles, rather than sharp bright dots, in agreement with the polycrystalline nature of the nano-sized grains. Those diffraction circles were indexed and identified as the planes of tetragonal anatase TiO₂.

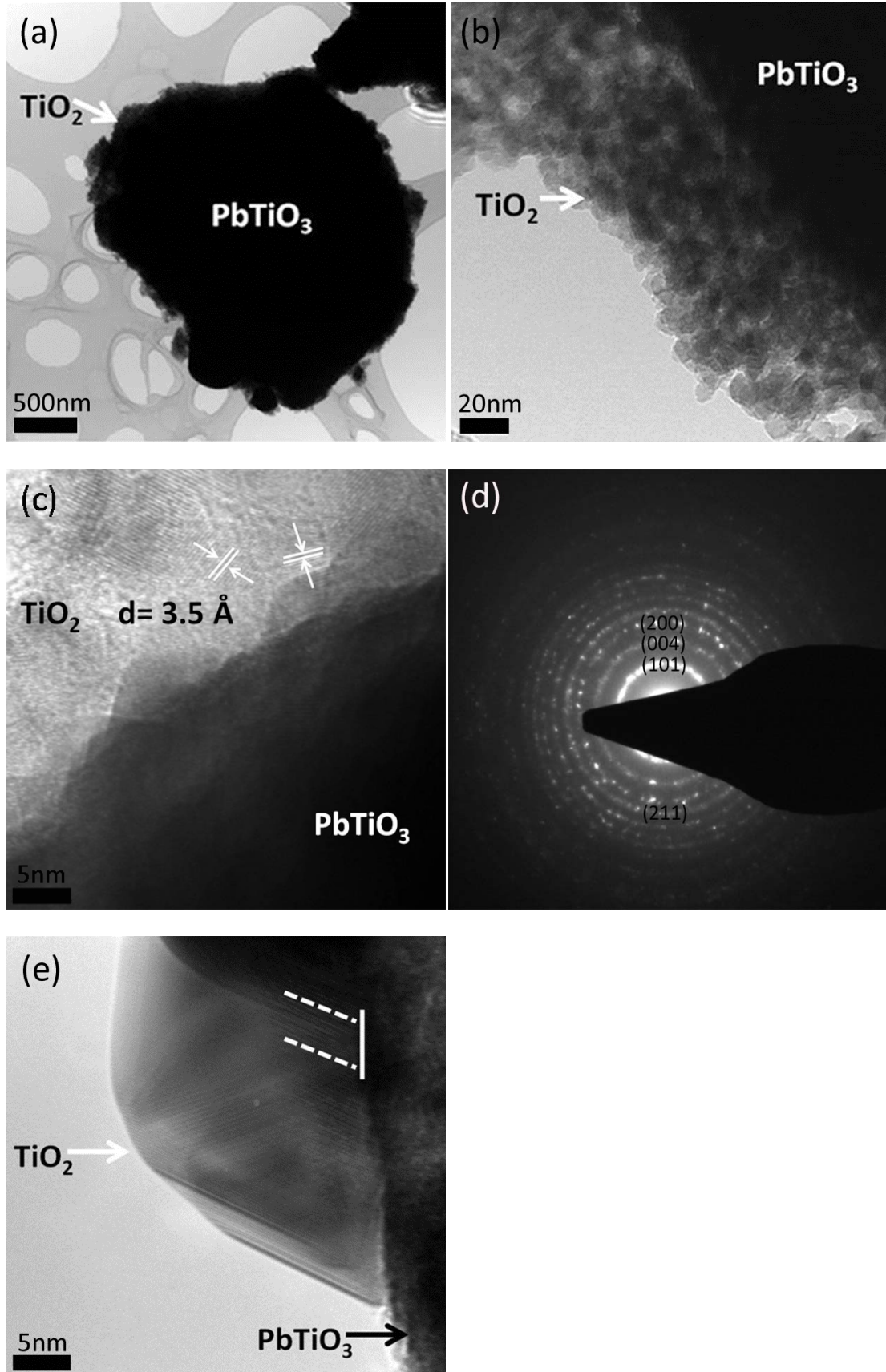


Figure 6-2 TEM images of heterostructured particles composed of *mc*-PbTiO₃ and *ns*-TiO₂ annealed at 500 °C: (a) low magnification bright field image of entire particle, (b) high

magnification bright field image of detail of the $\text{PbTiO}_3/\text{TiO}_2$ interface, (c) HRTEM image of the interface, (d) SAED of TiO_2 coating, and (e) HRTEM image of the interface after in-situ annealing with high energy electron beam.

To demonstrate the influence of high temperature annealing on the nanostructured TiO_2 and its interface with the micron-sized core, we carried out an in-situ “annealing” experiment in the TEM. The “annealing” was done using a high energy electron beam trained on the coatings for 2 seconds. A very thin coating area, with two or three TiO_2 particle layers, was selected and exposed to the high-energy electron beam. Then we investigated the same region with TEM after the electron beam annealing. The interface after in-situ annealing is shown in figure 6-2(e). The area in the right side of the interface, related to *mc*- PbTiO_3 core, did not change under electron beam exposure. However, coarsened TiO_2 grains are clearly observed on the left side of the interface, and the size of TiO_2 particle has increased from 10 nm to 25 nm. This also leads to a clear decrease in the overall surface area, which is unwanted for catalysis. The observation of fringes (marked with white curve and line) at the $\text{PbTiO}_3/\text{TiO}_2$ interface suggests a direct connection between the two phases, which is beneficial for the electron transfer between the core and shell. These observations support the arguments that ex-situ annealing leads to decreased surface areas but improved interfacial bonding, processes that have opposite effects on the overall catalytic activity.

6.1.3 Surface Area and Pore Morphology

The surface area and pore morphology of *mc*- PbTiO_3/ns - TiO_2 annealed at 400, 500, and 600 °C are shown in Table 6-2. The diameters of the PbTiO_3 particles are in

the micron range and, therefore, the surface area is small. This result is consistent with TEM images. The surface areas of the $\text{PbTiO}_3/\text{TiO}_2$ heterostructures decrease on annealing from $117 \text{ m}^2/\text{g}$ at $400 \text{ }^\circ\text{C}$ to $74 \text{ m}^2/\text{g}$ at $500 \text{ }^\circ\text{C}$ and to $26 \text{ m}^2/\text{g}$ at $600 \text{ }^\circ\text{C}$. This is the result of thermally driven consolidation and coarsening, as shown in the *in-situ* TEM experiment.^{2,3}

The isothermal curves and pore size distribution of $\text{PbTiO}_3/\text{TiO}_2$ annealed at 400 , 500 , and $600 \text{ }^\circ\text{C}$ are shown in figure 6-3. The isothermal curves of all $\text{PbTiO}_3/\text{TiO}_2$ curves belong to Type IV isothermal curve, which indicates the structure of the heterostructures is mesoporous. There is little change to the isothermal curves of $\text{PbTiO}_3/\text{TiO}_2$ heterostructures annealed at different temperatures, except for the P/P_0 value. The pore size distributions of $\text{PbTiO}_3/\text{TiO}_2$ heterostructures are narrow. Based on their measured mean pore sizes, shown in table 6-2, and pore size distribution, shown in figure 6-3-(b), the *mc-PbTiO₃/ns-TiO₂* and *ns-TiO₂* prepared by the sol-gel method can be considered mesoporous. This is consistent with their isothermal curves. With increasing annealing temperature, the pore volume decreased and pore radius increased because of thermal coarsening.

Table 6-2 Surface areas and pore characteristics of *mc-PbTiO₃/ns-TiO₂* and its components.

Material	Processing temperature ($^\circ\text{C}$)	BET surface area (m^2/g)	Pore volume (cc/g)	Pore radius D_v (r) (\AA)
<i>ns-TiO₂</i>	500	83	0.14	25
<i>mc-PbTiO₃</i>	500	2	0.01	N/A
<i>mc-PbTiO₃/ns-TiO₂</i>	400	117	0.19	23
	500	74	0.15	28
	600	26	0.13	55

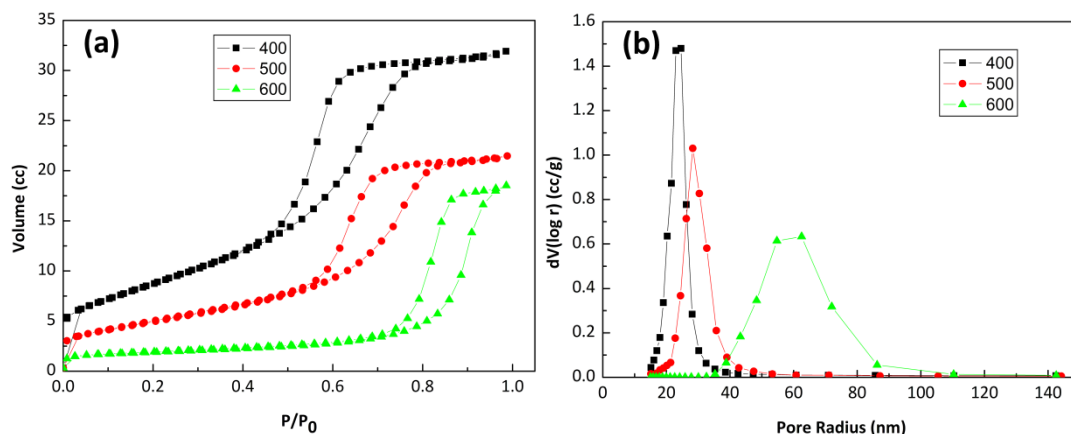


Figure 6-3 (a) Isothermal curves and (b) pore size distribution of PbTiO₃/TiO₂ annealed at different temperatures (the number in the caption refers to the annealing temperature).

6.1.4 Light Absorption

Figure 6-4 shows the UV-vis diffuse reflectance spectra of the *mc*-PbTiO₃/*ns*-TiO₂ as well as those of component phases and Pb doped TiO₂, all annealed at 500 °C. The region between 400 and 450 nm is magnified in the inset to highlight the details near the onset of absorption. The reflectance spectra recorded from the UV-vis spectrometer were converted to absorbance using the Kubelka-Munk function.⁴ The data shown in Figure 6-3 confirm that TiO₂ exhibits little absorbance of light with wavelengths longer than 400 nm. The onset of the light absorption by PbTiO₃ occurs at a longer wavelength because of its smaller band gap energy.⁵ Specifying a value for the band gap of PbTiO₃ is complicated by its anomalous absorption edge.⁶ Because of this, values for the band gap between 2.75 eV and 3.6 eV can be found in the literature.⁵⁻⁸ Micron-sized PbTiO₃ prepared by a molten salt methods was reported to have band gap of 2.75 eV,⁵ and this material is apparently similar to the material used here.

The absorbance data in figure 6-4 shows that PbTiO_3 begins to absorb light at 435 nm, a wavelength consistent with a band gap of 2.85 eV. The absorption edge of heterostructured $\text{PbTiO}_3/\text{TiO}_2$ is close to that of the PbTiO_3 core material, indicating that the core is the primary photon absorbing phase in the visible region of the spectrum. It is possible that Pb-doping of the coating leads to visible light absorption in the coating itself. However, the absorption spectrum of Pb-doped TiO_2 shows a negligibly small shift to the visible light region when compared with undoped TiO_2 . This indicates that the absorption of $\text{PbTiO}_3/\text{TiO}_2$ in the visible light region does not originate from Pb doping of the nanostructure coating. The influence of Pb doping on the extension of light absorption can be considered negligible in these materials.

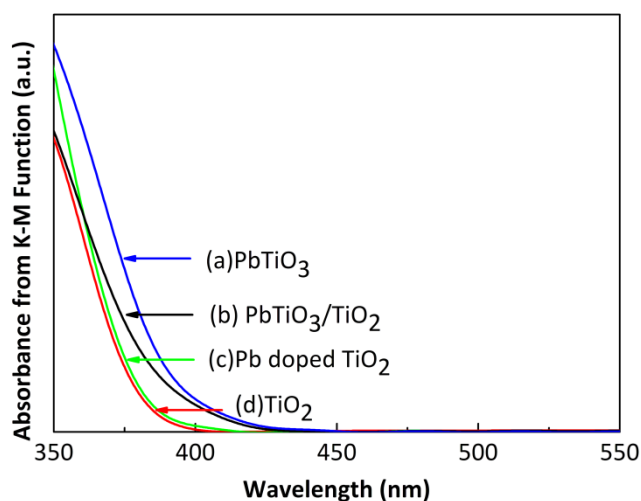


Figure 6-4 Absorbance data, converted from diffuse reflectance spectra using the K-M function for (a) $\text{PbTiO}_3/\text{TiO}_2$, (b) PbTiO_3 , and (c) TiO_2 annealed at 500 °C. The inset enlarges the absorbance spectra between 400 nm and 450 nm.

6.2 Photocatalytic Activity

mc- PbTiO_3 /*ns*- TiO_2 heterostructured powders annealed at 500 °C, and their component phases, were used to photochemically degrade methylene blue (MB) using visible light ($\lambda > 420$ nm). Methylene blue is an organic heterocyclic-dye and is

relatively stable against degradation in normal conditions. Photochemical degradation leads to a reduction in absorbance for the MB solution, which correlates to a reduction in concentration.

The results from MB degradation are shown in figure 6-5. The data denoted as “blank” is the result of a control experiment carried out in the same way as all of the others, but without an added catalyst. The constant absorbance with time verifies that methylene blue is not homogeneously degraded by visible light under these conditions. Similarly, no degradation is detected for the experiment with microcrystalline PbTiO_3 used as the photocatalyst. Recall that this sample has a small surface area compared to the others. Thus, this result does not necessarily mean that PbTiO_3 is inert for this reaction, simply that it is not capable of degrading detectible amounts of MB under these conditions. TiO_2 by itself shows modest reactivity, even though the absorbance data in figure 6-4 indicates that it is not able to absorb visible light photons. This phenomenon has been reported previously and is referred to as the “ TiO_2 -mediated dye degradation” process.^{9,10} According to the reported process, TiO_2 is not excited by the visible light but provides a pathway for electron transfer from excited dye molecules to oxygen atoms adsorbed on the TiO_2 surface. The generation of superoxide radical anion, $\cdot\text{O}_2^-$, and $\cdot\text{OH}$ radicals on the surface of TiO_2 are the primary species responsible for organic dye degradation in these conditions.^{9,10}

Compared with the low rates of MB degradation by TiO_2 , PbTiO_3 , and physical mixtures of the two phases, the *mc-PbTiO₃/ns-TiO₂* core/shell structure exhibits greater photochemical activity measured by the dye degradation rate. The greater

degradation rate is reflected in both the slope of the absorbance versus reaction time curve and by the total amount of dye degraded during the experiment. After 5 hours of irradiation, the concentration of MB in the solution decreased to 20 % of its initial concentration. The time evolution of the dye concentration can be reasonably accounted for by a pseudo-first-order model, represented by the following equation.¹¹⁻¹³

$$\ln(C_0/C) = K_{app}t$$

In this equation, C_0 is the dye concentration at time = 0, C the concentration of dye at time = t , K_{app} the apparent first-order reaction rate, and t the visible light exposure time. According to the data shown in figure 6-5, the MB removal rate over *mc*-PbTiO₃/*ns*-TiO₂ (0.24 h⁻¹) is 4.8 times greater than TiO₂ alone (0.05 h⁻¹). No significant dye degradation was observed in the blank experiment, indicating that self-degradation of the dye by visible light irradiation can be ignored. Also, the mechanical mixture of PbTiO₃ and TiO₂ showed less reactivity for dye degradation than *mc*-PbTiO₃/*ns*-TiO₂ core/shell structured powder prepared by sol-gel method, indicating the importance of the interface between the two phases.

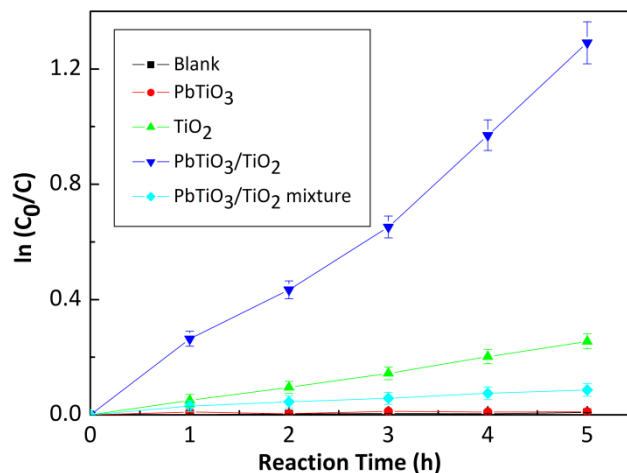


Figure 6-5 Photochemical dye degradation with PbTiO₃/TiO₂ annealed at 500 °C and its component phases during irradiation by visible light ($\lambda > 420$ nm). Absorbance data labeled blank, which is overlaid by the PbTiO₃ data, is from a control experiment conducted without the addition of a catalyst.

Figure 6-6 compares the dye degradation rates of *mc*-PbTiO₃/*ns*-TiO₂ annealed at 400 °C, 500 °C, and 600 °C. The results of the dye degradation experiment using Pb-doped TiO₂ are also shown in figure 6-6. The results indicate that the annealing temperature influences the photochemical activity of *mc*-PbTiO₃/*ns*-TiO₂. It is noteworthy that the photochemical activity of these heterostructured powders is not simply related to the surface area. The sample annealed at 500 °C degrades MB at the highest rate, even though it does not have the largest surface area. The powder annealed at 600 °C exhibits the lowest reactivity among the heterostructured *mc*-PbTiO₃/*ns*-TiO₂ samples. The photochemical reactivity of the Pb-doped TiO₂ is similar to the undoped, *ns*-TiO₂. The reaction rates are 0.049 h⁻¹ and 0.05 h⁻¹ for the Pb-doped and undoped materials, respectively.

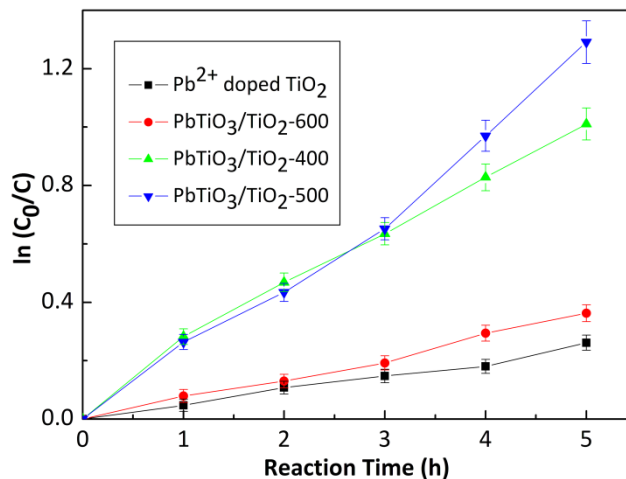


Figure 6-6 Methylene blue degradation with PbTiO₃/TiO₂ annealed at different temperatures from 400 °C to 600 °C and TiO₂ doped with 1 mol% Pb.

6.3 Discussion

The most interesting aspect of the results presented here is that PbTiO₃ microcrystals coated with nanostructured TiO₂ have a greater photochemical activity for methylene blue degradation under visible light than either of the components from which the composite is made, or a mixture of these two components. To understand the reactivity of the heterostructured catalyst, schematic energy level diagrams are constructed for both negative and positive polarizations normal to the heterostructure and these are presented in figure 6-7 (a) and (b), respectively. In this schematic, the band gap energy of PbTiO₃ and TiO₂ (anatase) is assumed to be 2.85 eV and 3.2 eV, respectively. The band gap for PbTiO₃ is based on the DRS measurement (Figure 6-4) and the band gap for TiO₂ is based on a reported value.^{14,15} The reported work function of TiO₂ is 4.2 eV¹⁶ and this value was used to position the Fermi level relative to the vacuum level. We assume that the Fermi level is 0.1 eV below the conduction band edge.¹⁷ The conduction band edge energy of PbTiO₃ was estimated,

using the method of Butler and Ginley,¹⁸ to be 4.23 eV below the vacuum level. The electrochemical equilibrium between solid and the solution is achieved by having a constant Fermi level throughout all three phases. In each case, it is assumed the surface potential, V_s , is controlled by the interaction between the titania and the aqueous solution and we use a value of 0.5 eV. The redox potential of 10^{-5} M methylene blue solution was reported to be +0.011 eV on NHE scale at pH = 7 and is marked in the figure.¹⁹ Finally, we assume that the energy levels in the TiO_2 layer are not fully relaxed to the bulk energy levels because it is thinner than the depletion layer which is about 100 nm in titania.²⁰

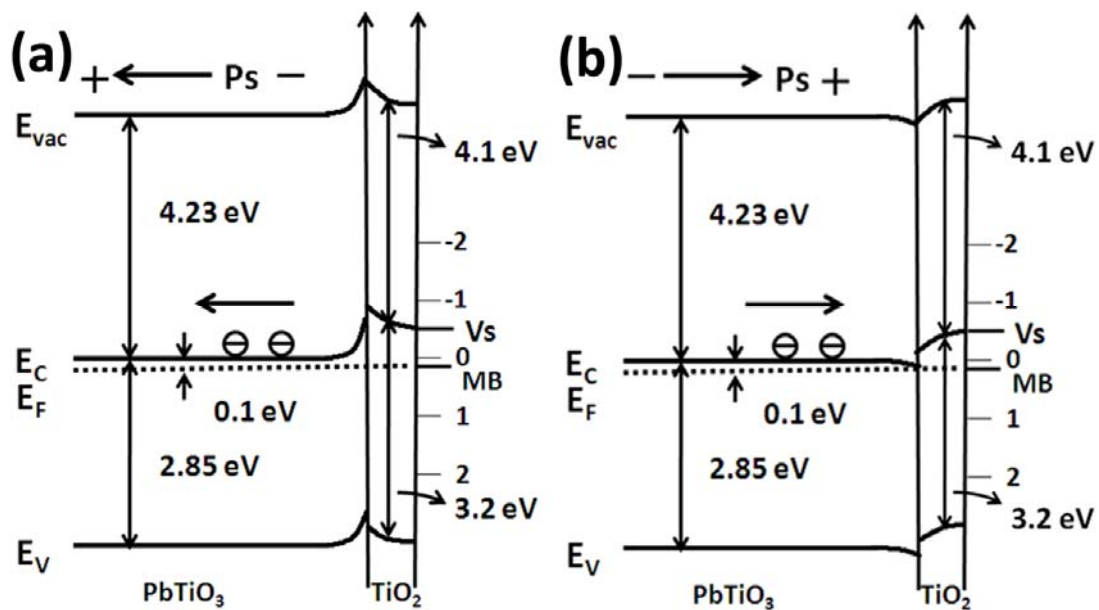


Figure 6-7 A schematic energy level diagram of $\text{PbTiO}_3/\text{TiO}_2$ with (a) negative polarization and (b) positive polarization normal to the heterostructure interface. E_{vac} , E_C , E_F , E_V , and E_s are the energies of the vacuum level, conduction band, Fermi level, valence band, and surface potential, respectively.

As stated above, figure 6-7 (a) to (b) respectively depict the energy levels for the heterostructures when the negative polarization (the positive direction of polarization points into the ferroelectric) and positive polarization (the opposite case) are normal

to the heterostructure interface. We ascribe band bending in the micron-sized ferroelectric core to a rise primarily from the spontaneous polarization, which has been measured to be $75 \mu\text{C}/\text{cm}^2$ at room temperature,²¹ and leads to an internal charge that is offset by the depletion & accumulation region in the doped semiconductor. The core also absorbs most of the visible light. Recall that the DRS data showed that the *mc*-PbTiO₃/*ns*-TiO₂ composite absorbed visible light, and that titania does not. Photogenerated electrons in PbTiO₃ will be drawn to the PbTiO₃/TiO₂ interface in positive domains and holes will be repelled from the interface, owing to the internal fields. The opposite process will occur in negative domains, where holes will be drawn to the interface. The use of micron-sized core is necessary to prevent the decrease in ferroelectric spontaneous polarization that occurs with decreasing particle size. The decrease in polarization begins in the range of 100-200 nm, so this is the minimum sized cores that support full polarization. The cores used in the present experiments were significantly larger than the minimum, and could perhaps be optimized further by decreasing the average size below a micron. Meanwhile, the fully extended space charge region of the micron-sized core can increase the amount of separated charge carriers and improve the efficiency of light absorption. Previous experiments demonstrated that *mc*-BaTiO₃/*ns*-TiO₂ exhibited higher photocatalytic activity for hydrogen production than *ns*-BaTiO₃/*ns*-TiO₂.

Once carriers reach the PbTiO₃/TiO₂ interface, figure 6-7 indicates that there are energy barriers for transmission. For example, electrons transported to the interface in positive domains (see figure 6-7 (b)) encounter increasing energy levels in the shell

layer and holes reaching the interface in negative domains encounter a similar barrier. It should be noted that the titania shell is actually porous and the energy levels are not expected to vary uniformly. For the charge carriers to be injected into the nanostructured TiO₂ layer, they must either have enough energy to overcome the barrier²² or they must tunnel through it.^{23,24} Because the titania grains are only on the order of 10-15 nm, the distances necessary for transport in the porous coating are significantly smaller than the complete shell thickness. Therefore, tunneling may be the dominant process. Because the transfer of photogenerated charge carriers from the core to the shell is essential for the reaction to occur, it is important that the core and shell are chemically bonded to each other, and not simply in contact. The importance of the quality of this interface is indicated by the low reactivity of the mechanical mixture of PbTiO₃ and TiO₂.

Because the outer TiO₂ layer is nanostructured and mesoporous, there is a large surface area to which the dye can absorb and charge carriers can be transferred. The dye degradation process has been studied and reported on previously.^{10,13,25} Based on these studies, it is agreed that photogenerated electrons combine with the adsorbed oxygen molecules to form superoxide radical anions, $\cdot\text{O}_2^-$. The photogenerated holes oxidize excited dye molecules to form radicals or they oxidize surface adsorbed H₂O to form hydroxyl radicals, $\cdot\text{OH}$. While it is the oxidation half of the reaction that is most directly associated with the dye degradation, both are essential for maintaining charge balance.

The annealing temperature influences the crystallinity,²⁶ surface area,²⁶ and the

contact at the core/shell interface,²⁷ and each of these characteristics have different effects on the photochemical activity. In the *mc*-PbTiO₃/*ns*-TiO₂ heterostructured powders, the sites where the charge carriers react with adsorbed molecules are on the TiO₂ surface, even though no charge carriers are generated in the TiO₂ layer. This means that the carriers must be transported from the light absorbing PbTiO₃ core to the titania/solution interface without recombination. Because crystal defects are known recombination centers, higher crystallinity and improved interface quality are expected to enhance the photochemical activity of heterostructures and these characteristics are expected to improve with greater annealing temperatures.

On the other hand, higher annealing temperatures are expected to reduce surface areas and this will decrease the photochemical activity. These considerations form the basis for a plausible explanation of the observed variation in reaction rate with annealing temperature. The sample annealed at the lowest temperature (400 °C) has the highest surface area (117 m²/g). The surface area of the sample annealed at 500 °C is 37 % lower, yet it has a slightly higher reactivity. In this case, we propose that increases in the crystallinity and interface quality offsets the reduction in surface area. The sample annealed at 600 °C exhibits the lowest reactivity and it has the lowest surface area (26 m²/g). In this case, it seems that any further gains in crystallinity or interface quality cannot offset the decrease in surface area. Finally, it should also be mentioned that the coating architecture is also important and affected by the annealing.¹² A dense shell blocks the penetration of the methylene blue to the inner parts of the shell near the core and forces charge carriers to be transported over longer

distances. Both of these factors will limit the photochemical activity.

Considering the fact that Pb-doping has been reported to extend the absorption edge of some layered perovskite photocatalysts to the visible light range, it might be proposed that the increased photochemical reactivity of PbTiO₃ supported titania is the result of a small amount of Pb that dissolved in the titania during processing.²⁸ Contrary to this suggestion, calculations predict that the band gap of anatase is enlarged by 0.02 eV with Pb doping.²⁹ To determine if changes in the electronic structure caused by Pb doping influence the reactivity, a control experiment was conducted to measure the degradation of methylene blue by Pb-doped titania. The result shows that Pb-doped TiO₂ is less reactive than *mc*-PbTiO₃/*ns*-TiO₂ annealed at the same temperature (500 °C). In addition, the reactivity of Pb-doped TiO₂ is similar to the undoped TiO₂. Those results indicate that Pb doping is not the primary factor leading to the enhancement of photochemical reactivity of *mc*-PbTiO₃/*ns*-TiO₂.

While there have been two other examples of heterostructured photoactive materials comprised of micron scale cores and nanostructured coatings,^{27,30} this is the first example that uses a visible light absorbing ferroelectric core. The strategy of separating the light absorbing function and the surface reaction function of the photocatalyst to different phases in intimate contact is likely to lead to many other visible light photochemically active materials. The findings presented here indicate that controlling the hierarchical structural features of the particle, including the length scales of structural features in the core and the shell, will be important for optimizing performance.

6.4 Summary

Heterostructured powders consisting of a microcrystalline PbTiO_3 core surrounded by a nanostructured TiO_2 shell were prepared by the sol-gel method. This composite exhibited enhanced photochemical activity for methylene blue degradation in visible light when compared to the component phases by themselves. The enhanced photochemical reactivity is attributed to the absorption of visible light by the PbTiO_3 core, the separation of photogenerated carriers by internal fields at the interface, and reaction at the surface in a nanostructured TiO_2 shell. The enhancement in the photochemical activity cannot be explained by the incorporation of Pb in the titania. The reactivities of materials annealed at different temperatures did not scale with surface area, suggesting that the crystallinity of the shell and structural integrity of the interface are also important factors.

6.5 References

- (1) Soh, J. R.; Lee, H. M.; Kwon, H. S. *Calphad-Comput. Coupling Ph. Diagrams Thermochem.* **1994**, *18*, 237.
- (2) Chan, C. K.; Porter, J. F.; Li, Y. G.; Guo, W.; Chan, C. M. *Journal of the American Ceramic Society* **1999**, *82*, 566.
- (3) Zhang, Q. H.; Gao, L.; Guo, J. K. *Applied Catalysis B-Environmental* **2000**, *26*, 207.
- (4) Munk, P. K. a. F. Z. *Tech. Phys.* **1931**, *12*, 593.
- (5) Arney, D.; Watkins, T.; Maggard, P. A. *Journal of the American Ceramic Society* **2011**, *94*, 1483.
- (6) Zametin, V. I. *Physica Status Solidi B-Basic Research* **1984**, *124*, 625.
- (7) Hosseini, S. M.; Movlaroooy, T.; Kompany, A. *Physica B-Condensed Matter* **2007**, *391*, 316.
- (8) Yadav, H. O. *Ceramics International* **2004**, *30*, 1493.
- (9) Wu, T. X.; Liu, G. M.; Zhao, J. C.; Hidaka, H.; Serpone, N. *Journal of Physical Chemistry B* **1999**, *103*, 4862.
- (10) Zhao, W.; Chen, C. C.; Li, X. Z.; Zhao, J. C.; Hidaka, H.; Serpone, N. *The Journal of Physical Chemistry B* **2002**, *106*, 5022.

- (11) Baiju, K. V.; Shukla, S.; Sandhya, K. S.; James, J.; Warriar, K. G. K. *The Journal of Physical Chemistry C* **2007**, *111*, 7612.
- (12) Carreon, M. A.; Choi, S. Y.; Mamak, M.; Chopra, N.; Ozin, G. A. *Journal of Materials Chemistry* **2007**, *17*, 82.
- (13) Houas, A.; Lachheb, H.; Ksibi, M.; Elaloui, E.; Guillard, C.; Herrmann, J. M. *Applied Catalysis B-Environmental* **2001**, *31*, 145.
- (14) Grant, F. A. *Reviews of Modern Physics* **1959**, *31*, 646.
- (15) Pascual, J.; Camassel, J.; Mathieu, H. *Physical Review B* **1978**, *18*, 5606.
- (16) Imanishi, A.; Tsuji, E.; Nakato, Y. *The Journal of Physical Chemistry C* **2007**, *111*, 2128.
- (17) Breckenridge, R. G.; Hosler, W. R. *Physical Review* **1953**, *91*, 793.
- (18) Butler, M. A.; Ginley, D. S. *Journal of the Electrochemical Society* **1978**, *125*, 228.
- (19) Rao, P. S.; Hayon, E. *The Journal of Physical Chemistry* **1973**, *77*, 2753.
- (20) Albery, W. J.; Bartlett, P. N. *Journal of the Electrochemical Society* **1984**, *131*, 315.
- (21) Gavriilya, V. G.; Spinko, R. I.; Martynen, M. A.; Fesenko, E. G. *Soviet Physics Solid State, Ussr* **1970**, *12*, 1203.
- (22) Zhang, X.; Zhang, L. Z.; Xie, T. F.; Wang, D. J. *The Journal of Physical Chemistry C* **2009**, *113*, 7371.
- (23) Burbure, N. V.; Salvador, P. A.; Rohrer, G. S. *Chemistry of Materials* **2010**, *22*, 5831.
- (24) Burbure, N. V.; Salvador, P. A.; Rohrer, G. S. *Chemistry of Materials* **2010**, *22*, 5823.
- (25) Chen, C. C.; Ma, W. H.; Zhao, J. C. *Chemical Society Reviews* **2010**, *39*, 4206.
- (26) Kudo, A.; Miseki, Y. *Chemical Society Reviews* **2009**, *38*, 253.
- (27) Li, L.; Salvador, P. A.; Rohrer, G. S. *Journal of the American Ceramic Society* **2011**, *submitted*.
- (28) Kim, H. G.; Becker, O. S.; Jang, J. S.; Ji, S. M.; Borse, P. H.; Lee, J. S. *Journal of Solid State Chemistry* **2006**, *179*, 1214.
- (29) Long, R.; Dai, Y.; Meng, G.; Huang, B. B. *Physical Chemistry Chemical Physics* **2009**, *11*, 8165.
- (30) Gao, B.; Kim, Y. J.; Chakraborty, A. K.; Lee, W. I. *Applied Catalysis B-Environmental* **2008**, *83*, 202.

7. Photocatalytic Activity of FeTiO₃/TiO₂ and AFeO₃/TiO₂ (A= Bi, La, Y) Heterostructures

As shown in the previous chapters, ATiO₃/TiO₂ (A=Ba, Sr, Pb) heterostructures showed enhanced photocatalytic activity for hydrogen production from water compared with their components under UV and visible light. In order to determine if the compositions of A and B sites in ABO₃ structure show influence on the photocatalytic activity of the ABO₃/TiO₂ heterostructures, a series of AFeO₃ (A= Bi, La, Y) compounds were chosen as the core materials. FeTiO₃, which combines Ti and Fe in the A and B sites, is also used to investigate the photocatalytic activity of the heterostructure. In this chapter, the influence of composition of core materials on the photocatalytic activity of the heterostructure is discussed. By comparing the materials with different band gap energies, band positions, and other physical parameters, an initial exploration into core materials selection and heterostructure design was carried out. In some cases, dipolar fields can be expected from p-n junctions or ferroelectricity, but no effort was made to extract the contributions from such internal fields to the activity of the heterostructures. The focus here was moreso on investigating the effects of shifting from Ti-based cores to Fe-based cores.

7.1 Photocatalytic Activity of FeTiO₃/TiO₂ Heterostructure

7.1.1 Phase Composition

XRD patterns of *mc*-FeTiO₃/*ns*-TiO₂ heterostructures and their components are given in figure 7-1. All diffraction peaks from the heterostructures and the components can be indexed to the standard diffraction pattern of anatase TiO₂ (JCPDS 46-1237) and FeTiO₃ ((JCPDS 75-1211). The observation of anatase is consistent with previous reports that indicate the conversion temperature from anatase to rutile is greater than 600 °C.^{1,2} That no other phases were observed implies no reaction occurs between FeTiO₃ and TiO₂, at any of the annealing temperatures (note the single phase powders were annealed at 500 °C). With an increase of the annealing temperature from 400 °C to 600 °C, the width of the peak at 25.28 °, which is related to (101) plane of anatase TiO₂, narrows. This result can be explained if the crystal size of nanostructured TiO₂ coating increased with the increase of annealing temperature, as a result of the thermal coarsening.

Though no tertiary phases were observed in the heterostructures, it is possible that some Fe-doping of TiO₂ occurred, as reported in similar heterostructures.³ To test this hypothesis, we prepared 1 mol% Fe-doped TiO₂. The TiO₂ phase in the doped TiO₂ powder was also anatase. The (101) and (200) diffraction peaks, respectively at 25.28 ° and 48.05 °, were used to calculate the *a* and *c* lattice parameters of tetragonal anatase, as well as the unit cell volumes. Table 7-1 presents the comparison of lattice parameters for undoped TiO₂, Fe-doped TiO₂ and TiO₂ in the *mc*-FeTiO₃/*ns*-TiO₂

heterostructure. The Fe-doped TiO₂ had no difference in the a lattice parameter, but had a decreased c parameter and, thus, a decreased unit cell volume. This indicates the addition of Fe³⁺ leads to the shrinkage of the unit cell along c axis. Considering that the ionic radius of Fe³⁺ (0.64 Å) is a little smaller than Ti⁴⁺ (0.68 Å),⁴ it is reasonable that Ti⁴⁺ can be substituted by Fe³⁺ at low levels causing only small decrease of the unit cell volume. The lattice parameters and unit cell volume of TiO₂ in FeTiO₃/TiO₂ heterostructure is similar to that of undoped TiO₂. This indicates little Fe interdiffuses from the FeTiO₃ core to the TiO₂ shell.

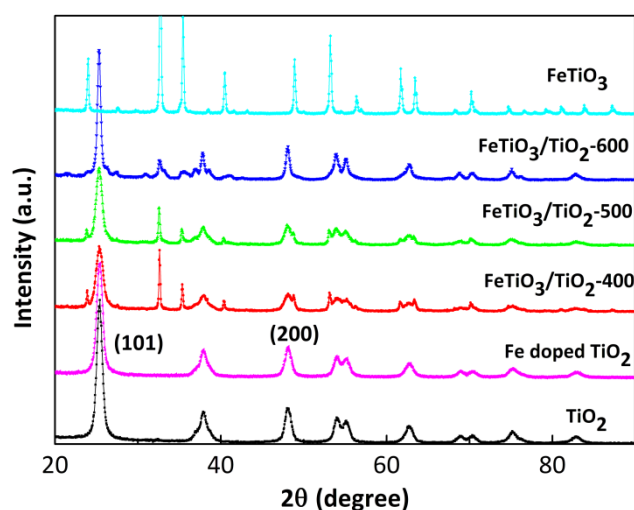


Figure 7-1 X-ray diffraction pattern of *mc*-FeTiO₃/*ns*-TiO₂ core/shell heterostructure annealed at different temperatures from 400 to 600 °C and their components. The diffraction pattern of 1mol% Fe doped TiO₂ is also shown. The number after the heterostructure represents the annealing temperature in the preparation of heterostructure by sol-gel method. (e.g. -400: 400 °C). The TiO₂ and FeTiO₃ powders were annealed at 500°C.

Table 7-1 Lattice parameters and unit cell volumes of undoped TiO₂, Fe-doped TiO₂ (D-TiO₂), and TiO₂ phases in FeTiO₃/TiO₂ heterostructure (H-TiO₂).

Materials	d ₁₀₁ (Å)	d ₂₀₀ (Å)	a(Å)	c(Å)	Volume(Å ³)
TiO ₂	3.501	1.889	3.778	9.315	133.0
D-TiO ₂	3.493	1.889	3.778	9.167	130.8
H-TiO ₂	3.507	1.893	3.786	9.308	133.4

7.1.2 Morphology

The core-shell microstructure and morphology of *mc*-FeTiO₃/*ns*-TiO₂ heterostructured powders annealed at 500 °C was analyzed in detail using TEM. A low magnification TEM bright field image that includes an entire particle is shown in Figure 7-2(a). The dark region is considered to be the FeTiO₃ microcrystalline core, surrounded by a semi-transparent layer that is considered to be the nanostructured TiO₂ shell. A higher magnification bright field TEM image, taken from the semi-transparent region, is shown in figure 7-2(b). In this figure, the transparent layer is clearly composed of (TiO₂) nanoparticles with approximate diameters of 10-15 nm. This is consistent with the 9 nm particle diameter value calculated using the Scherrer equation and the measured width of the TiO₂ XRD peak, which is shown in figure 7-1. A sharp and clear interface can be observed between *mc*-FeTiO₃ core and *ns*-TiO₂ shell.

The selected area diffraction pattern (SAED) of the TiO₂ nanostructured coating is shown in figure 7-2(c). The diffraction pattern consists of a series of concentric circles, rather than bright sharp dots, because of the polycrystalline nature of the nanostructured TiO₂ coatings. Those diffraction circles were indexed and identified as the planes of tetragonal anatase TiO₂. Figure 7-2(d) is the high resolution TEM (HRTEM) image of TiO₂ coating. The atomic arrangement is highlighted with the white solid line. The distance between two contiguous atomic planes is measured to be 3.5 Å, which is consistent with the value of interplanar distance of the (101) plane in anatase TiO₂. These results are consistent with our earlier results on the titanates.

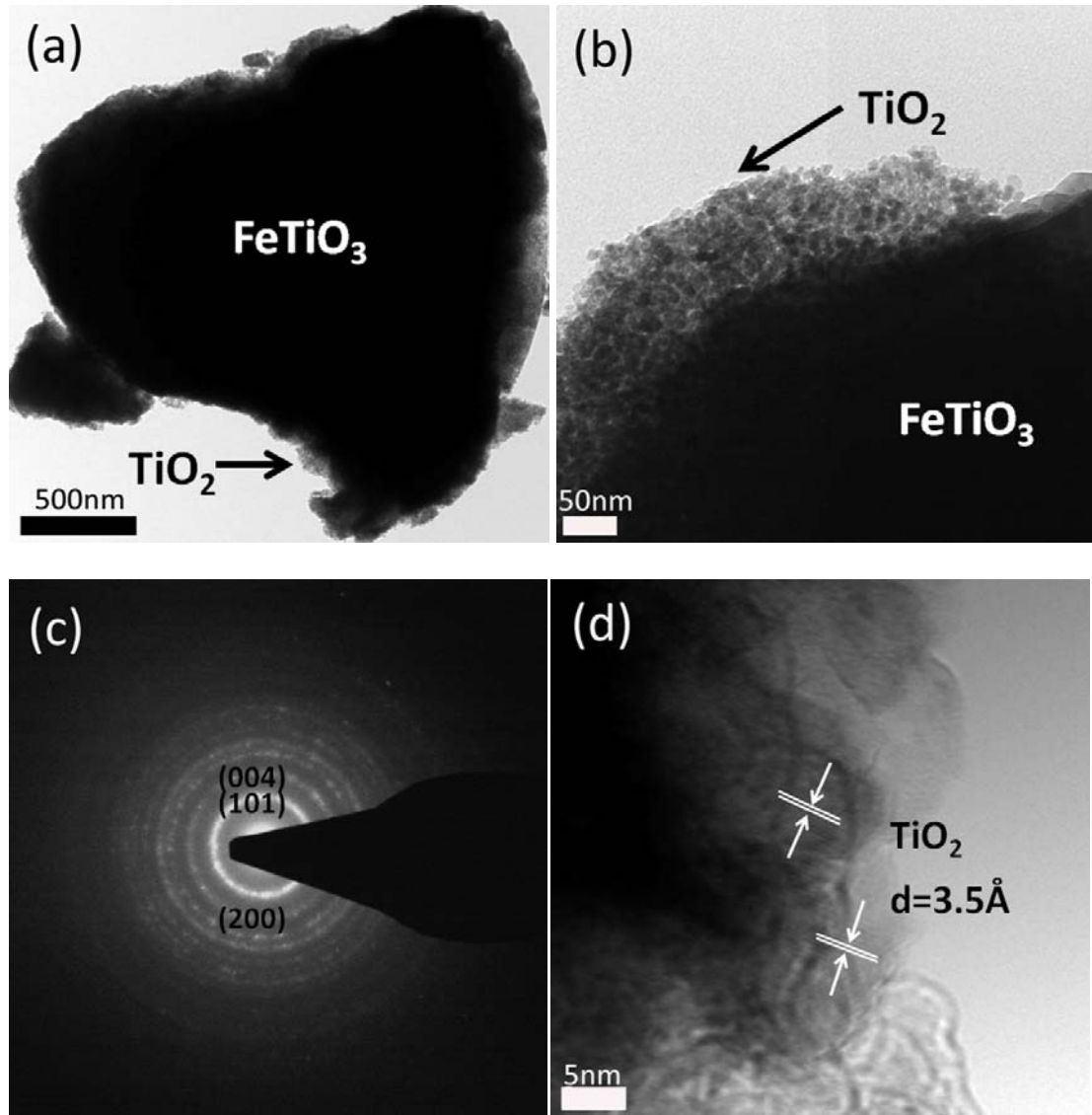


Figure 7-2 TEM images of *mc*-FeTiO₃/*ns*-TiO₂ heterostructure powders annealed at 500 °C: (a) low magnification bright field images of the entire particles; (b) high magnification bright field image of detail about FeTiO₃ and TiO₂ interface; (c) SAED of TiO₂ coating; and (d) HRTEM image of TiO₂ coating.

7.1.3 Optical Properties

The optical properties of *mc*-FeTiO₃/*ns*-TiO₂ heterostructure annealed at different temperatures and their components were shown in figure 7-3. The reflectance of various powders was measured by UV-visible spectrometer. FeTiO₃

shows strong absorption both in UV and visible light range. Considering the structure of FeTiO₃, the strong polarized covalent bond between metal and oxygen ions produces a charge transfer from oxygen to metal, leading to the absorption in the visible light region. The reported band gap energy of FeTiO₃ varies rather widely in the literature but the value for bulk FeTiO₃ is generally reported to be between 2.5-2.6 eV⁵⁻⁸ (values as high as 3.55 eV have been reported,⁹ in that report it was for a FeTiO₃ thin film). The phenomenon that no peaks relating to the bandgap excitation of FeTiO₃ are observed in its UV-vis spectrum is explained owing to absorption from the intervalence charge transfer between Fe²⁺ and Ti⁴⁺ as well as Fe³⁺ and Ti³⁺.^{7,10}

The heterostructured powders annealed at different temperatures show similar reflectance to each other in the UV and visible range. No significant difference for light absorption is observed. In addition, the reflectance of heterostructure powders is more similar to FeTiO₃ than TiO₂. Combined with the XRD result that little Fe doping is observed in the TiO₂ coating, the similarity of the optical properties of *mc*-FeTiO₃/*ns*-TiO₂ heterostructures to FeTiO₃ indicates the *mc*-FeTiO₃ core is the primary light absorbing component in the heterostructure (though absorption in the coating cannot be ruled out). The Fe-doped TiO₂ powder (which is yellow in color) extends its absorption edge into the deep visible light range and shows stronger absorption in both UV and visible range than undoped sample.

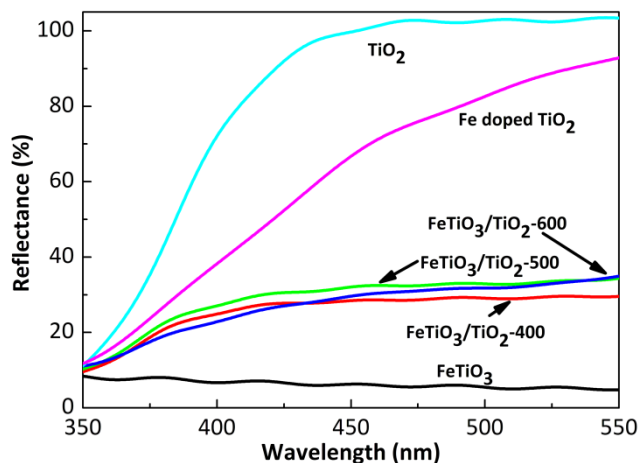


Figure 7-3 UV-visible spectra of *mc*-FeTiO₃/*ns*-TiO₂ heterostructure annealed at different temperatures, its components, and Fe-doped TiO₂.

7.1.4 Photocatalytic Activity for Methylene Blue Degradation

The physical properties of different photocatalysts and their reactivity for photocatalytic dye degradation of methylene blue are shown in table 7-2. The surface area of FeTiO₃ is 0.47 m²/g, indicating the powder is in the micron-sized range. This is consistent with the results from TEM. The surface area of *mc*-FeTiO₃/*ns*-TiO₂ decreased from 93 m²/g at 400 °C to 40 m²/g at 600 °C. The pore volume of *mc*-FeTiO₃/*ns*-TiO₂ annealed at 600 °C was smaller than the value for samples annealed at 400 °C and 500 °C, indicating a denser heterostructured coating was prepared.

Figure 7-4 shows the photocatalytic activity for methylene blue degradation under visible light irradiation of *mc*-FeTiO₃/*ns*-TiO₂ heterostructured powder annealed at 500 °C, and of its components. (It should be noted that no dye degradation was observed without the addition of a photocatalyst). The time evolution of dye degradation, represented as C/C_0 , is consistent with the pseudo-first-order model.¹¹⁻¹³

The *mc*-FeTiO₃/*ns*-TiO₂ heterostructure exhibits high visible light photocatalytic reactivity when compared with its components, both in the degradation rate, which is represented as the slope of $\ln(C_0/C)$ vs time, and the amount of dye degraded after 6 hours experiment. The reaction rate K_{MB} of *mc*-FeTiO₃/*ns*-TiO₂ and its components are shown in table 7-2. The MB removal rate of *mc*-FeTiO₃/*ns*-TiO₂ (0.17 h⁻¹) is 3.4 times that of TiO₂ (0.05 h⁻¹) and 5.7 times of FeTiO₃ (0.03 h⁻¹), respectively. The corresponding reactivity of a mechanical mixture of FeTiO₃ and TiO₂ (0.03 h⁻¹) is only about 17.6% of the core/shell structure, which demonstrates the core/shell heterostructured powder is more active. In addition, the reactivity of *mc*-FeTiO₃/*ns*-TiO₂ and TiO₂ for methylene blue dye degradation under dark is also presented in figure 7-4. Little degradation was observed for the powders without irradiation, which confirms that the efficient degradation of methylene blue is photocatalytic (and not chemical).

Table 7-2 Physical properties of heterostructured powders and their reaction rates for photocatalytic degradation of methylene blue (K_{MB}).

Catalyst	Processing Temperature (°C)	BET Surface Area (m ² /g)	Pore Volume (cc/g)	K_{MB} (h ⁻¹)
TiO ₂	500	83	0.14	0.05
FeTiO ₃	500	0.47	0.003	0.03
FeTiO ₃ /TiO ₂	400	93	0.13	0.04
	500	73	0.11	0.17
	600	40	0.06	0.09

TiO₂ exhibits higher dye degradation rate under visible light illumination than under dark. This phenomenon is explained as the so-called “TiO₂ mediated dye

degradation” or “self photosensitized degradation” of dyes.^{14,15} During this process, TiO₂ is not excited to produce electrons and holes but only provides the pathway to transfer the injected electrons from excited dye to the adsorbed dye on TiO₂ surface for degradation.

To test if the enhancement of photocatalytic activity for *mc*-FeTiO₃/*ns*-TiO₂ originates from the interdiffusion of Fe to the TiO₂ coating, Fe doped TiO₂ was prepared and tested for MB degradation under visible light. The previous literature reports Fe doping can extend the absorption of TiO₂ to the visible light range, which was also observed in our UV-vis experiments. This has been suggested to arise from the creation of a donor level above the valance band edge; the donor level leads to absorption in the visible region and, thus, leads to photocatalytic activity enhancement for water splitting and some dye degradation experiments.^{16,17} However, the substituted Fe dopants can also serve as centers for charge carrier recombination,^{18,19} which then reduces overall photocatalytic activity. The current experiments demonstrate that 1% Fe doping did not enhance the photocatalytic activity of TiO₂ for MB degradation and imply that simple Fe doping of TiO₂ does not produce the efficient reactivity of *mc*-FeTiO₃/*ns*-TiO₂ heterostructure powders.

The influence of annealing temperature on the photocatalytic activity of heterostructure powders is shown in table 7-2. *mc*-FeTiO₃/*ns*-TiO₂ annealed at 500 °C exhibits the highest reactivity for MB degradation amongst the three samples. The reactivity of the sample annealed at 500 °C (0.17 h⁻¹) is 4.3 times and 1.9 times that of the powders annealed at 400 °C (0.04 h⁻¹) and 600 °C (0.09 h⁻¹), respectively. It is

noteworthy that the surface area of the sample annealed at 500 °C is even smaller than the powder annealed at 400 °C. These collected observations will be discussed further in Section 7.3, after first presenting the work of perovskite iron-oxides (AFeO_3).

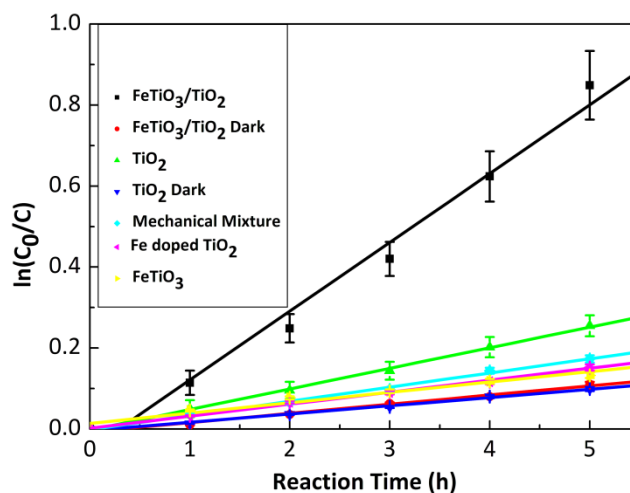


Figure 7-4 Photodegradation of methylene blue with $\text{FeTiO}_3/\text{TiO}_2$ annealed at 500 °C and its components. The reactivity of FeTiO_3 and TiO_2 mechanical mixture as well as Fe doped TiO_2 are also shown here. Blank refers to the dye degradation without any powder addition.

7.2 Photocatalytic Activity of $(\text{Bi},\text{La},\text{Y})\text{FeO}_3/\text{TiO}_2$ Heterostructure

7.2.1 Structure Characterization

BiFeO_3 , LaFeO_3 , and YFeO_3 were synthesized in our lab (see Chapter 3). The phase composition of these powders was analyzed by XRD, and their patterns are shown in Figure 7-5. All peaks in the XRD diffractograms are indexable to the corresponding powders (BiFeO_3 , JCPDS 86-1518; LaFeO_3 , JCPDS 37-1493; YFeO_3 , JCPDS 39-1489) and no secondary phase was observed.

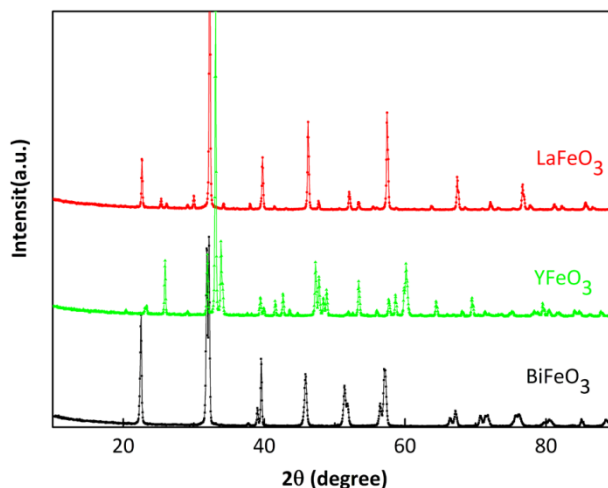


Figure 7-5 Powder x-ray diffractograms of (a) BiFeO_3 prepared by hydrothermal method, (b) YFeO_3 prepared by sol-gel method, and (c) LaFeO_3 prepared by citrate gel method.

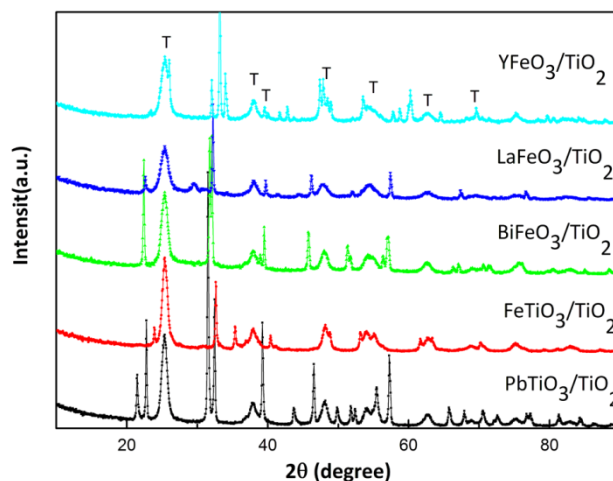


Figure 7-6 Powder x-ray diffractograms of various heterostructured powders. The titanium dioxide phase was designated as “T” and marked in the figure.

Figure 7-6 shows the phase composition of heterostructured powders analyzed by XRD. The titania phases are designated by the “T” and marked above the corresponding peaks. Based on comparisons between the data in Figure 7-5 and the JCPDS database, no secondary phases were observed in our powders (anatase TiO_2 , (JCPDS 46-1237; PbTiO_3 , JCPDS 06-0452; FeTiO_3 , JCPDS 75-1211; BiFeO_3 , JCPDS 86-1518; LaFeO_3 , JCPDS 37-1493; and YFeO_3 , JCPDS 39-1489). All peaks are related to TiO_2 and the corresponding components. No reaction is observed between

the component phases. TiO_2 peaks marked in the figure are primarily anatase.

7.2.2 Photocatalytic Activities of the Heterostructures

The surface areas, pore structures, and the reactivities for photocatalytic degradation of methylene blue with different materials are shown in table 7-3, while the $\text{FeTiO}_3/\text{TiO}_2$ was shown in table 7-2. $(\text{Pb,Fe})\text{TiO}_3/\text{TiO}_2$ heterostructures show low surface areas, while $(\text{Bi,La,Y})\text{FeO}_3/\text{TiO}_2$ heterostructures display high values. This phenomenon can be understood if the different cores influence the microstructure of the nanostructured coating differently. When the organic molecule is removed from the three-dimensional network of the TiO_2 xerogel during annealing, interparticle pores are formed, which are the origin of porosity of the nanostructured coating. The pore structure begins to collapse upon any increase in temperature. The interface of the xerogel network with the core scaffold can stabilize the pore from collapsing, to some degree. The degree of stabilization will depend on the nature of the core and the interactions with the xerogel network. Based on the high surface areas, the iron-based perovskites $(\text{Bi,La,Y})\text{FeO}_3$ appear to stabilize the TiO_2 coating better than the $(\text{Pb,Fe})\text{TiO}_3$ materials. The large pore volumes observed for $(\text{Bi,La,Y})\text{FeO}_3/\text{TiO}_2$ also confirm this point.

The visible light reactivity of other various photocatalysts toward the degradation of methylene blue is shown in figure 7-7 and is listed in table 7-3. Compared with their photocatalytic activity, $(\text{Pb,Fe})\text{TiO}_3/\text{TiO}_2$ exhibits pronounced enhancement for dye degradation as compared to TiO_2 alone. *mc*- BiFeO_3/ns - TiO_2 also shows a little

higher degradation rate than TiO_2 alone, while $mc\text{-LaFeO}_3/ns\text{-TiO}_2$ and $mc\text{-YFeO}_3/ns\text{-TiO}_2$ displays lower reactivity. All single component powders, namely $mc\text{-PbTiO}_3$, $mc\text{-FeTiO}_3$, $mc\text{-BiFeO}_3$, $mc\text{-LaFeO}_3$ and $mc\text{-YFeO}_3$, show little reactivity for methylene blue degradation, which is not shown herein. Their reactivities are far smaller than TiO_2 alone due to their small surface area. This result also means the reactivity of the heterostructure powders originates from the interaction between core and shell, rather than the components alone.

Table 7-3 Physical properties of heterostructured powders and its reaction rate for photocatalytic degradation of methylene blue (K_{MB}).

Catalyst	Processing Temperature (°C)	BET Surface Area (m^2/g)	Pore Volume (cc/g)	K_{MB} (h^{-1})
$\text{PbTiO}_3/\text{TiO}_2$	500	74	0.15	0.24
$\text{BiFeO}_3/\text{TiO}_2$	500	104	0.20	0.07
$\text{LaFeO}_3/\text{TiO}_2$	500	109	0.23	0.04
$\text{YFeO}_3/\text{TiO}_2$	500	115	0.22	0.01

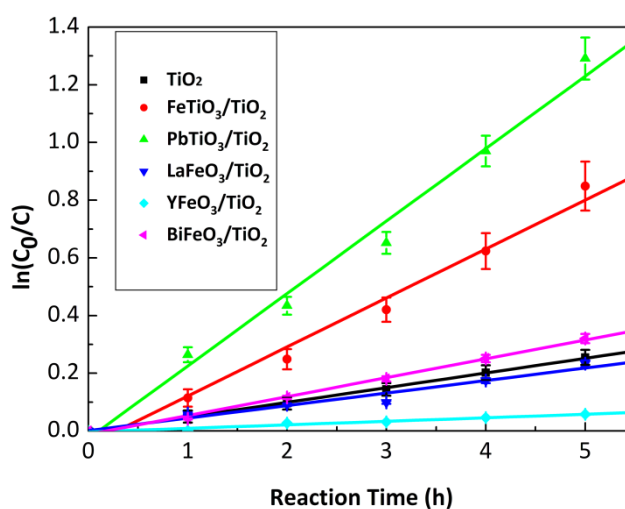


Figure 7-7 Photodegradation of methylene blue with $(\text{Pb,Fe})\text{TiO}_3/\text{TiO}_2$ and $(\text{Bi,La,Y})\text{FeO}_3$ annealed at 500 °C and TiO_2 under visible light illumination.

7.3 Discussion

The primary observation in this chapter is that $ATiO_3/TiO_2$ ($A=Pb, Fe$) shows significantly enhanced photocatalytic activity under visible light irradiation when compared to their components alone, while $AFeO_3/TiO_2$ ($A= Bi, La, Y$) do not (though $BiFeO_3/TiO_2$ show very tiny enhanced photocatalytic activity than TiO_2 alone). This interesting phenomenon shows B sites in ABO_3/TiO_2 is directly related to the photocatalytic activity of the heterostructures.

The electronic properties of various core materials and TiO_2 are listed in table 7-4. The conduction band positions of TiO_2 and $FeTiO_3$ are reported and cited herein.^{10,20} The conduction band positions (E_c), which considered the same level with flat band potential, of other materials are calculated by the following equation proposed by Butler and Ginley:²¹

$$(7-1) \quad V_{fb} = E_0 - X + 1/2E_{bg}$$

$$(7-2) \quad X = 1/2(A+I)$$

In these equations, V_{fb} is flat band potential, E_0 is the energy of a free electron on the H_2 redox potential (4.5 eV), X is the Sanderson electronegativity of semiconductor, E_{bg} is the band gap energy of semiconductor, A is the electron atomic electron affinity, and I is the first ionization potential. For AB_2 compounds, X is defined as equation (7-3).

$$(7-3) \quad X = [X(A)X(B)^2]^{1/3}$$

Table 7-4 Electronic properties of various core materials and TiO₂.

Materials	E _{bg} (eV)	E _A (eV)	E _c (eV)	E _v (eV)
PbTiO₃	2.85	4.23	-0.27	2.58
FeTiO₃	2.6 ¹⁰	4.6	0.1	2.7
BiFeO₃	2.6 ²²	4.6	0.1	2.7
LaFeO₃	2.4 ²³	4.35	-0.15	2.25
YFeO₃	2.6 ²⁴	4.35	-0.15	2.45
TiO₂	3.2	4.1	-0.4	2.8

Figure 7-8 shows the band position of various powders relative to standard hydrogen electrode (SHE) level, which is defined as 0 eV in current conditions. If we combine the information shown in this figure with the band gap schematic of BaTiO₃ and SrTiO₃ discussed in Chapter 4, we can see that the conduction band positions of BaTiO₃ and SrTiO₃ are quite close to that of TiO₂; that in PbTiO₃ is slightly lower than for TiO₂, while the conduction band positions of AFeO₃ (A=Bi, La, Y) are yet lower than that of TiO₂. The conduction band edge position of FeTiO₃ is more similar to the AFeO₃ materials, so this edge does not clearly explain reactivity enhancement of specific heterostructures. That no heterostructures with an edge lower than that of TiO₂ were active for H₂ production indicates the energy levels of electrons for reaction must be above the reaction level for the solution reduction, as expected. That the band edge does not clearly correlate with dye degradation reactivity is less clear.

The band gap energies of BaTiO₃ and SrTiO₃ are 3.2 eV, which is the same to that of TiO₂ at 3.2 eV. The similarities of band gap energy and conduction band position for ATiO₃ (A= Ba, Sr) can assist the electrons transfer from core to TiO₂ coating easier. Meanwhile, the process for electrons tunneling from core to the shell is

also easier. This means more electrons from core materials can participate in the redox reaction in the TiO_2 coating. The value is slightly lower for PbTiO_3 at 2.85 eV and for FeTiO_3 at 2.6 eV, but dye degradation is still enhanced for heterostructures with these cores. Considering the values for AFeO_3 (A= Bi, La, Y), it is not clear as to why those heterostructures do not show enhanced photocatalytic activity as compared to their components. Perhaps the strongest correlation is with the valence band edge. For $(\text{La},\text{Y})\text{FeO}_3$, the valence band edge is below 6.95 eV, while it is greater than 7 eV and close to the edge of TiO_2 for the others. This suggests that the hole transfer overpotential is too large in the Fe-O based systems.

Another reason leading to the enhancement of photocatalytic activity of ATiO_3 (A= Ba,Sr,Pb,Fe)/ TiO_2 may be nature of bond formation between TiO_6 octahedra in the core materials and TiO_6 octahedra in the TiO_2 shell, as compared to that between FeO_6 octahedra in the AFeO_3 core materials to the TiO_6 octahedra in TiO_2 coating. The bonding between Fe^{3+} in the FeO_6 octahedra to Ti^{4+} in TiO_6 octahedra will form Fe-O-Ti bonds, which will change the chemical potential and the polarity of the chemical bonds.²⁵ It can be assumed the interfacial Ti-O-Ti bonding in the TiO_2 and ATiO_3 leads to better charge transfer than the Fe-O-Ti bonding between AFeO_3 and TiO_6 octahedra, resulting in improved redox reactions. It also can be noticed that the pore volume and surface area of $\text{AFeO}_3/\text{TiO}_2$ are larger than those of $\text{ATiO}_3/\text{TiO}_2$ (table 7-2 and 7-3). This indicates that denser coating leads to the formation of stronger bondings between ATiO_3 and TiO_2 than that between AFeO_3 and TiO_2 .

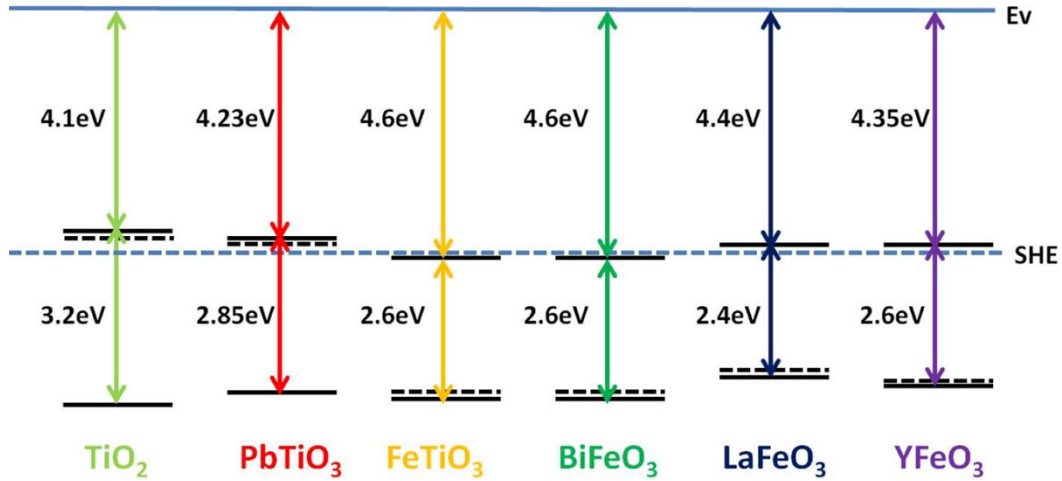


Figure 7-8 The schematic of band gap energy and band positions for various core materials.

The structure of FeTiO₃ is a little different from other ATiO₃ perovskites (A=Ba, Sr, Pb). Its ilmenite structure involves both FeO₆ and TiO₆ octahedra.²⁶ Though both Fe³⁺/Ti³⁺ and Fe²⁺/Ti⁴⁺ pairs exist in FeTiO₃, FeTiO₃ still can be considered as one member of a series of compounds that includes the titanates A²⁺Ti⁴⁺O₃.²⁶⁻²⁸ This may explain why FeTiO₃/TiO₂ shows enhanced photocatalytic activity compared with its components alone, though the band gap energy and conduction band position of FeTiO₃ are similar to AFeO₃ (A=Bi, La, Y) and different from TiO₂.

Another reason leading to the enhancement of photocatalytic activity of FeTiO₃/TiO₂ is attributed to the formation of p-n junction between p-type FeTiO₃ and n-type TiO₂. The internal field formed in the p-n junction can assist the charge separation to the different direction and thus increase the photocatalytic activity. P-type ferroelectric BiFeO₃ coated with TiO₂ film is observed to show high photocatalytic activity for silver reduction under visible light irradiation in our group.²⁹ The internal field from the p-n junction and ferroelectric polarization from the BiFeO₃ substrate will assist the separation of charge carriers. However, only a

very small enhancement of photocatalytic activity of BiFeO₃/TiO₂ core/shell structure is observed compared with its components in our experiment. The current experiment in this chapter shows the electronic structure (band gap energy and conduction band position) similarities to TiO₂ coating and bonding between core and shell are also important factors to affect the photocatalytic activity of our micro-nano core/shell heterostructures. This may be the reason why the combination of p-type LaFeO₃ and YFeO₃ with n-type TiO₂, which also form p-n junction in the interface, did not show enhanced photocatalytic activity for dye degradation. In other words, there is no strong evidence that enhancement arises from the p-n junction effects.

The influence of annealing temperature on the photocatalytic activity of FeTiO₃/TiO₂ is consistent with the previous result of BaTiO₃/TiO₂ discussed in Chapter 5. The enhancement of reactivity of *mc*-FeTiO₃/*ns*-TiO₂ for methylene blue degradation with the increase of annealing temperature confirmed that strong chemical bonds between core and shell is beneficial for the improvement of photocatalytic activity. Though *mc*-FeTiO₃/*ns*-TiO₂ annealed at 500 °C exhibited apparent higher degradation rate than the as-prepared samples annealed at 600 °C, the heterostructure annealed at 600 °C shows the highest reaction rate per surface area among all *mc*-FeTiO₃/*ns*-TiO₂ samples after removing the influence from surface area.

7.4 Summary

In this chapter, the photocatalytic activity of ATiO₃ (A= Fe, Pb) heterostructures

is compared with the reactivity of $AFeO_3$ ($A = Bi, La, Y$) heterostructures for methylene blue degradation under visible light irradiation. Compared with the previous experiments result from $BaTiO_3$ and $SrTiO_3$, it can be observed that $ATiO_3$ ($A = Ba, Sr, Pb, Fe$)/ TiO_3 displays enhanced photocatalytic activity than their components while $AFeO_3$ ($A = Bi, La, Y$) do not. This phenomenon is explained that the similarities of electronic properties (band gap energy and conduction band position) of core materials to the TiO_2 coating and the bonding between core and shell also influence the photocatalytic activity of the micro-nano heterostructures greatly. The influence of annealing temperature on the photocatalytic activity of $FeTiO_3/TiO_2$ is studied. The heterostructured annealing at 500 °C shows the highest methylene blue degradation rate in 5 hours visible light irradiation.

7.5 References

- (1) Chan, C. K.; Porter, J. F.; Li, Y. G.; Guo, W.; Chan, C. M. *Journal of the American Ceramic Society* **1999**, *82*, 566.
- (2) Baiju, K. V.; Shukla, S.; Sandhya, K. S.; James, J.; Warriar, K. G. K. *The Journal of Physical Chemistry C* **2007**, *111*, 7612.
- (3) Bruzzone, S.; Arrighini, G. P.; Guidotti, C. *Materials Science and Engineering: C* **2003**, *23*, 965.
- (4) Wang, C.-y.; Bottcher, C.; Bahnemann, D. W.; Dohrmann, J. K. *Journal of Materials Chemistry* **2003**, *13*, 2322.
- (5) Ginley, D. S.; Butler, M. A. *Journal of Applied Physics* **1977**, *48*, 2019.
- (6) S. S. Sunkara; R. K. Pandey. *Ceramic Transactions* **1995**, *60*, 83.
- (7) Wilson, N. C.; Muscat, J.; Mkhonto, D.; Ngoepe, P. E.; Harrison, N. M. *Physical Review B* **2005**, *71*.
- (8) Blasse, G.; Dirksen, G. J.; Dekorte, P. H. M. *Materials Research Bulletin* **1981**, *16*, 991.
- (9) Dai, Z.; Naramoto, H.; Narumi, K.; Yamamoto, S.; Miyashita, A. *Journal of Applied Physics* **1999**, *85*, 7433.
- (10) Gao, B.; Kim, Y. J.; Chakraborty, A. K.; Lee, W. I. *Appl. Catal. B-Environ.* **2008**, *83*, 202.
- (11) Baiju, K. V.; Shukla, S.; Sandhya, K. S.; James, J.; Warriar, K. G. K. *The Journal of Physical Chemistry C* **2007**, *111*, 7612.

- (12) Carreon, M. A.; Choi, S. Y.; Mamak, M.; Chopra, N.; Ozin, G. A. *Journal of Materials Chemistry* **2007**, *17*, 82.
- (13) Houas, A.; Lachheb, H.; Ksibi, M.; Elaloui, E.; Guillard, C.; Herrmann, J. M. *Applied Catalysis B-Environmental* **2001**, *31*, 145.
- (14) Wu, T.; Liu, G.; Zhao, J.; Hidaka, H.; Serpone, N. *The Journal of Physical Chemistry B* **1999**, *103*, 4862.
- (15) Zhao, W.; Chen, C.; Li, X.; Zhao, J.; Hidaka, H.; Serpone, N. *The Journal of Physical Chemistry B* **2002**, *106*, 5022.
- (16) Serpone, N.; Lawless, D.; Disdier, J.; Herrmann, J. M. *Langmuir* **1994**, *10*, 643.
- (17) Nahar, M. S.; Hasegawa, K.; Kagaya, S. *Chemosphere* **2006**, *65*, 1976.
- (18) Wang, X. H.; Li, J. G.; Kamiyama, H.; Moriyoshi, Y.; Ishigaki, T. *The Journal of Physical Chemistry B* **2006**, *110*, 6804.
- (19) Wang, X. H.; Li, J. G.; Kamiyama, H.; Katada, M.; Ohashi, N.; Moriyoshi, Y.; Ishigaki, T. *Journal of the American Chemical Society* **2005**, *127*, 10982.
- (20) Imanishi, A.; Tsuji, E.; Nakato, Y. *The Journal of Physical Chemistry C* **2007**, *111*, 2128.
- (21) Butler, M. A.; Ginley, D. S. *Journal of The Electrochemical Society* **1978**, *125*, 228.
- (22) Gustau, C.; James, F. S. *Advanced Materials* **2009**, *21*, 2463.
- (23) Bocquet, A. E.; Fujimori, A.; Mizokawa, T.; Saitoh, T.; Namatame, H.; Suga, S.; Kimizuka, N.; Takeda, Y.; Takano, M. *Physical Review B* **1992**, *45*, 1561.
- (24) Butler, M. A.; Ginley, D. S.; Eibschutz, M. *Journal of Applied Physics* **1977**, *48*, 3070.
- (25) Yu, J.; Xiang, Q.; Zhou, M. *Applied Catalysis B: Environmental* **2009**, *90*, 595.
- (26) Wilson, N. C.; Muscat, J.; Mkhonto, D.; Ngoepe, P. E.; Harrison, N. M. *Physical Review B* **2005**, *71*, 075202.
- (27) Goodenough, J. B.; Stickler, J. J. *Physical Review* **1967**, *164*, 768.
- (28) Fennie, C. J. *Physical Review Letters* **2008**, *100*, 167203.
- (29) Zhang, Y.; Schultz, A. M.; Salvador, P. A.; Rohrer, G. S. *Journal of Materials Chemistry* **2011**, *21*, 4168.

8. Conclusions and Future Work

8.1 Conclusions

Micron-sized (*mc*-) (Ba,Sr)TiO₃ core / nanostructured (*ns*-) TiO₂ shell heterostructured ceramics exhibited enhanced photocatalytic activity for hydrogen production, when compared to any of their components alone. The results indicate that photoexcited electrons from the core can be transported to the shell and participate in reactions. The improved reactivity of the heterostructure is attributed to the combined efficient photon absorption and charge separation in the micron-sized core, efficient transfer across the core/shell interface, and high surface area and reactivity of the nanostructured TiO₂ shell. These attributions were supported by comparing the absorption coefficients of each component and the reactivity of the heterostructures to the reactivities of freestanding nanostructured TiO₂, heterostructures with non-light-absorbing cores, and mechanical mixtures of *mc*-cores with P25. The heterostructure consisting of *ns*-BaTiO₃ and a *ns*-TiO₂ coating showed lower hydrogen production than from *mc*-BaTiO₃/*ns*-TiO₂ heterostructures processed under the same conditions.

Three characteristics of the heterostructure processing, namely annealing temperature, coating thickness and cocatalyst loading amount, were optimized. The annealing temperature was shown to change the photocatalytic activity of the shell. The annealing temperature can influence interface quality, phase composition, light absorption, crystallinity, mesoporosity, surface area and other physical and chemical

parameters. These parameters all have the potential to change photocatalytic activity. The coating thickness is directly related to the photocatalytic activity of heterostructured powders. *mc*-BaTiO₃/*ns*-TiO₂ coated twice shows the highest photocatalytic activity for hydrogen production, compared with heterostructures coated once and three times. When materials loaded with different amounts of the cocatalyst were compared, it was found that heterostructured photocatalysts with 1% Pt loading exhibited the greatest reactivity for hydrogen production.

Ferroelectric PbTiO₃ microcrystals were coated with nanostructured TiO₂ using the sol-gel method. The heterostructure was more photocatalytically active for methylene blue degradation under visible light irradiation than its components. The enhancement in the photochemical activity cannot be explained by the incorporation of Pb in the titania. The reactivities of materials annealed at different temperatures did not scale with surface area, suggesting that the crystallinity of the shell and structural integrity of the interface are also important factors.

The photocatalytic activity of AFeO₃ (A= Bi, La, Y) for methylene blue degradation under visible light irradiation was also studied. The photocatalytic reactivities of ATiO₃(A= Ba, Sr, Pb, Fe)/TiO₂ heterostructures were enhanced compared to the reactivities of mixtures of the component phases while the reactivities AFeO₃ (A= Bi, La, Y)/TiO₂ heterostructures showed no enhancement. This phenomenon might be explained by the similarities of the electronic structure (band gap energy and conduction band position) of the core materials and the TiO₂ coating and the bonding between the core and shell.

8.2 Future Work

To further explore the influence of bonding between the core and shell on the photocatalytic activity of the heterostructures, Fe_2O_3 can be used as shell to coat AFeO_3 ($\text{A}=\text{Bi}, \text{La}, \text{Y}$) to investigate if the photocatalytic activity of the heterostructure can be improved. Because of the low conduction band position of Fe_2O_3 , the heterostructure is not apt to be used for hydrogen production directly from the water. Substrate/film heterostructures can be considered to be also be processed so that their photoelectrochemical properties can be explored. If AFeO_3 ($\text{A}=\text{Bi}, \text{La}, \text{Y}$)/ Fe_2O_3 heterostructures show an enhancement of the photocatalytic activity, the result will be consistent with the explanation proposed in Chapter 7.

$(\text{Ba},\text{Sr})\text{TiO}_3/\text{TiO}_2$ heterostructures have been shown to exhibit enhanced photocatalytic activity compared with its components. $\text{Ba}_x\text{Sr}_{1-x}\text{TiO}_3$ solid solution with $x=0.26$ has been confirmed to show higher photocatalytic activity for silver reduction than SrTiO_3 and BaTiO_3 alone because the high dielectric constant at that composition enlarges the space charge region.^{1,2} The solid solution $\text{Ba}_{0.26}\text{Sr}_{0.74}\text{TiO}_3$ can be considered to be coated with TiO_2 to investigate the hydrogen production rate from this heterostructure. By comparing its photocatalytic activity with $\text{BaTiO}_3/\text{TiO}_2$ and $\text{SrTiO}_3/\text{TiO}_2$, we can obtain more information about the influence of core material parameters on the photocatalytic activity of the heterostructures. We expect that $\text{Ba}_{0.26}\text{Sr}_{0.74}\text{TiO}_3/\text{TiO}_2$ can show higher hydrogen production rate than $\text{BaTiO}_3/\text{TiO}_2$ and $\text{SrTiO}_3/\text{TiO}_2$ because the larger space charge region of the core will assist the charge carriers separation and more electrons can transfer to the TiO_2 coating to

participate in redox reaction.

8.3 References

(1) Bhardwaj, A.; Burbure, N. V.; Gamalski, A.; Rohrer, G. S. *Chemistry of Materials* **2010**, *22*, 3527.

(2) Bhardwaj, A.; Burbure, N. V.; Rohrer, G. S. *Journal of the American Ceramic Society* **2010**, *93*, 4129.